Synthesis of Novel Polythiophenes Having Alkylamide Substituents for Organic Solar Cells

by

Xiaocheng Zhou

A thesis
presented to the University of Waterloo
in fulfillment of the
thesis requirement for the degree of
Master of Applied Science
in
Chemical Engineering

Waterloo, Ontario, Canada, 2018

Author's Declaration

I hereby declare that I am the sole author of this thesis. This is a true copy of the thesis, including any required final revisions, as accepted by my examiners.

I understand that my thesis may be made electronically available to the public.

Abstract

Solar energy is one of the most important sustainable energy resources which can satisfy increasingly growing demand of power and energy and reduce carbon footprint. In order to utilize the solar energy, solar cells are feasible and promising technologies to convert sunlight into electricity. Among the various types of solar cells, organic solar cells (OSCs), also known as organic photovoltaics (OPVs), are versatile technologies, because carbon based organic materials have relatively cheap, finely tunable physical properties and solution processibility that enables the manufacture of OSCs through roll-to-roll printing processes. P3HT has been one of the most intensely studied donor semiconductors for OSCs because of its easy synthesis (low cost), good solution processability, and high hole transport property. However, its relative high HOMO level results in a low open circuit voltage (Voc) and thus low power conversion efficiency (PCE) in OSCs. In this thesis, six new π-conjugated polythiophene derivatives based on the newly designed [2,2'-bithiophene]-4,4'-dicarboxamide (BTDCA) electron-deficient building block were synthesized and characterized. Firstly, **P1** and **P2** comprising BTDCA with different lengths of side chain and bithiophene (BT) were synthesized to balance the solubility and interchain packing. The HOMO levels of **P1** and **P2** were successfully lowered from -4.9 eV for P3HT to -5.3 eV for both **P1** and **P2**. **P2** showed a higher degree of crystallinity than **P1**, leading to its higher hole mobility (up to 1.4×10^{-2} $cm^2 V^{-1} s^{-1}$) compared to **P1** (up to 2.0×10^{-3} $cm^2 V^{-1} s^{-1}$). Preliminary tests of **P1** and **P2** in solar cells were conducted using the blend of **P1** or **P2** with $PC_{61}BM$. The Voc for the blend of P3HT with $PC_{61}BM$ was 0.59 V, while a significantly higher Voc of up to 0.87 V was obtained with the new materials **P1** and **P2** as donors. The Jsc values of **P2** based solar cells were low, possibly due to the large grain size resulting from the higher degree of crystallinity. Then **P3** was synthesized with a smaller comonomer unit, thieno[3,2-b]thiophene (TT), to decrease the crystallinity. The hole mobility for **P3** dropped to 4.5×10^{-4} $cm^2 V^{-1} s^{-1}$ due to the decreased crystallinity compared with **P2**. Interestingly, higher solar cell performance was achieved for **P3**, most likely due to the optimized crystallinity property and thin film morphology. The PCE of the solar cell with the blend of **P3** and ITIC (PCE = 3.5%) was three times that of P3HT and ITIC (PCE = 1.3%). After that, thiophene (T) was used as comonomer and copolymerized with BTDCA to form

P4. Unfortunately, the structure was over tuned, thus resulting in very disordered chain packing and poor OTFT and OPV performances.

Hydrogen bonding was then introduced into the BTDCA building block. **P5** and **P6** with different length of side chains were copolymerized with BT. Both **P5** and **P6** showed poor solubility which could be dissolved in common organic solvents such as chloroform, toluene, chlorobenzene and dichlorobenzene while **P6** could be dissolved in a more polar solvent *m*-cresol. The new polymer **P6** showed high hole mobility (up to 2.6×10^{-2} $cm^2 V^{-1} s^{-1}$) which is two times that of **P2** (up to 1.4×10^{-2} $cm^2 V^{-1} s^{-1}$), due to the self-assembling property of hydrogen bonding, which improves the intermolecular interaction thus better inter-chain connectivity and higher mobility. **P6** based solar cells did not show good performance due to its poor solubility which might not form bi-continuous and interpenetrating morphology in the active layer of solar cells.

Acknowledgements

I would like to show my great thanks to my supervisor, Prof. Yuning Li, who gave me the opportunity to work in his group. His expertise and guidance have helped greatly through my master's study. Moreover, his patience and valuable advice cultivated my research skills and knowledge. Thanks also go to Prof. Xianshe Feng and Prof. Alexander Penlidis who reviewed my thesis and provided valuable comments and advice.

I would like to thank Dr. Bill O'Keefe and Dr. Romain Perrier-Cornet from Canadian General-Tower (CGT) for their valuable advice and help.

I am very much thankful for Dr. Arthur Hendsbee for testing the OTFT device performance, Jenner Ngai for testing GPC, XRD, AFM and film thickness data, Shuyang Ye from University of Toronto for testing some polymers using the MALDI-TOF-MS.

I also would like to thank other colleges in Li's groups, Zhifang Zhang, Pankaj, Xiguang gao, Han Meng, and Wuqi Li. I would not be able to complete this work without their help. Moreover, I would like to thank George Chang, who is co-op student, for his lab maintenance, including updating chemical inventory and disposing chemical wastes. I also would like to thank Mozhgan Sadeghianlemraski from Prof. Hany Aziz's group for testing solar cells while the solar simulator in our lab was down.

I would like to acknowledge the constant support from all my family members and friends.

The work reported herein was financially supported by the Ontario Centre of Excellence (OCE), the Natural Sciences and Engineering Research Council (NSERC) of Canada, and CGT.

Table of Contents

List of Figures

List of Tables

Appendix A

List of Abbreviations and Symbols

AFM: atomic force microscopy

BGBC: bottom gate bottom contact

CV: cyclic voltammetry

D-A: donor-acceptor

DDTS: dodecyltrichlorosilane

DFT: density functional theory

FF: fill factor

FTIR: Fourier-transform infrared spectroscopy

HOMO: highest occupied molecular orbital

HPLC: high performance liquid chromatography

I_{ON}/I_{OFF}: current ON/OFF ratio

Jsc: short-circuit current

λ_{max}: wavelength of incident light with maximum adsorption

L: channel length

LUMO: lowest unoccupied molecular orbital

MALDI-TOF-MS: matrix-assisted laser desorption/ionization-time of flight-mass spectrometry

OTFT: organic thin film transistor

OPV: organic photovoltaic

OSC: organic solar cell

PCE: power conversion efficiency

RMS: root mean square

Rs: series resistance

Rsh: shunt resistance

UV-Vis: ultraviolet-visible

Voc: open-circuit voltage

Vth: threshold voltage

V_G: gate voltage

μ: charge carrier mobility

W: channel width

XRD: X-ray diffraction

Other abbreviations and symbols are defined in the text

Chapter 1 Introduction

1.1 Overview of Solar Cell Technology

Global warming and energy problems caused by fossil fuels have affected sustainable development goals. Furthermore, the world's energy crisis has become severe. Therefore we need to find alternative energy sources which are environmentally-friendly and cost effective.[1,2] Solar energy is one of the most important sustainable energy resources which can satisfy increasingly growing demand of power and energy and reduce carbon emissions.[3]

In the last two decades, a lot of efforts have been made on solar cell research to convert light into electricity, efficiently.[4] The most successful one is the use of semiconducting materials - silicon which have been applied into automotive vehicles and space satellite.[5] Nowadays, the market has been occupied by the inorganic silicon solar cell due to its stability and efficiency. Solar cell development can be divided into three generations. First, Bell laboratories started investigating photovoltaic devices and invented inorganic single-crystal solar cell in 1954; PCE of the device was around 6% based on a P-N junction device.[6,7] Through several years of research and development, Si solar cells have been commercialized and successfully applied to provide power for various energy needs.

Nevertheless, single-crystal silicon based solar cells have been gradually replaced by poly-crystalline silicon. The polycrystalline silicon is cheaper due to its simper manufacturing process, but at the same time, PCE is lower.

Thus, scientists proceeded to research on thin-film solar cell which is the second-generation solar cell. Instead of Silicon energy intensive wafer technology, thin-film solar cell is made by materials such as cadmium indium selenide (CIGS), amorphous silicon and cadmium telluride (CdTe). By changing from silicon to glass substrate increased the production speed up to 100 times and thus the production cost was reduced significantly.[8,9] Moreover, these devices can be processed at lower temperatures and higher automation level. In terms of performance, the efficiency of III/V semiconductors like GaAs and CIGS-cells (the combinations of Cu/In/Ga/Se) can reach to 20%.[10,11] Unfortunately, Cd is toxic and the sources of In and Te on earth are limited.

Due to the scarcity of these rare earth materials, researchers started to research and develop the third-generation solar cells, the dye-sensitized solar cells, all polymer or all organic solid-state solar cells and hybrid solar cells containing inorganic materials with nanostructure or quantum dots.[12,13]

Compared with the first and the second generation, the materials for the third-generation solar cells are versatile. Carbon based organic materials are relatively cheap. And we can tune the absorption and other physical properties very easily compared to the inorganic materials. Moreover, these third generation solar cells are solution processable with excellent potential for a large-scale production, via printing techniques in a roll-to-roll production process.[14] Also, organic solar cells attract more and more attention because their easier fabrication, low-cost and flexibility.[15]

1.2 Structure and Function of an Organic Solar Cells

In 1986, Tang[16] reported the first organic solar cell fabricated by a 3,4,9,10-perylenetetracarboxylic bis-benzimidazole and copper phthalocyanine in a bilayer heterojunction structure as shown in **Figure 1-1**. Under illumination from AM2 solar simulator, the PCE (power conversion efficiency) was 1%.[16] Later, Yu[17] found the incident photon to electron conversion efficiency increased ten times by blending the poly(2-methoxy-5-(2′-ethyl-hexyloxy)-1,4-phenylene vinylene (donor) and fullerene C_{60} (acceptor) in the active layer compared with traditional bilayer devices without blending.[17] This interpenetrating and bi-continuous structure, called a “bulk heterojunction”, enlarges the interface between donor and acceptor which is promising for thin film solar cell. In addition, as shown in **Figure 1-2**, in a perfect mixed donor and acceptor layer, the charge generation can be efficient, but transportation can be very poor. However, in a bilayer structure, charge generation efficiency is low because the separation of the charges takes places at the interface between donor and acceptor.

Through research on morphology optimization and simulations, the structure depicted in **Figure 1-2 (C)** should be the ideal arrangement. In this structure, the width of each domain is two times the diffusion length of excitons, electron and hole pairs, ensuring efficient charge separation. At the same time, donor and acceptor domains are highly ordered facilitating charge

transport.[18] A more realistic depiction of the bulk heterojunction structure is shown in **Figure 1-2 (d)**, in which donor and acceptor domains are interconnected. This active layer can be processed on a large scale by spray-coating, spin-coating, gravure-coating, inkjet-printing, roller-casting etc.[19] In a bulk heterojunction structure, a fine mixture on the nanoscale is important which is a prerequisite for charge separation and electron dissociation.[20] Later, it was found that adding additives and annealing can optimize the morphology.[21] Today, optimization of bulk heterojunction morphology has become a critical issue for improving the efficiency of bulk heterojunction solar cells.

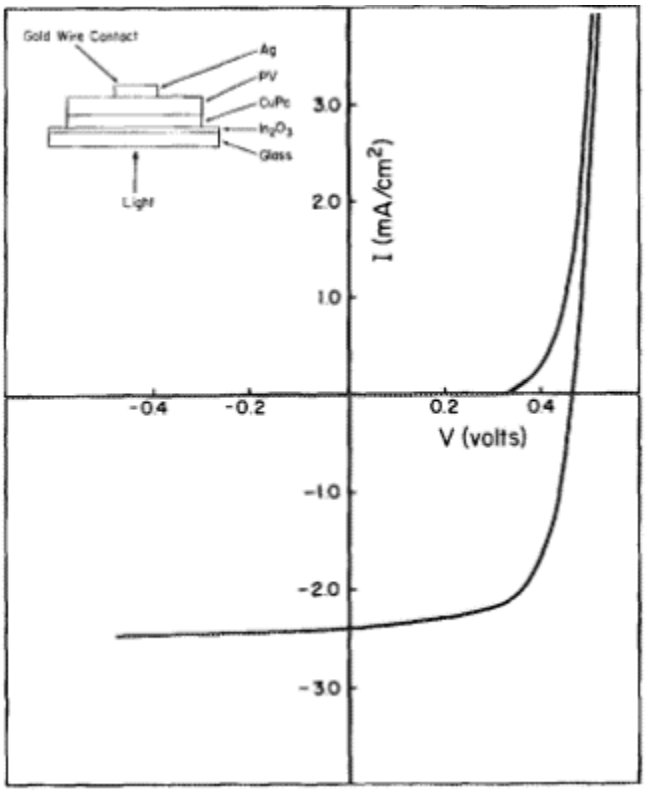

Figure 1-1 Configuration and current-voltage characteristics of an ITO/CuPc (25 nm) IPV (45 nm)/ Ag cell. [16]

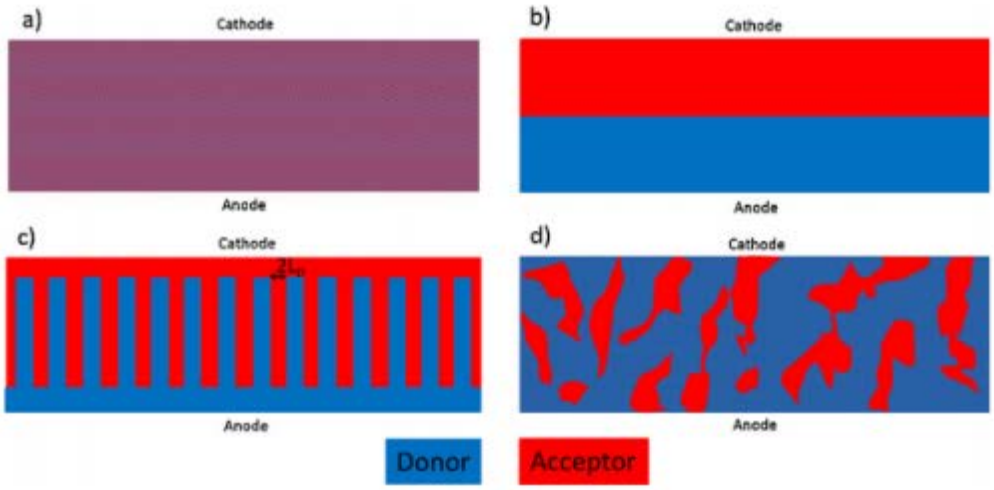

Figure 1-2 (a) Fine mixture of donor and acceptor, (b) bilayer structure, (c) ideal morphology of a bulk heterojunction solar cell and (d) typical morphology of solution processed device. [18]

When organic semiconductors in solar cells absorb energy from light, the electrons cross the bandgap from the valence band to the conduction band. The absorption range of polymer is determined by the band gap. Researchers in the field have been trying to narrow the band gap and get a broader absorption band. The reason for making polymers with a very low bandgap is to match them with the spectral coverage of incident solar irradiation. For example, a polymer is capable of harvesting 30% of solar energy when the band gap is 2 eV, while the material can absorb 77% when the band gap is 1.1 eV. With a comparatively small band gap, the short circuit current (Jsc) of solar cell will be improved but the open circuit voltage (Voc) will be decreased. Voc is determined by the difference between LUMO (lowest unoccupied molecular orbital) of donor material and HOMO (highest occupied molecular orbital) of the acceptor material.

1.3 The State-of-the-art Donors and Acceptors for OSCs

As for donor polymers, polythiophene derivatives, mainly P3HT (poly(3-hexylthiophene)) and poly(phenylenevinylene) (PPV) derivatives such as MDMO-PPV (poly[2-methoxy-5-(3,7-dimethyloctyloxy)]-1,4-phenylenevinylene) are the early classes of polymers. The

development of designing solar cell polymers got a breakthrough by introducing donor-acceptor copolymers.[22] Recently, unlike homopolymer P3HT, by engineering the donor and acceptor units, energy level can be tuned, leading to higher efficiency organic solar cells.[23] The structure of the materials introduced below were shown in **Figure 1-3**. For instance, Yu[24] fabricated solar cell with PDBT-T1: IDIC and PTB7-TH: IDIC and got PCE 9.2% and 5.2%, respectively. Furthermore, Zhao[25] introduced a new donor polymer (PBDB-T-SF) with acceptor (IT-4F) for non-fullerene OSC system, obtaining PCE over 13%. As acceptors, traditional fullerene derivatives such as $PC_{61}BM$ used to attract attention, since they have strong electron accepting ability and enable electron delocalization at the interface of D/A. However, recently, this situation has changed due to insufficient absorption of fullerene derivatives. Then non-fullerene solar cell developed rapidly, which exhibits complementary absorbance and more flexibility in D/A system. Remarkably, in 2015, ITIC was found as an acceptor material and showed high performance, with PCE reaching 10.68% when donor material is PDBT-T.[26] In this thesis work, the acceptors for solar cells will be $PC_{61}BM$ and ITIC.

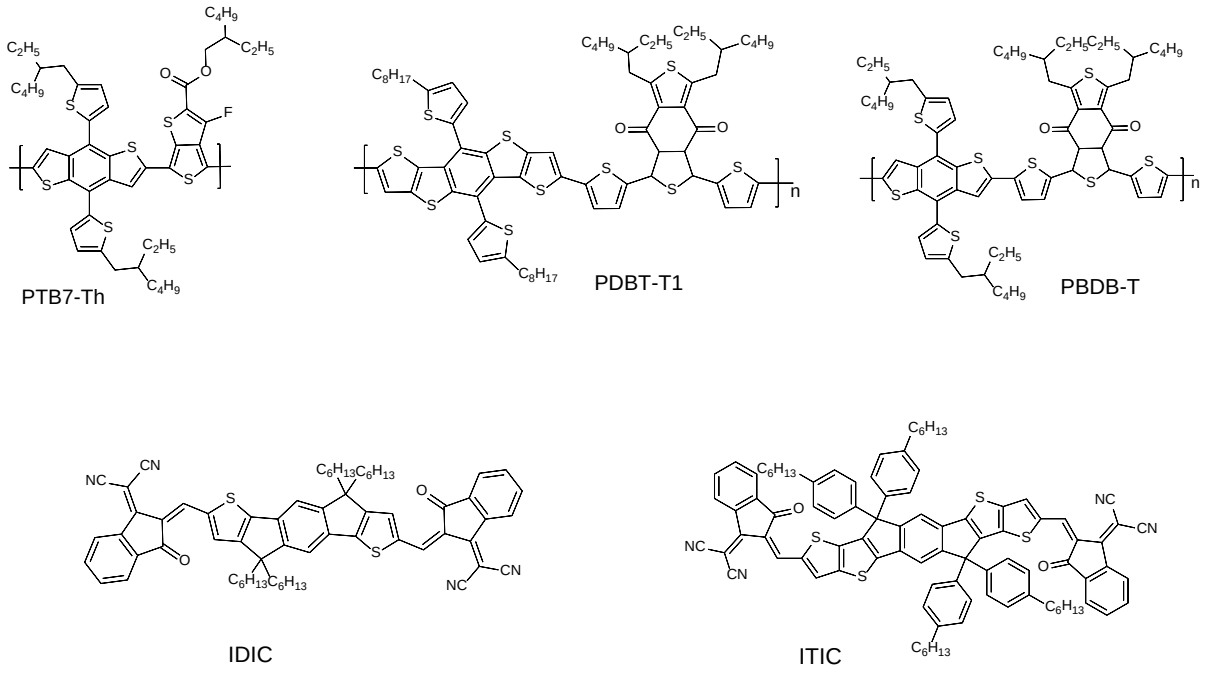

Figure 1-3 Recently reported high performance donors and non-fullerene acceptors for OSCs.

1.4 Basic Working Principles of OSC

The organic solar cell (OSC) like the other conventional solar cells, such as silicon solar cell, absorbs sunlight and generates electricity. The mechanism of generating electricity from sunlight can be divided into five steps:

1. The incident light reaches the active layer of the solar cell.
2. The active layer absorbs the energy of light with appropriate wavelength and generates the exciton (bounded electron and hole pair).
3. The excitons diffuse to the interface of the donor and acceptor where they separate into electrons and holes.
4. The electrons transport through the LUMO of donor to acceptor while the holes transport through the HOMO of acceptor to donor.
5. The holes and electrons are extracted by anode and cathode respectively.

The performance of a solar cell can be characterized by four factors, Voc, Jsc, FF and PCE, which can be described by equation (1):

$$\mathrm{PCE} = \frac{\mathrm{V_{oc}} \times \mathrm{J_{sc}} \times \mathrm{FF}}{\mathrm{P_{in}}} \quad (1)$$

in which the P_{in} is the incident light power, usually used as 100 mW/cm^2, the standard AM1.5G spectrum multiplied by the area of the cell. FF is calculated by equation (2):

$$\mathrm{FF} = \frac{\mathrm{V_{max}} \times \mathrm{J_{max}}}{\mathrm{V_{oc}} \times \mathrm{J_{sc}}} \quad (2)$$

Figure 1-4 shows a J-V curve of a typical solar cell exposed to light. As depicted in the graph, the voltage at which J equals zero is called Voc, which also represents the maximum voltage that can be obtained from the cell. Jsc is the current density when the output voltage is zero in the J-V curve, which also represents the maximum current density that can be obtained from the cell.

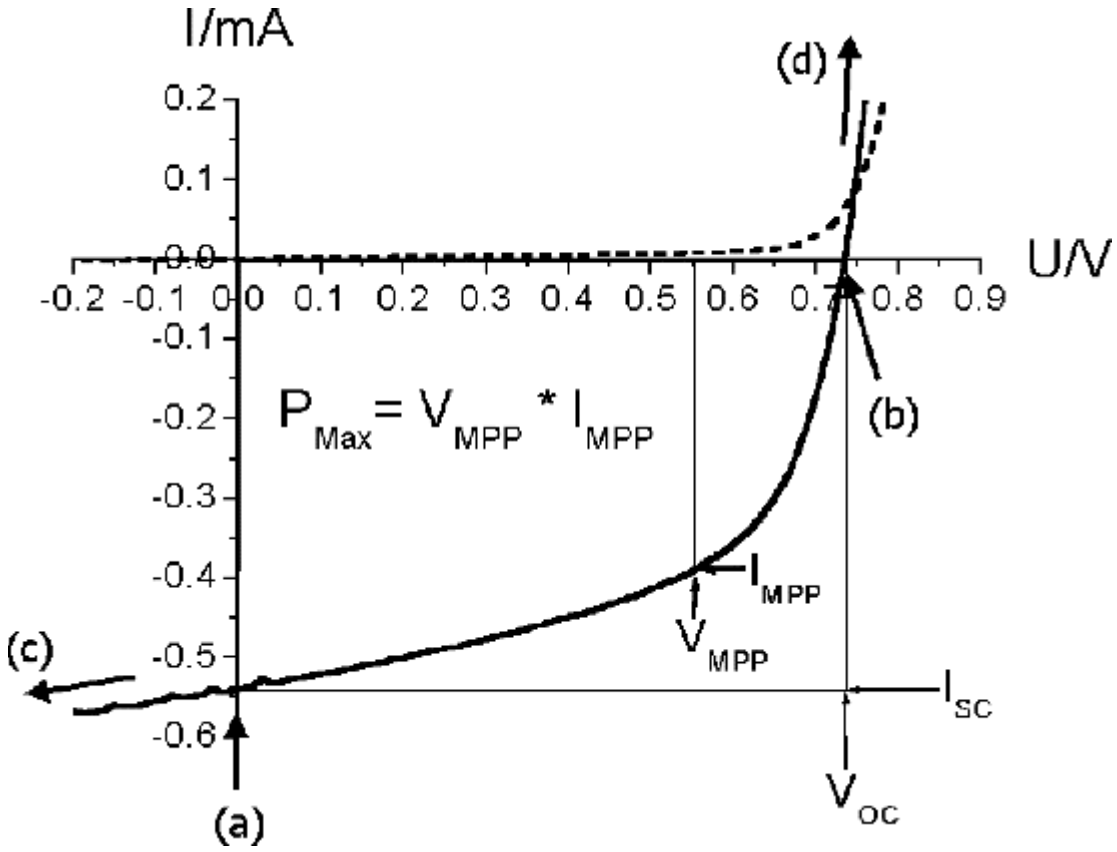

Figure 1-4 J–V curve for a typical solar cell. [27]

For organic solar cells, Cowan proposed an equation for maximum achievable Voc based on both theoretical study and experimental data, the equation (3) was shown below.[28]

$$V_{oc} = \frac{1}{e}(E^{A}_{LUMO} - E^{D}_{HOMO} - \triangle) - \frac{kT}{e}\ln(\frac{N_e N_h}{N_c}) \qquad (3)$$

Where e is the elementary charge, N_e is termed the electron density in the acceptor domains and N_h is termed the hole density in the donor domains under open circuit conditions, N_c is the density of states (DOS) at the respective band edge of the donor and the acceptor. The energy shift, Δ arises from disorder within the phase-separated donor and acceptor domains.

This equation was also verified in the simpler equation by Scharber's work,[29] for a solar cell with an active layer blended with a polymer donor and a fullerene derivative such as $PC_{61}BM$ and $PC_{71}BM$:

$$V_{oc} = \frac{1}{e}(E^{A}_{LUMO} - E^{D}_{HOMO}) - 0.3V \quad (4)$$

The constant value 0.3 V is an empirical factor, mainly influenced by the coulomb attraction between holes and electron for efficient charge separation.

Another factor that can influence PCE is Jsc, which can be simply increased by using low band gap and broad absorption profile semiconductor material to promote more light harvesting and charge generation. In a device, Jsc is determined by the following factors: the charge generation and the charge recombination. Achieving a proper active layer morphology can enhance the current during the transport. As shown in **Figure 1-5**, the donor and acceptor domains should be twice the size of the exciton diffusion length, which is limited to ~10 nm,[30,31] in order to allow excitons to diffuse efficiently to donor-acceptor interface and thus improve the charge dissociation and separation.

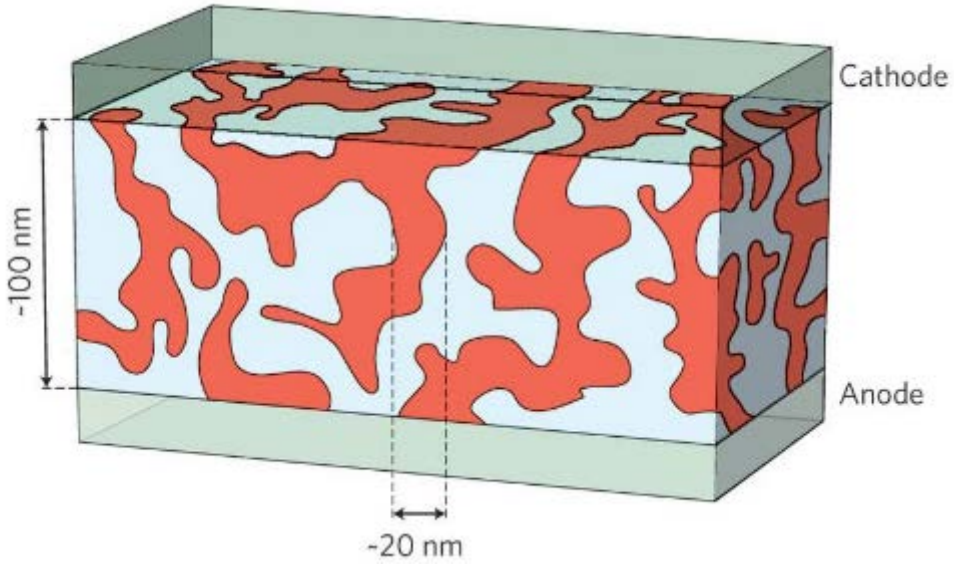

Figure 1-5 Ideal three-dimensional morphology with bi-continuous and interpenetration network of a bulk heterojunction (the polymer donor and the acceptor blending) with top and back electrodes. [32]

Charge generation process takes place in the femtosecond time scale, while the reverse reaction, the charge recombination step, occurs in the microsecond range,[33] as shown in **Figure 1-6**.

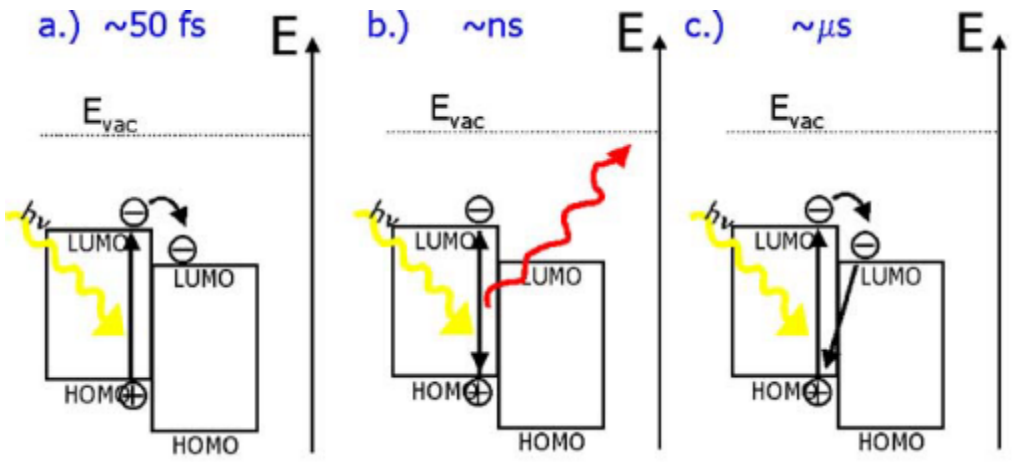

Figure 1-6 Photoinduced processes in donor-acceptor system, (a) charge separate state, (b) photoluminescence and (c) back transfer-recombination.[33]

Apart from the Voc and Jsc, the Rs (series resistance) and Rsh (shunt resistance) also can significantly influence the J-V curve and their values can be calculated through equation (5).

$$J = J_L - J_0 \exp\left(\frac{q(V + JR_S)}{nKT}\right) - \frac{V + JR_s}{R_{sh}} \quad (5)$$

Where J_L is the photocurrent, J_0 is the dark saturation current and n is the ideality of the device. According to this equation, the higher Rs or the lower Rsh is, the lower Voc and FF will become, thus the lower PCE.

1.5 Objective and Structure of This Thesis

A lot of efforts have been made for improving the PCE of OPVs. Despite the fact that the highest PCE of 17.3% was obtained recently[34] by using tandem strategy, the donor materials they used were costly and the tandem structure made the commercialization even more difficult. In order to make commercialized large area solar cells by using printing through roll-to-roll process, it is important to develop low-cost and stable materials. The polythiophene (PT) derivatives are standard donor materials for polymer solar cell (PSC), the most prominent of which is poly(3-hexylthiophene) (P3HT), which has been intensely studied. It can be noticed

that due to its relatively high HOMO level, the Voc value is low in the solar cell and with stability problems.

In this work, [2,2'-bithiophene]-4,4'-dicarboxamide BTDCA electron-deficient building block was designed and synthesized, by simply attaching alkylamide functional group onto the BT, significantly lowering the HOMO level from -4.9 eV (P3HT) to -5.4 eV. The lower HOMO level can improve stability.

In chapter 2, the design and synthesis of four polymers based on BTDCA electron-deficient building block will be discussed. **P1** and **P2** were synthesized with different lengths of alkylamide chain on the BTDCA and copolymerized with the same comonomer unit, BT. **P3** and **P4** were focused on the same length of alkylamide side chain based on the performance of **P1** and **P2,** and copolymerized with TT and T, respectively. Then the polymers characterized using several techniques such as AFM, XRD, UV-Vis absorption spectroscopy and CV, to study the optical and electrochemistry properties. After that the polymer were used for BGBC OTFTs to investigate their charge transport properties, especially hole mobility. Furthermore, the polymers will be used as donor in OSCs with $PC_{61}BM$ and ITIC as the acceptor, using conventional structure ITO/PEDOT: PSS/Active layer/LiF/Al.

In chapter 3, two polymers based on BTDCA(H) with hydrogen bonding are discussed. The thermal stability, crystallinity, optical and electrochemistry properties were studied systematically using TGA, DSC, XRD, UV-Vis, CV and FTIR. Then the polymer was applied into BGBC OTFTs to study the charge transport property. OSCs results were shown, using these polymers as the donor and $PC_{61}BM$ as the acceptor in conventional structure.

In chapter 4, the conclusions of this thesis work are summarized, and future work is proposed for further study of this work.

Chapter 2 Synthesis and Characterization of BTDCA-based Polymers

2.1 Introduction

Among the polymers which were applied as donor materials for polymer solar cell (PSC), polythiophene (PT) derivatives, especially P3HT has been one of the most intensely studied. The P3HT polymer with uncontrolled coupling can form several different degrees of regioregular isomers, including head-to-tail (HT), head-to-head (HH) and tail-to-tail (TT) shown in **Figure 2-1 (a)**. As a result, four regioisomeric triads in the polymer chain can be formed (HT-HT, TT-HT, HT-HH and TT-HH) shown in **Figure 2-1 (b).**[35–38]

Among the three types of regioregular isomers, the head-to-tail is the most preferred orientation in the polymer as the repeating thiophene unit, forming a more coplanar polymer. Much of the work has been devoted to the synthesis of highly regioregular HT-P3HT, and in 1992, Rieke made the first advance to synthesize this polymer. The device performance is significantly dependent on the degree of regioregularity of P3HT. HT-P3HT exhibits a more planar conformation, high crystallinity, strong intramolecular and intermolecular overlap, resulting in high hole mobility in the single polymer only device (μ_h = 0.1−0.3 cm^2/V s).[39–44] Compared with regiorandom polymers, the regioregular polymers also show an extended range of absorption up to 650 nm, giving a band gap of about 1.9−2.0 eV.

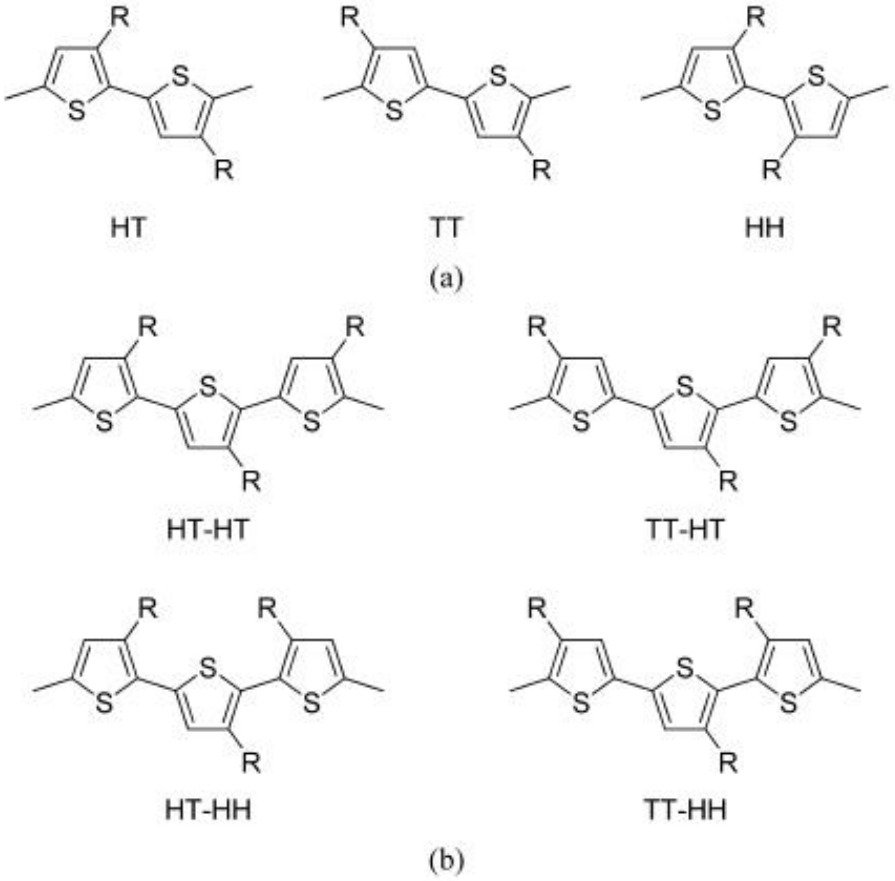

Figure 2-1 (a) Three substituted bithiophenes and (b) isomeric triads.[45]

P3HT has played an important role in promoting developments in the polymer solar cell field. The P3HT based polymer solar cell, combined with the well-known acceptor [6, 6]-phenyl C_{71} butyricacid methyl ester ($PC_{71}BM$) achieved 4% power conversion efficiency under an optimized device fabrication process.[46] However, P3HT has some drawbacks, for example, it has a relative high HOMO level and stability issue. In the polymer solar cell, Voc value is dependent on the difference between the HOMO level of the polymer donor and the LUMO level of the acceptor.[47] The relative high HOMO level results in relative lower Voc and final PCE. A lot of effort has been made to modify the PT derivatives, in order to achieve higher PCE in polymer solar cells, by lowering the band gap to increase the short-circuit current and lowering the HOMO level to increase the open-circuit voltages.[48,49]

It is worth noticing that various π-conjugated molecules containing amide or imide functional groups have caught great attention and been reported in OTFTs and OSCs. For π-conjugated molecules with imide motif, perylenediimide (PDI) and naphthalenediimide (NDI) are among the most popular ones and have been widely studied as building blocks in polymers for OSCs as charge-transporting semiconductors for OTFTs.[50–55] Besides, the molecules with amide motif, isoindigo and diketopyrrolopyrrole (DPP) have been receiving considerable attention as organic semiconductors for a variety of applications, particularly for OTFTs and OSCs.[52,56–58] While introducing the amide side chain, the different lengths of the chain affect the polymer properties. In conjugated polymers, the side chains help to adjust the solubility and determine the intermolecular interaction between different polymer chains and the intramolecular interaction between polymers and small molecules acceptors. In general, long or branched side chains can improve the solubility of polymers more than the shorter chains in the same organic solvent. However, the π-π interchain interaction will be reduced at the same time because of steric hinderance.[59] The grazing incidence X-ray scattering (GIXS) study conducted by Szarko[60] revealed that the reduced π-π interchain interaction will lengthen the π-π stacking distance (*d*-value) resulting in low charge transport character and poor power conversion efficiency of solar cells performances.

In this chapter, a newly designed BTDCA with amide functional group was designed and synthesized. Attaching the amide functional group with its electron withdrawing effect can lower the HOMO level of the D-A polymer which is beneficial for PT derivatives. These polymers usually exhibit planar structures and show excellent chemical, thermal and photochemical stability which is favorable to the fabrication of devices.[61]

The brominated BTDCA will be synthesized with different length of side chains for balancing the solubility and π−π interchain interaction. And this new building block, then was used as an acceptor and BT, TT and T as a donor to form several D-A polymers.

2.2 [2,2'-Bithiophene]-4,4'-dicarboxamide (BTDCA) Monomer

2.2.1 [2,2'-Bithiophene]-4,4'-dicarboxamide (BTDCA) Molecular Design

The work commenced by conducting a computer simulation with density function theory (DFT) on two models, BTDCA-Me and bithiophene-Me whose structures are shown in **Figure 2-2**. The side chain attached on the amide was substituted by methyl groups for simplifying the calculation. During this calculation, the coplanarity, electron distribution, and energy levels of the following molecules was studied. From the simulation results, [2,2'-bithiophene]-4,4'-dicarboxamide (BTDCA) shows small dihedral angle (~22°) between the two thiophenes, which is comparable to that of bithiophene (~20°). The results also show that the electrons in HOMO level and LUMO level are quite evenly delocalized around the two thiophenes, indicating a good π-π stacking along the backbone. What's more important, by attaching amide electron withdrawing groups, the HOMO and LUMO level of [2,2'-bithiophene]-4,4'-dicarboxamide (BTDCA-Me) are -5.8 eV and -1.6 eV, which are lower than the HOMO and LUMO levels of bithiophene-Me, which are -5.4 eV and -1.1 eV, respectively, as shown in **Figure 2-3 (a)** and **(b)**.

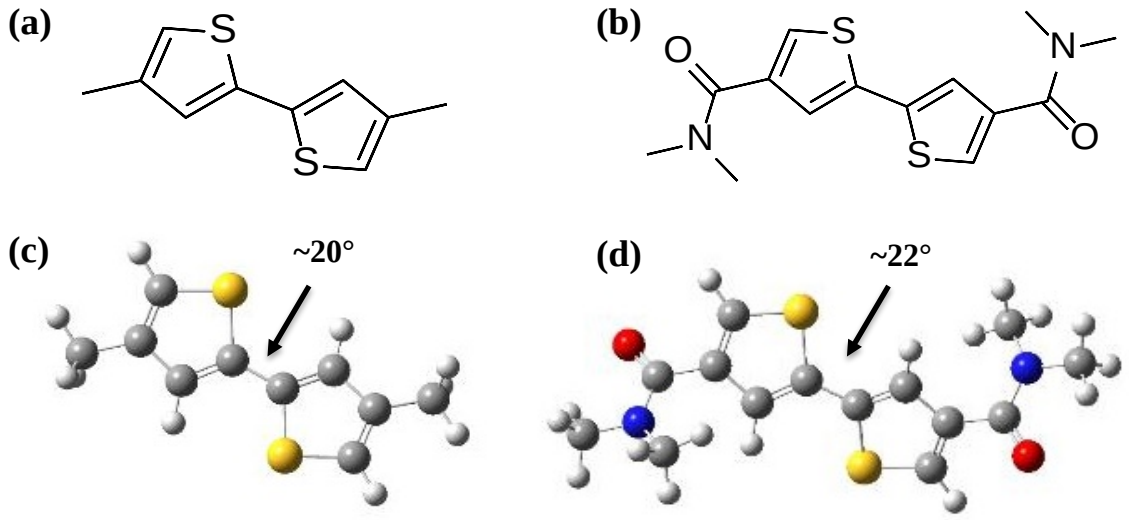

Figure 2-2 The chemical structure of Bithiophene-Me and [2,2'-bithiophene]-4,4'-dicarboxamide (BTDCA-Me) (a) and (c). The calculated geometry of Bithiophene-Me and [2,2'-bithiophene]-4,4'-

dicarboxamide (BTDCA-Me) and their dihedral angle values obtained by computer simulation (b) and (d).

(a)

LUMO = -1.1 eV

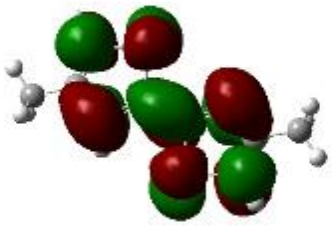

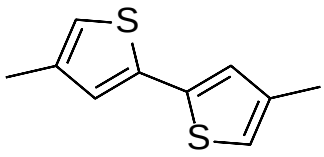

HOMO = -5.4 eV

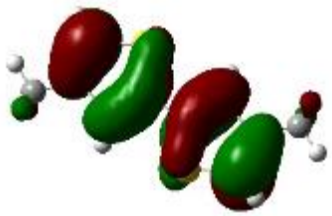

(b)

LUMO = -1.6 eV

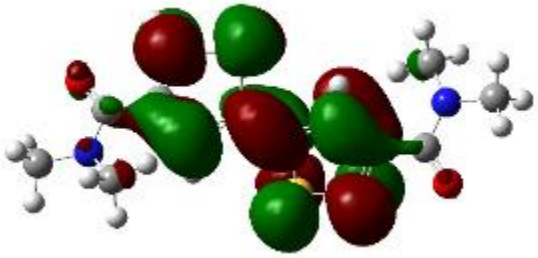

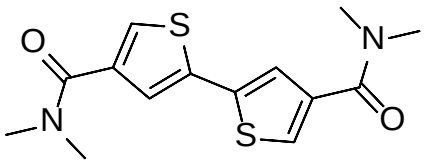

HOMO = -5.8 eV

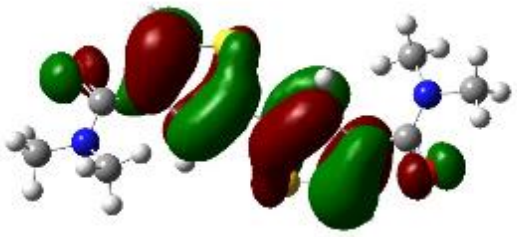

Figure 2-3 HOMO/LUMO orbitals of (a) BT-Me and (b) BTDCA-Me and the calculated HOMO/LUMO levels with respect to vacuum (0 eV).

2.2.2 Synthesis of [2,2'-Bithiophene]-4,4'-dicarboxamide (BTDCA) Monomer

As shown in **Scheme 1**, the brominated BTDCA monomer can be synthesized by several simple reaction and purification steps. The details for materials synthesis are shown in section 2.7.4 and the following NMR spectra are shown in Appendix A.

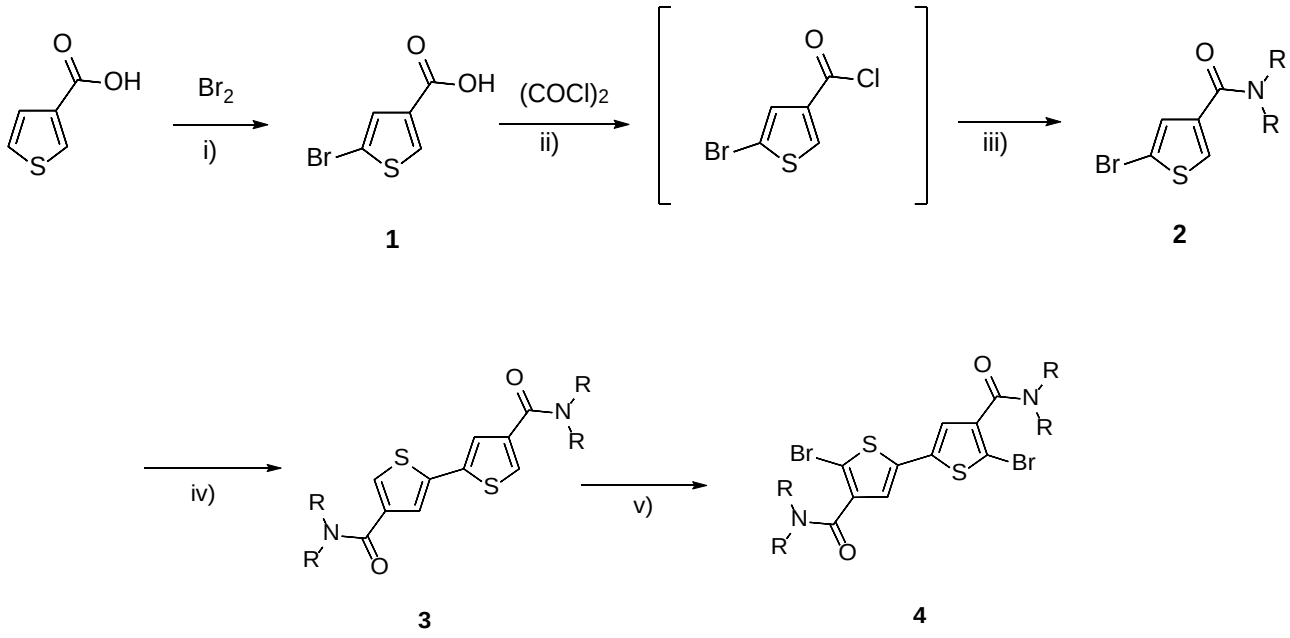

Scheme 1: Synthetic route towards the brominated BTDCA monomer. Reaction conditions: i): acetic acid/ Br_2 /r.t. 49% ii): anhydrous chloroform/ Oxalyl chloride/0 °C to r.t. iii) anhydrous

chloroform/HNR_2/0 °C to r.t. 96% for two steps iv): DMAc/zinc powder/triphenylphosphine/2,2'-bipyridyl/anhydrous nickel (II) chloride/80 °C 57% v): anhydrous chloroform /trifluoracetic acid/NBS/r.t. 95%.

2.3 Synthesis and Characterizations of PBTDCA-BT

2.3.1 Structure Simulation by Density Functional Theory (DFT)

We design the D-A polymer PBTDCA-BT, using BTDCA as an acceptor and BT as a donor. The geometry optimization was conducted on each repeating unit of the PBTDCA-BT by computer simulation based on density functional theory. The side chain attached on the amide was substituted by methyl groups for simplifying the calculation. The orbital surfaces of HOMO/LUMOs of PBTDCA-Me-BT were generated to visualize the electron distribution on the molecular orbitals and the calculated HOMO/LUMO levels with respect to vacuum (0 eV) are shown in **Figure 2-4.**

It is clear from **Figure 2-4** that the electrons are evenly distributed over the whole molecule in both the highest occupied molecular orbital (HOMO) and the lowest unoccupied molecular orbital (LUMO) of the PBTDCA-Me-BT. This indicates that the PBTDCA-Me-BT has high degree of conjugation.

(a)

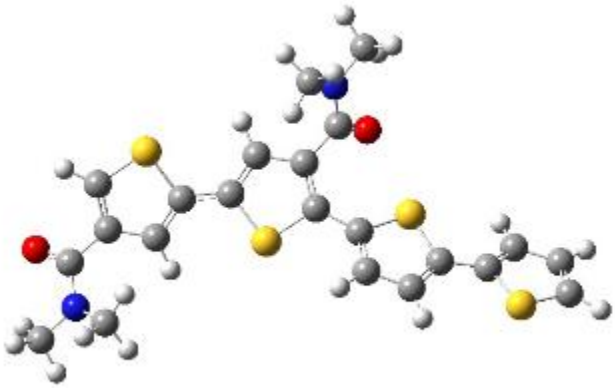

(b)

LUMO = -1.9 eV

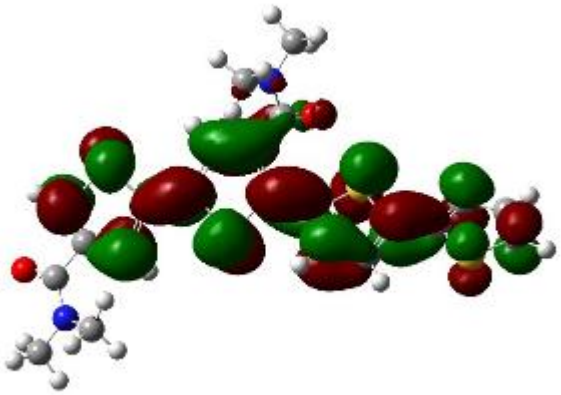

(c)

HOMO = -5.2 eV

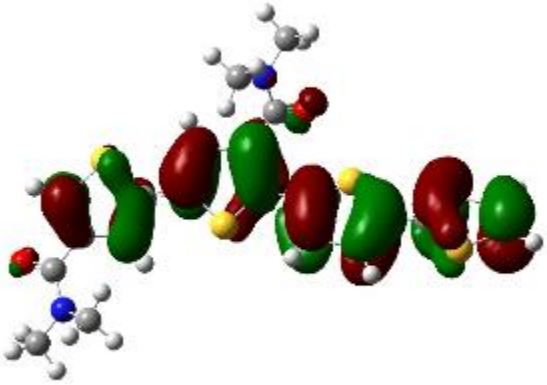

Figure 2-4 (a) Optimized geometry of PBTDCA-Me-BT. (b) HOMO/(c) LUMO, orbitals of PBTDCA-Me-BT and the calculated HOMO/LUMO levels with respect to vacuum (0 eV).

2.3.2 Synthesis of PBTDCA-BT with Different Length of Side Chains

As shown in **Scheme 2, PBTDCA-BT** based two polymers were prepared via Stille coupling polymerization of BTDCA with 5, 5'-bis(trimethylstannyl)-2,2'-bithiophene, and purified using Soxhlet extraction. Both polymers showed quite good solubility in several solvents such as chloroform, chlorobenzene and 1,2-dichlorobenzene. The synthesis procedures are shown in section 2.7.4 and the following NMR spectra are shown in Appendix A

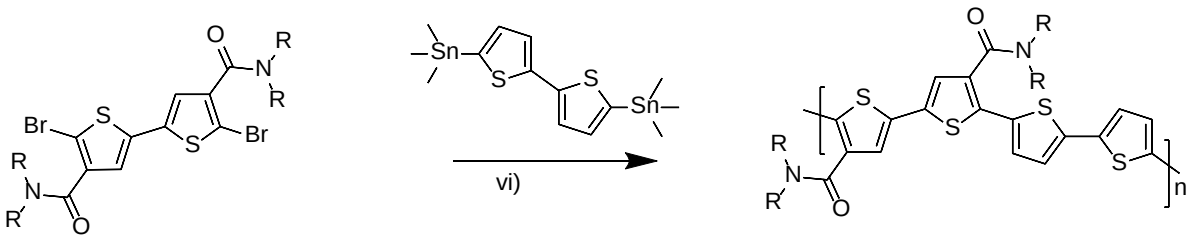

PBTDCA-BT

P1 R= C_6H_{13}

P2 R= C_4H_9

Scheme 2: Reaction condition vi): 5, 5'-bis(trimethylstannyl)-2,2'-bithiophene/anhydrous chlorobenzene/ $Pd(PPh_3)_4$ (5%). Yield: 80% for **P1** and 78% for **P2** in chloroform**.**

2.3.3 Characterization of P1 and P2 by TGA, DSC, UV-Vis, CV, AFM and XRD

The molecular weight of **P1** was measured by gel-permeation chromatography (GPC) at 140 °C with 1,2,4-trichlorobenzene as eluent and polystyrene standards. The number average molecular weight (Mn) and the polydispersity index (PDI) were determined to be 20.3 kDa and 1.7 for **P1 (Figure 2-5),** indicating narrow molecular weight distribution. Since **P2** has shorter polar side chain, we could not obtain the molecular through HT-GPC equipment. MALDI-TOF was used as an alternative way to measure the molecular weight of **P2** and the rest polymers in this work, using a Bruker AutoFlex Speed MALDI-TOF mass spectrometer from a matrix of DCTB (2500:1 matrix-to-polymer ratio) casted from chloroform. The number average molecular weight (Mn) and the polydispersity index (PDI) were determined to be 6.5 kDa and 1.1 **(Figure 2-6)**. The thermal stability is important for the applications of polymers, as the devices might be annealed up to 200 ℃ for the performance optimization. The thermal stability of the polymers was characterized by thermal gravimetric analysis (TGA). A 2% weight loss was observed at 430 °C for **P1** and 441 °C for **P2 (Figure 2-7),** indicating good thermal stability of both polymers and sufficient for the application for OPVs and OTFTs. Neither exothermic nor endothermic transitions were observed in the range of -20 ℃ to 300 ℃

in the differential scanning calorimetry (DSC) measurement of the polymer thin film, suggesting the absence of crystalline domains **(Figure 2-8).**

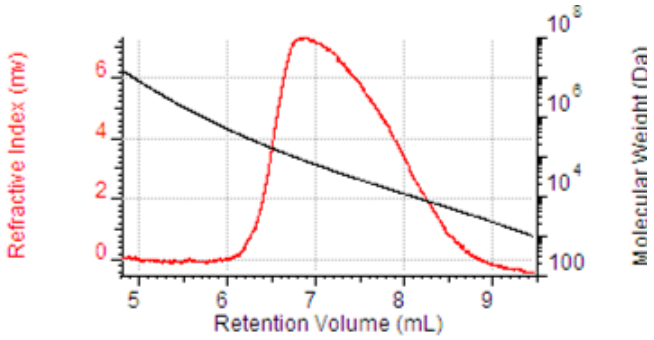

Figure 2-5 The molecular weight distribution of **P1** obtained by HT-GPC at 140 °C with 1,2,4-trichlorobenzene as eluent and polystyrene standards.

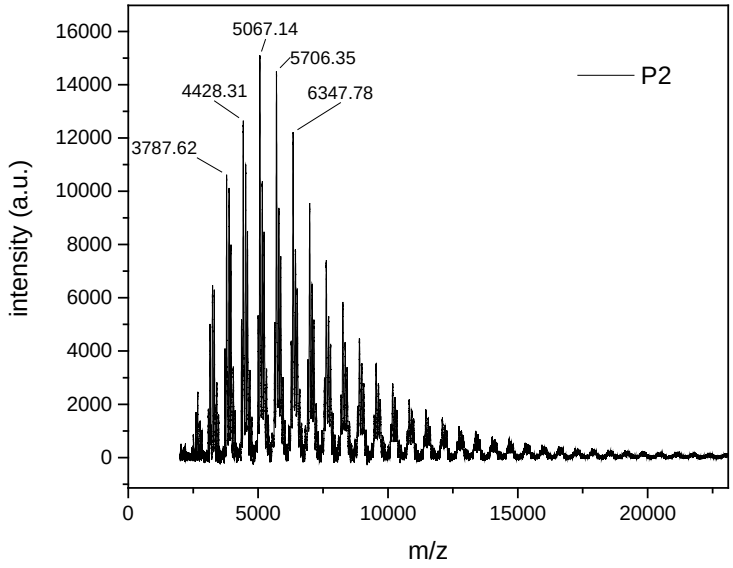

Figure 2-6 The molecular weight distribution of **P2** obtained by MALDI-TOF-MS from a matrix of DCTB (2500:1 matrix-to-polymer ratio) casted from chloroform.

(a) P1

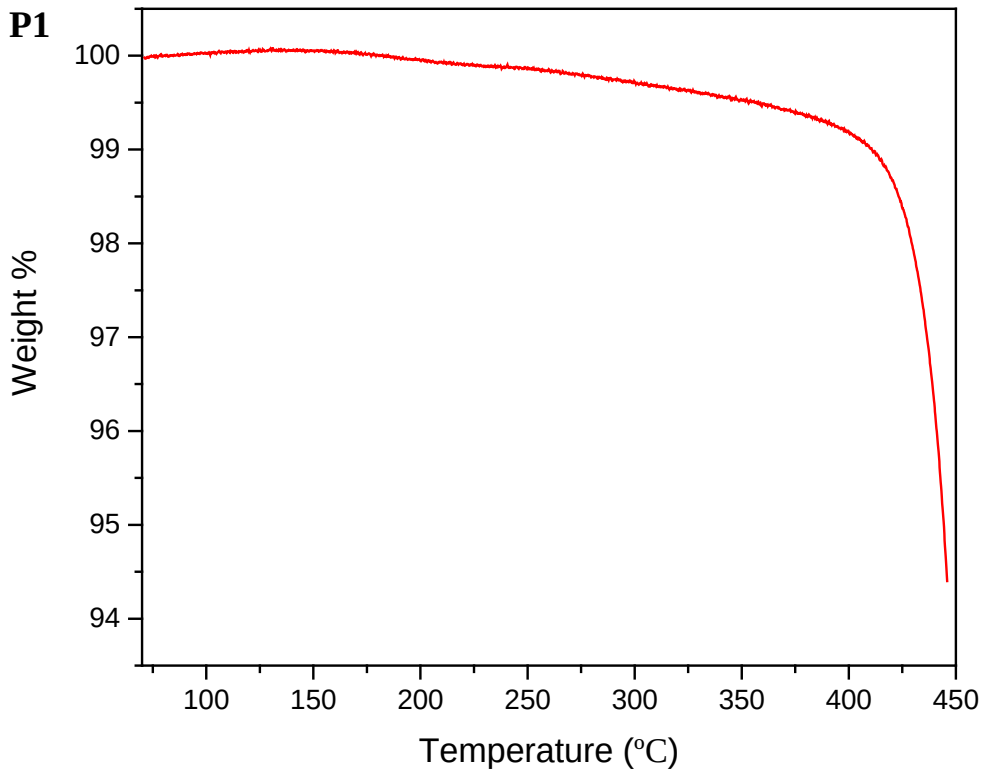
Weight %
100
99
98
97
96
95
94
100
150
200
250
300
350
400
450
Temperature (°C)

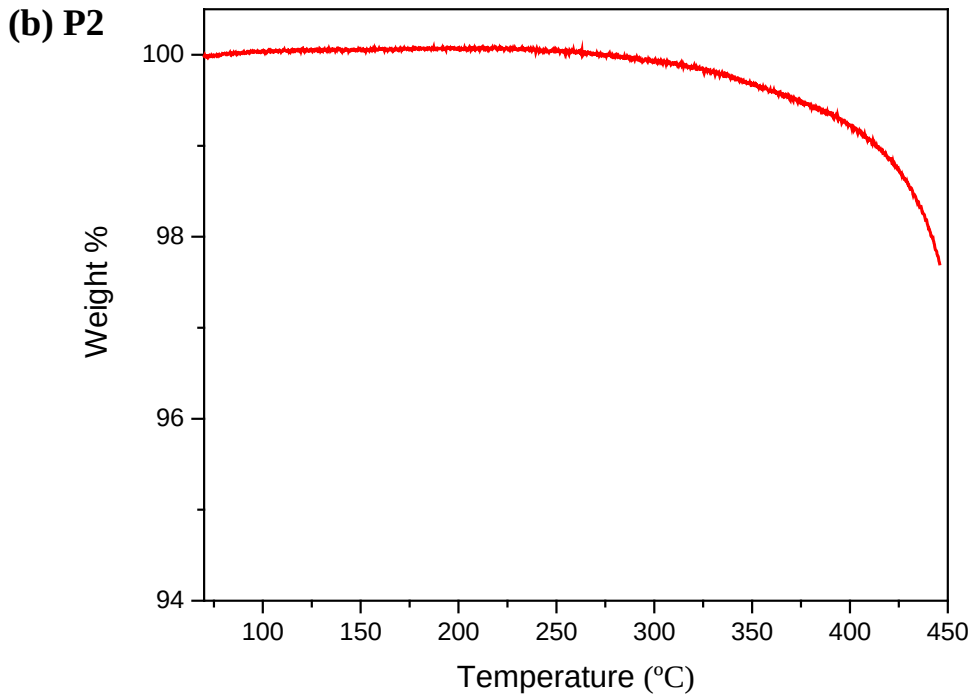

Figure 2-7 The TGA curves of (a) **P1** and (b) **P2** with increasing rate of 10 °C min^{-1} obtained in nitrogen.

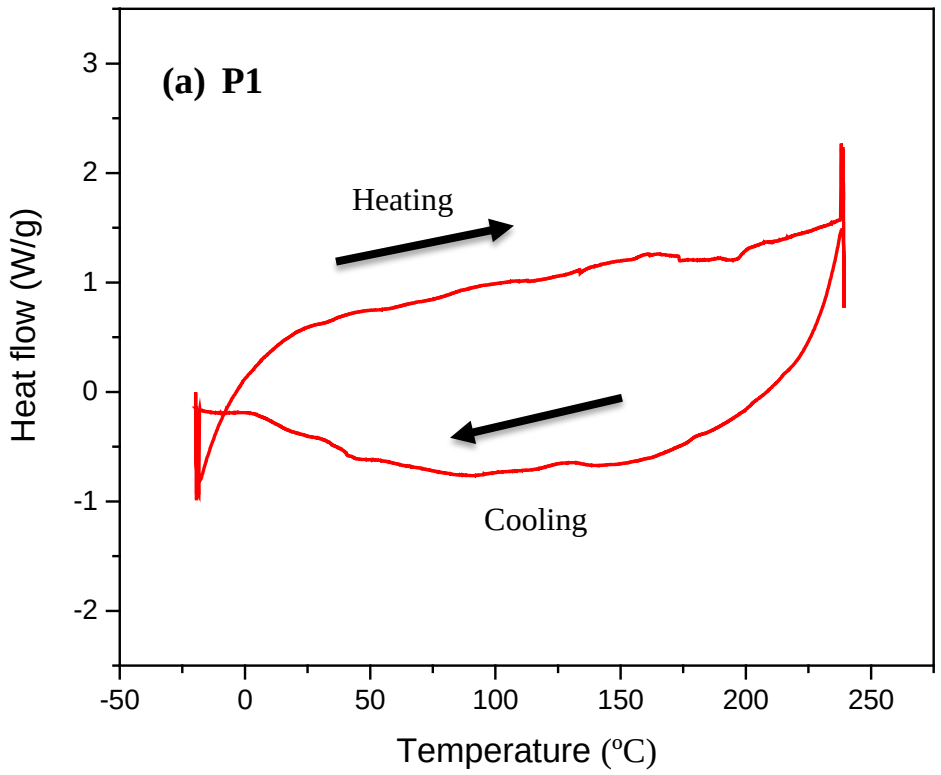
(a) P1
Heating
Cooling
Heat flow (W/g)
Temperature (°C)
3
2
1
0
-1
-2
-50
0
50
100
150
200
250

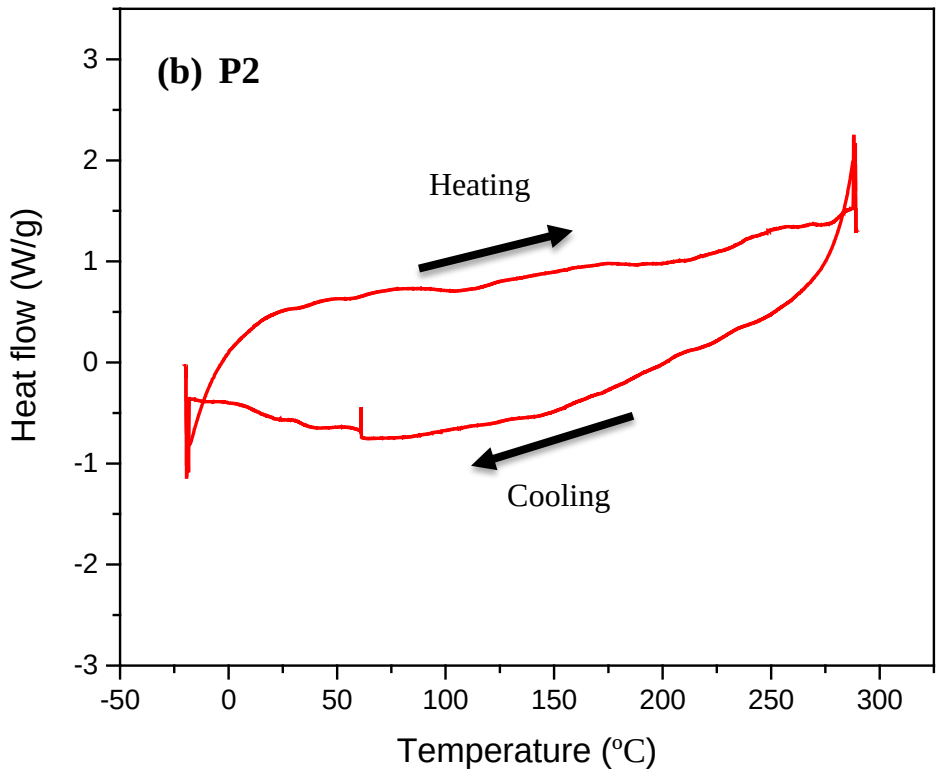

Figure 2-8 DSC profiles of (a) **P1** and (b) **P2** obtained at a scanning rate of 10 °C min^{-1} under nitrogen.

The UV-Vis absorption spectra of both **P1** and **P2** in chloroform solution and in thin films are shown in **Figure 2-9**. Both polymers exhibited single absorption peaks, typical for PT materials.[62] In solution, the maximum absorption wavelengths (λ_{max}) are 487 nm for **P1** and 486 nm for **P2**. The λ_{max} of the **P1** thin film and the **P2** thin film are red shifted to 503 nm and 495 nm, respectively, indicating more extended π-conjugation along the polymer backbone due to planarization of adjacent heterocycles in the solid state. Thus, the optical band gaps in the solid state are slightly decreased compared to those in solution. The optical band gaps of the polymer thin film are calculated to be ~2.06 eV for **P1** and ~2.08 eV for **P2**, respectively, using the thin film absorption onsets. This type of change in the absorption profile upon

solution to thin film transition is common for semiconducting polymers and is often seen in high performance systems.[63]

As mentioned before, the process of charge generation and extraction is said to happen in 5 steps as mentioned in section 1.3.

For efficient charge separation, the LUMO level and the HOMO level of the donor must be higher than that of the acceptor. This is the main reason why cyclic voltammetry method is important for designing a high efficiency solar cell. The LUMO and HOMO level should be carefully chosen for effective charge separation.

For organic semiconductors, HOMO level represents the energy required to extract an electron from a molecule, which is an oxidation process, and LUMO level is the energy necessary to inject an electron to a molecule, implying a reduction process.[64]

In this work, the tetrabutylammonium hexafluorophosphate solution was prepared in HPLC acetone (0.1 mol/L) and used an Ag electrode for reference. During the process, both oxidation and reduction redox were measured to get the $E_{ox}{}^{onset}$ *and* $E_{red}{}^{onset}$ value. Ferrocene, a well-known reference, was also used to calculate the HOMO and LUMO levels by using the equations (6) and (7).

$$E_{HOMO}(\text{eV}) = -\text{e}\,[E_{ox}{}^{onset} - E_{FC/FC^+}] - 4.8\ \text{eV} \quad (6)$$

$$E_{LUMO}(\text{eV}) = -\text{e}\,[E_{red}{}^{onset} - E_{FC/FC^+}] - 4.8\ \text{eV} \quad (7)$$

Cyclic voltammetry (CV) was used to reveal the electrochemical property aspects of the polymers (**Figure 2-10**). By using the oxidative onset potentials, the HOMO levels were estimated from the oxidation onset potentials to be -5.4 eV for both **P1** and **P2**. The HOMO levels of P3HT is estimated to be -4.9 eV.[65]

From the CV results, by attaching electron-withdrawing amide substituent to the side led to the decrease in the HOMO levels of **P1** and **P2.** The HOMO levels decreased by 0.5 eV in comparison with P3HT. This is beneficial for achieving higher Voc and is in line with theoretical predictions.

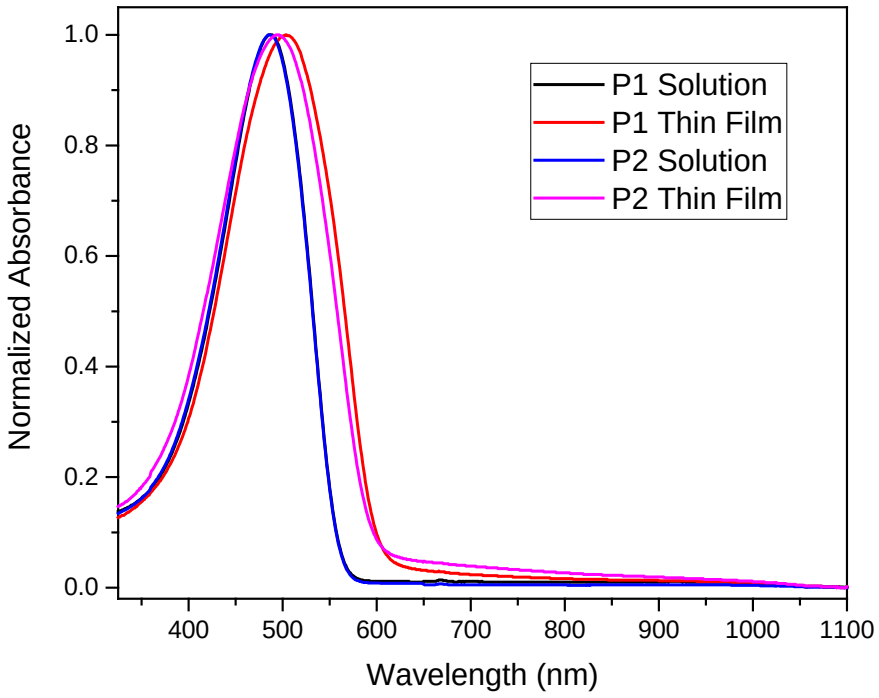

Figure 2-9 Normalized UV-vis absorption spectra of **P1** and **P2** in solution and in thin film.

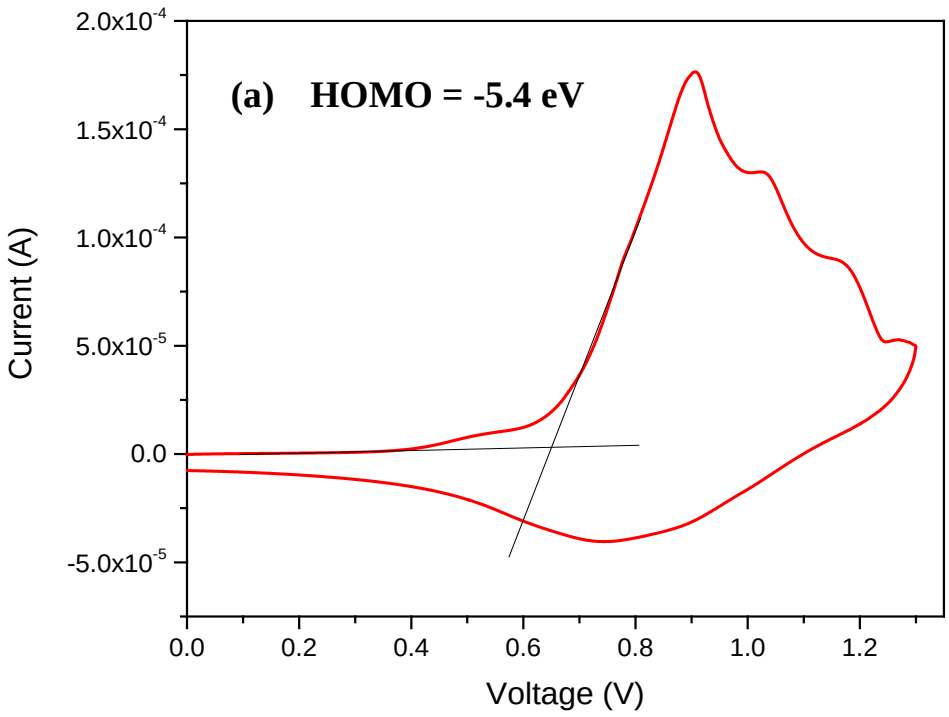
(a) HOMO = -5.4 eV
Current (A)
Voltage (V)
2.0x10-4
1.5x10-4
1.0x10-4
5.0x10-5
0.0
-5.0x10-5
0.0
0.2
0.4
0.6
0.8
1.0
1.2

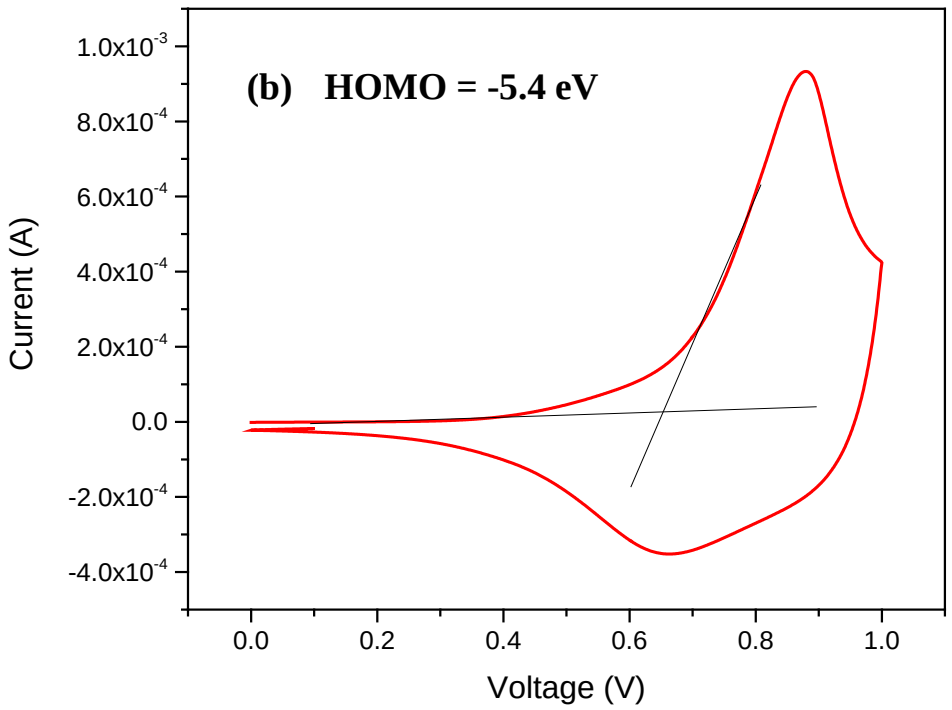

Figure 2-10 The CV diagrams of (a) **P1** and (b) **P2** at a scan rate of 0.1 V/s. The electrolyte was 0.1 M tetrabutylammonium hexafluorophosphate in anhydrous acetonitrile.

The surface morphology of **P1 (Figure 2-11)** and **P2 (Figure 2-12)** spin-coated on dodecyltrichlorosilane (DDTS)-modified SiO_2/Si substrates was examined by AFM. The samples were annealed at different temperatures for 20 min under nitrogen. From the depth profiling images, both **P1** and **P2** seem to have similar surface roughness. The surface roughness for both **P1** and **P2** thin films were dropped when the films were annealed at 100 ℃, evident from the scale for the height which dropped from 30 nm at RT to ~15 nm at 100 ℃. This might have been caused by the rearrangement of packing of the polymer chains. No significant increase in the grain size was observed as the annealing temperature increased from RT to 150 ℃. For the **P1** thin film annealed at 200 ℃, the spherical spots on the surface for **P1** may have been caused by the melting of the amide side chains. **P2** shows similar

morphology at 100 ℃ and 150 ℃. Overall, the grain size is ~500 nm, which is too large for the efficient carrier transport in OPVs.

The packing characteristics of thin films of both polymers were characterized by XRD measurements, shown in **Figure 2-13**. **P1** showed intense diffraction peaks at 2θ = 4.47° and 4.66° for 100 ℃ and 150 ℃ annealed samples. These correspond to the interlayer lamellar *d*-spacing of 1.97 nm and 1.90 nm, respectively. At 200 ℃, **P1** showed broad diffraction peak, probably due to the melted side chains which corresponds to the AFM image. **P2** exhibited more intense diffraction peaks at 2θ = 5.41° and 5.33° at 150 ℃ and 200 ℃, which respectively corresponds to the interlayer lamellar *d*-spacing of 1.63 nm and 1.66 nm. The results indicate that the packing and planarity of the **P2** films were improved by the annealing process. The more intense diffraction peaks of **P2** as compared to **P1** indicates that **P2** has higher degree of crystallinity than **P1,** which is beneficial for OTFT performance. The presence of longer side chain in **P2** might hinder the stacking property of the polymers. The shorter interlayer lamellar *d*-spacing in **P2** obtained from XRD results might substantiate this side chain interference.

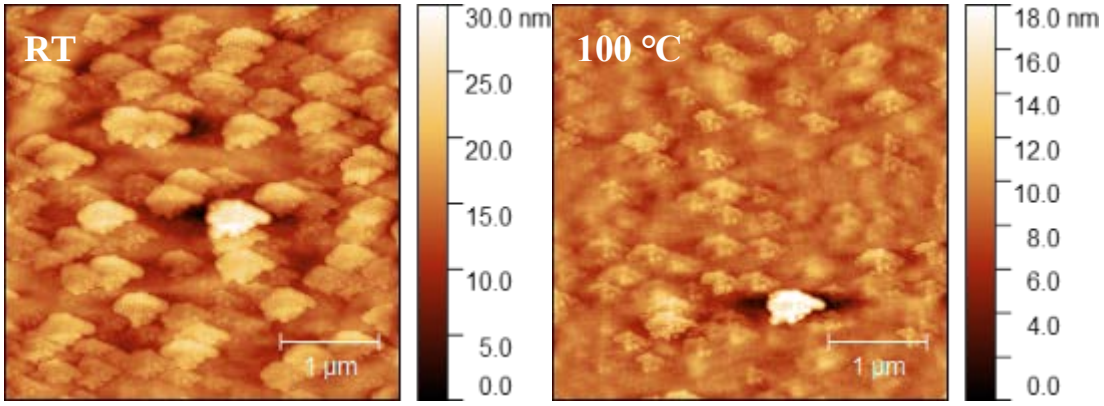

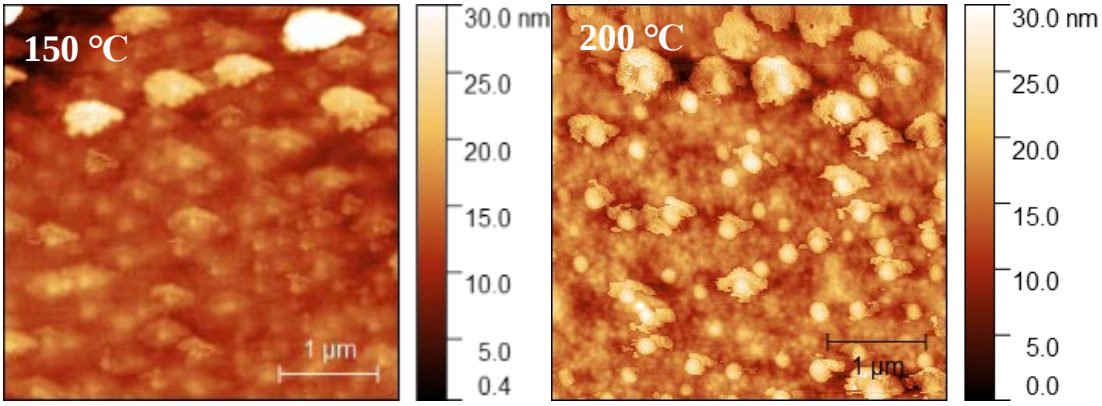

Figure 2-11 AFM height images (4 µm × 4 µm) of **P1** thin films spin-coated on DDTS-modified SiO_2/Si substrates and annealed at different temperatures for 20 min under nitrogen.

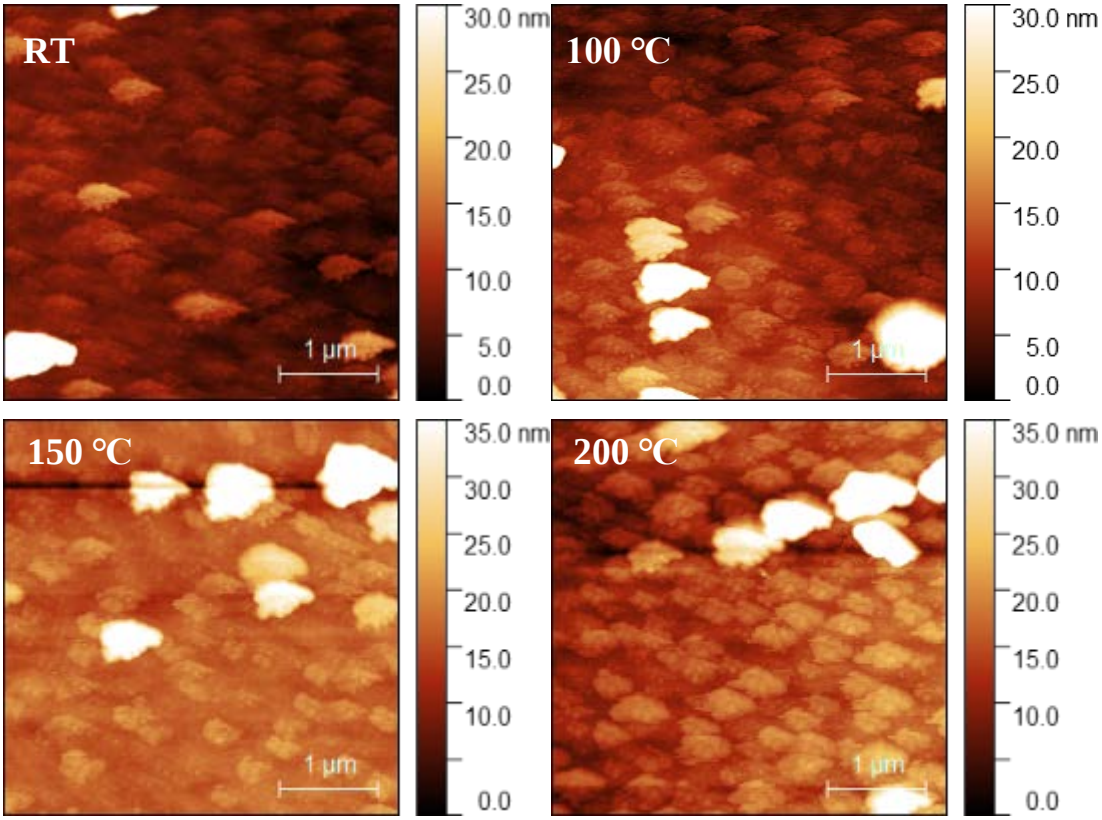

Figure 2-12 AFM height images (4 µm× 4 µm) of **P2** thin films spin-coated on DDTS-modified SiO_2/Si substrates and annealed at different temperatures for 20 min under nitrogen.

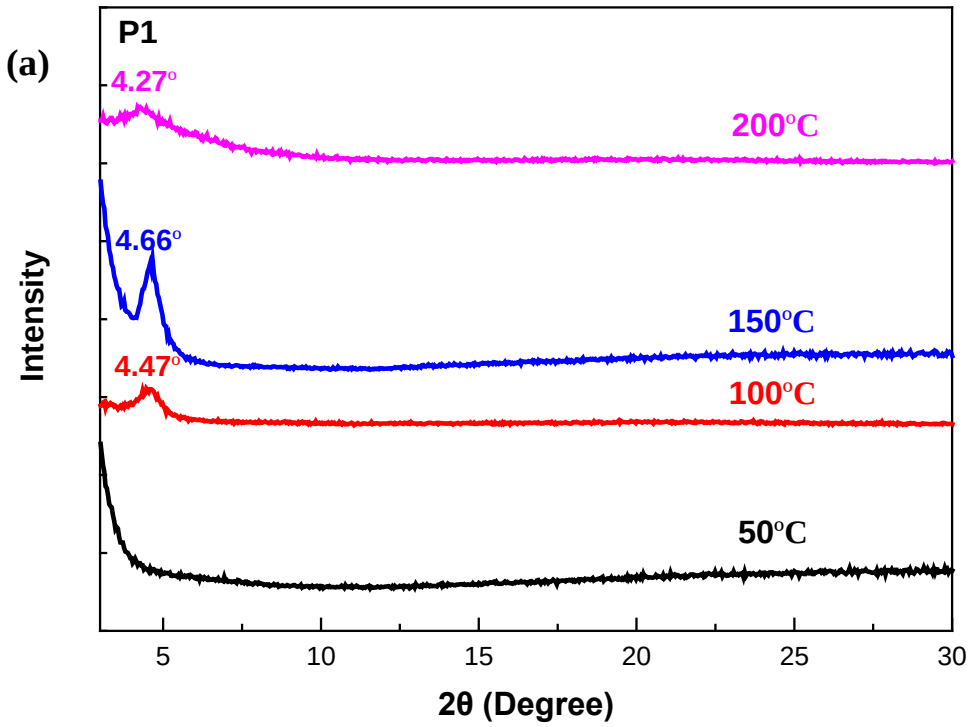
(a)
P1
4.27°
200°C
4.66°
150°C
4.47°
100°C
50°C
Intensity
5
10
15
20
25
30
2θ (Degree)

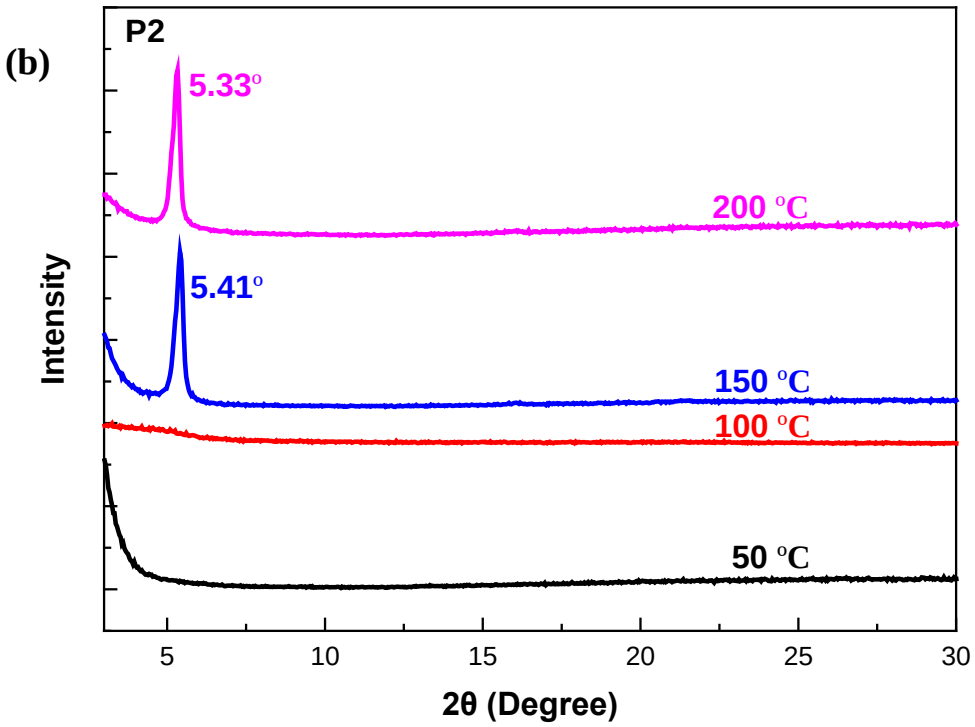

Figure 2-13 The XRD diagrams obtained from the spin-coated (a) **P1** and (b) **P2** thin film on DDTS-modified SiO_2/Si substrates.

2.3.4 OTFT Performances of P1 and P2

The properties of **P1** and **P2** were evaluated as channel semiconductors in BGBC OTFT devices fabricated on DDTS modified SiO_2/Si wafer substrates. The OTFT fabrications and characterizations are shown in section 2.7.2. Both polymers showed p-type charge transport behavior **(Table 2-1)**. For devices based on **P1**, the best overall performance with hole mobility of 0.002 $cm^2 V^{-1} s^{-1}$ was obtained for the 150 °C-annealed films which is ten times the mobility obtained before annealing. The output curve and transport curve were shown in **Figure 2-14**. But after annealing at a higher temperature of 200 °C, the hole mobility dropped to 0.0004 $cm^2 V^{-1} s^{-1}$. These results match the results obtained by XRD and AFM. **P1** with the intense diffraction peak at 150 °C, due to ordered packing at the edge-on orientation, is favorable for

the OTFT device performance, leading to the highest hole mobility for **P1** among the samples annealed at four temperatures. The decrease of hole mobility at 200 °C might have resulted due to melting of the side chain, also confirmed by the broad peak in XRD and the droplet in the AFM image.

For devices based on **P2**, the best overall performance with hole mobility of 0.014 $cm^2 V^{-1} s^{-1}$ was achieved for the 200 °C-annealed polymer films **(Figure 2-14)** which is 40 times the mobility obtained before annealing. Annealing at a higher temperature of 250 °C did not further improve the device performance. **P2** showed sharp diffraction peak in XRD results when the polymer thin films were annealed at 150 °C and 200 °C, indicating highly ordered packing which leads to higher hole mobility than those annealed at RT and 100 °C.

Table 2-1 OTFT device performance of **P1** and **P2** annealed at different annealing temperature.

Polymer	Annealing[a] temperature (°C)	Hole mobility[b] (10^{-3} $cm^2 V^{-1} s^{-1}$)	Vth[c] (V)	$I_{ON/OFF}$
P1	RT	0.19 ± 0.01 (0.21)	-53	10^3
	100	1.0 ± 0.08 (1.1)	-56	10^3
	150	1.7 ± 0.23 (2.0)	-37	10^3
	200	0.3 ± 0.5 (0.4)	-56	10^4
P2	RT	0.29 ± 0.03 (0.33)	-37	10^3
	100	5.8 ± 0.87 (6.7)	-38	10^4
	150	11 ± 1.7 (13)	-38	10^4
	200	14 ± 1.0 (14)	-41	10^5

[a] The devices were annealed in a glove box on a hotplate at the selected temperature for 20 min under argon. Hole mobilities were obtained in the saturated regions in hole enhancement modes. Each set of data were obtained from 3-5 OTFT devices.

[b] The average mobility ± standard deviation (maximum mobility) calculated from the saturation regions of the devices.

[c] The Vth calculated from the device with maximum mobility.

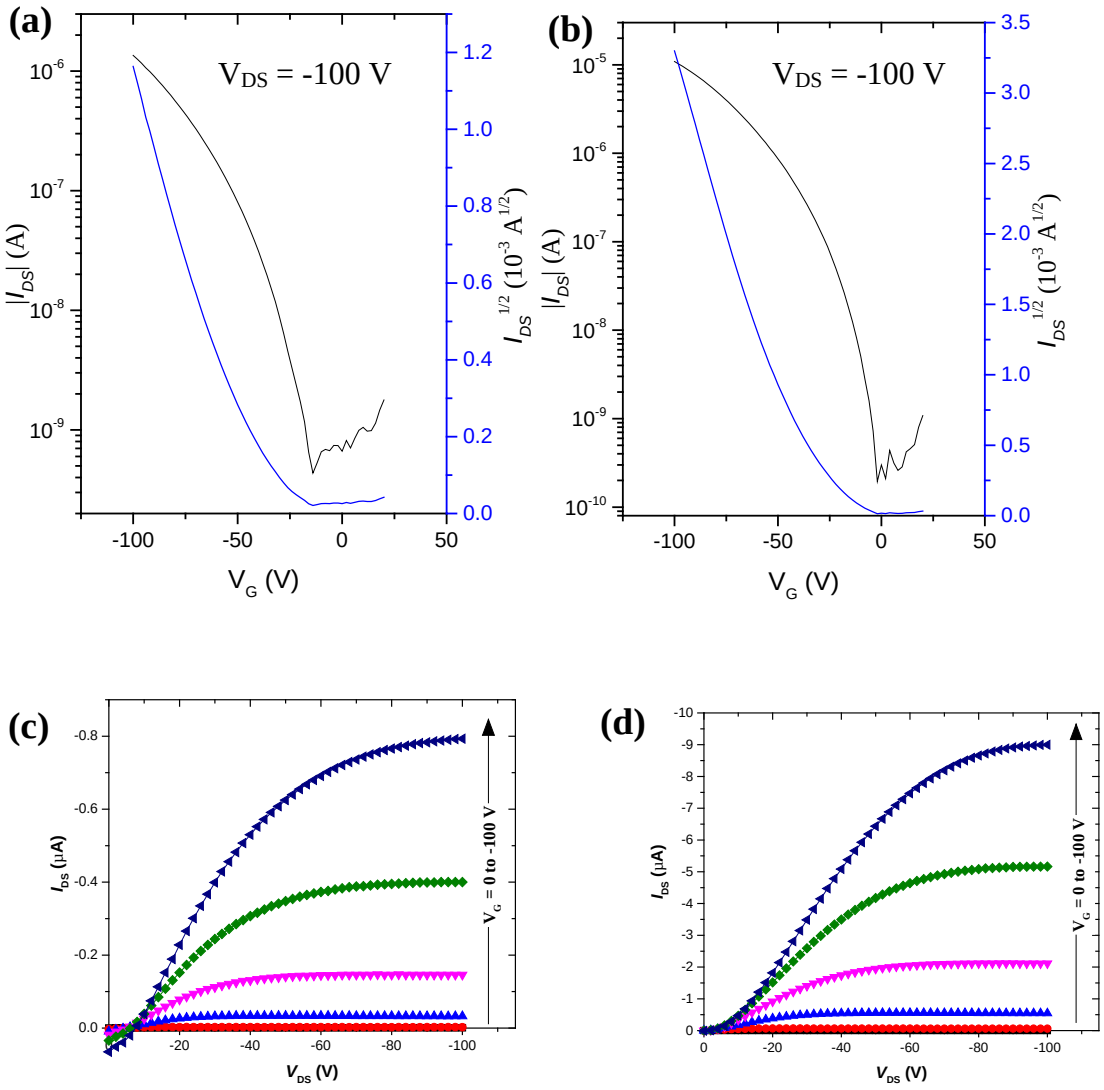

Figure 2-14 The transfer curves for OTFTs based on (a) **P1** and (b) **P2**, and output curves for OTFTs based on (c) **P1** and (d) **P2**. Device dimensions: channel length (L) = 30 μm; channel width (W) = 1000 μm. V_G valued from 0 to -100 V in the step of -20 V in output curves.

2.3.5 OPV Performances of P1 and P2

With reference to the UV-Vis absorbance and HOMO/LUMO of **P1** and **P2**, due to their well-tuned energy level, commercial $PC_{61}BM$ and 3,9-bis(2-methylene-(3-(1,1-dicyanomethylene)-

indanone))-5,5,11,11-tetrakis(4-hexylphenyl)-dithieno[2,3-d:2',3'-d']-s-indaceno[1,2-b:5,6-b']dithiophene (ITIC) were chosen as the acceptor material for the fabrication of solar cells. The OPV fabrications and characterizations are shown in section 2.7.3. The structures for $PC_{61}BM$ and ITIC are shown in **Figure 2-15**. The HOMO/LUMO offset between each donor polymer and acceptor is around 0.3 eV (**Figure 2-16**), which is sufficient for exciton dissociation. The conventional structure ITO/PEDOT: PSS/Active layer/LiF/Al shown in **Figure 2-17** was chosen for the solar cell fabrication.

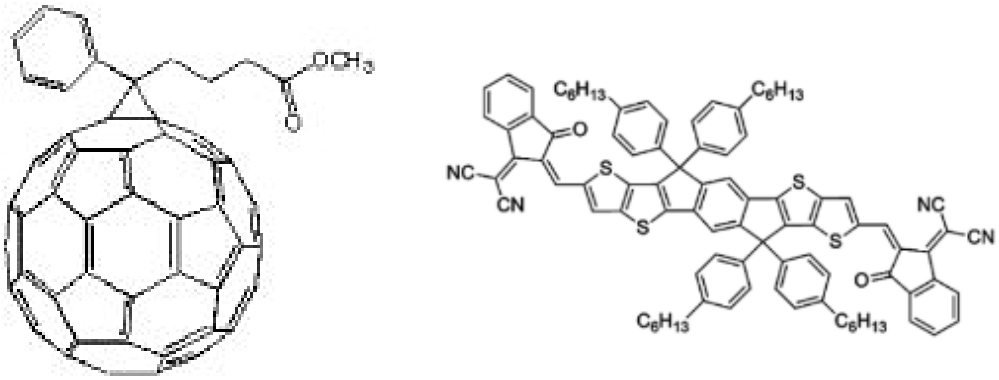

(a) $PC_{61}BM$ **(b)** ITIC

Figure 2-15 The molecular structure of (a) $PC_{61}BM$ and (b) ITIC.

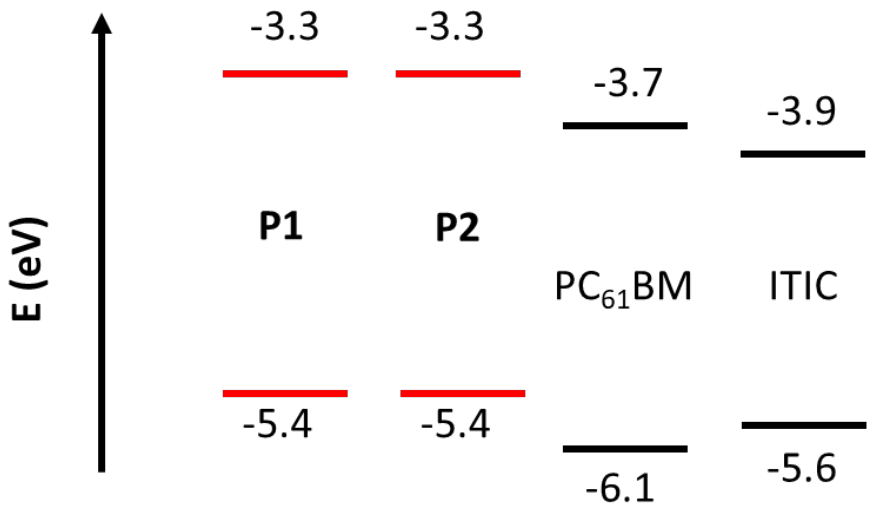

Figure 2-16 The comparison of the HOMO/LUMOs of $PC_{61}BM$, ITIC, **P1** and **P2**.

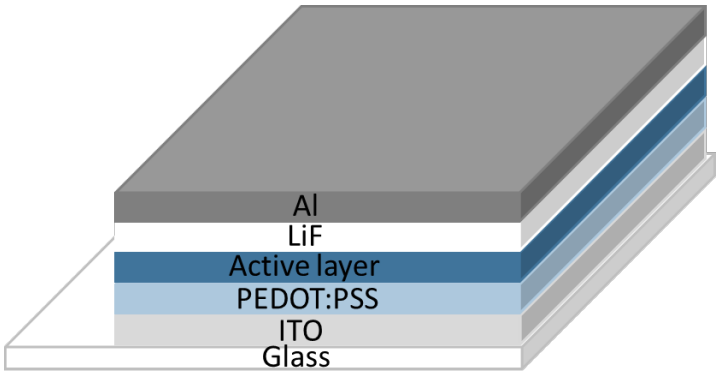

Figure 2-17 Conventional structure for solar cells.

First, we used $PC_{61}BM$ as the acceptor material and changed different solvents, chlorobenzene (CB) and dichlorobenzene (DCB) to test the solar cell performance. The photovoltaic results are summarized in **Table 2-2** and **Table 2-3** and corresponding J-V curves are shown in **Figure 2-18** and **Figure 2-19**. From **Table 2-2** and **Table 2-3**, ~ 0.86 V of Voc was obtained at room temperature for both **P1** and **P2** combined with $PC_{61}BM$ in chlorobenzene or dichlorobenzene. This was 0.36 V (72%) higher than P3HT:$PC_{61}BM$ solar cell (0.5 V)[66] which means by attaching amide electron withdrawing group successfully decreased the HOMO level and

finally gave higher Voc. In **Table 2-2**, the solar cell based on **P2:** $PC_{61}BM$ in CB (PCE = 0.80%) and DCB (PCE = 1.31%) both exhibited higher PCE than **P1:** $PC_{61}BM$ in CB (PCE = 0.72%) and DCB (PCE = 0.7%). For optimizing the solar cells performance, the devices were annealed at 120 ℃ for 10 min, since both **P1** and **P2** showed higher hole mobility after thermal treatment. After thermal treatment, the Jsc, Voc and FF all dropped, thus, lowering PCE. This is probably due to the fact that polymer intrinsically has a high degree of crystallinity. This prompted to form large donor domains during thermal treatment which is harmful for charge separation and transportation. Due to the better performance of **P2** based solar cells, we further optimized **P2** polymer and tuned the weight ratio between **P2** and $PC_{61}BM$. As shown in **Table 2-4** and **Figure 2-20**, a weight ratio of D/A 1.5: 1 and D/A 1: 1.5 were used and the best D/A weight ratio was 1:1, which achieved the highest PCE (1.31%).

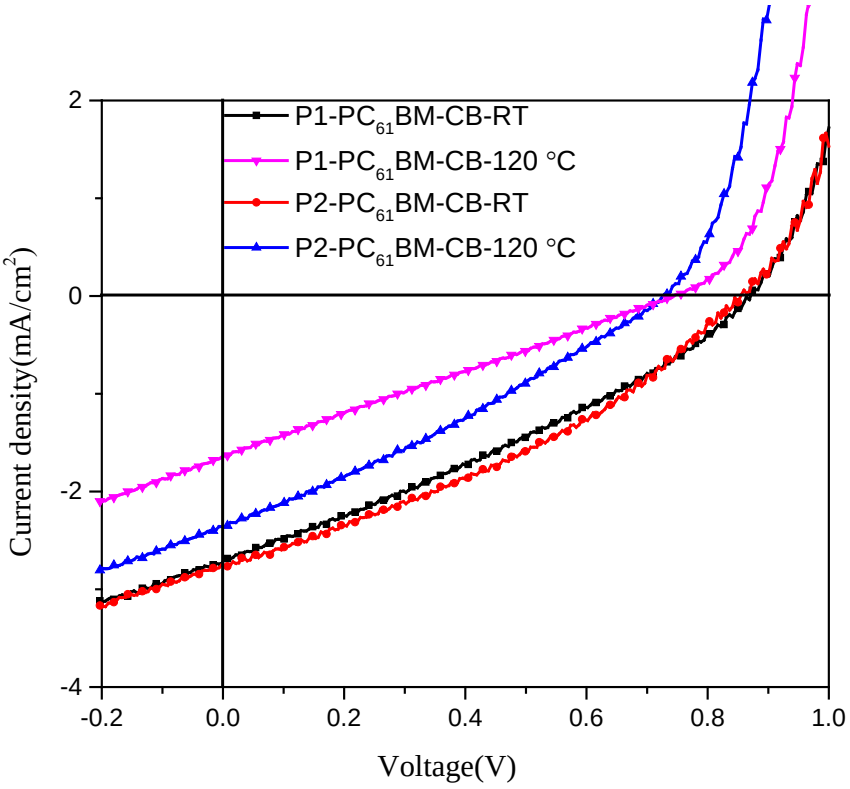

Figure 2-18 J-V curves based on **P1**: $PC_{61}BM$ and **P2**: $PC_{61}BM$ dissolved in chlorobenzene under AM 1.5G illumination.

Table 2-2 Summary of the OPV performance of **P1** and **P2** with $PC_{61}BM$ in CB.

Active layer	Ratio	Solvent	Annealing temperature (℃)	Jsc (mA/cm^2)	Voc (V)	FF	PCE %	Rs (ohm/ cm^2)	Rsh (ohm/ cm^2)
P1: $PC_{61}BM$	1: 1	CB	RT	2.7	0.87	0.31	0.72	319	399
P1: $PC_{61}BM$	1: 1	CB	120 ℃	1.6	0.74	0.25	0.31	430	262
P2: $PC_{61}BM$	1: 1	CB	RT	2.8	0.85	0.34	0.80	149	529
P2: $PC_{61}BM$	1: 1	CB	120 ℃	2.4	0.72	0.29	0.50	187	424

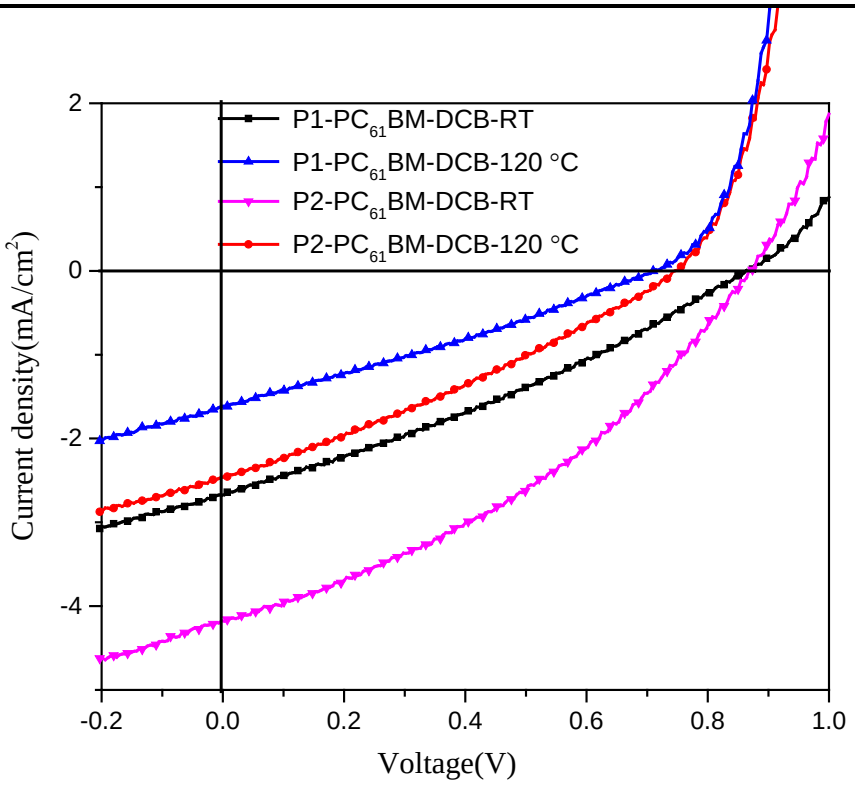

Figure 2-19 J-V curves based on **P1**: $PC_{61}BM$ and **P2**: $PC_{61}BM$ dissolved in DCB under AM 1.5G illumination.

Table 2-3 Summary of the OPV performance of **P1** and **P2** with $PC_{61}BM$ in DCB.

Active layer	Ratio	Solvent	Annealing temperature (℃)	Jsc (mA/cm^2)	Voc (V)	FF	PCE %	Rs (ohm/ cm^2)	Rsh (ohm/ cm^2)
P1: $PC_{61}BM$	1: 1	DCB	RT	2.7	0.86	0.31	0.70	360	457
P1: $PC_{61}BM$	1: 1	DCB	120 ℃	2.5	0.75	0.30	0.55	260	481
P2: $PC_{61}BM$	1: 1	DCB	RT	4.2	0.87	0.36	1.31	87	353
P2: $PC_{61}BM$	1: 1	DCB	120 ℃	1.6	0.71	0.29	0.33	186	452

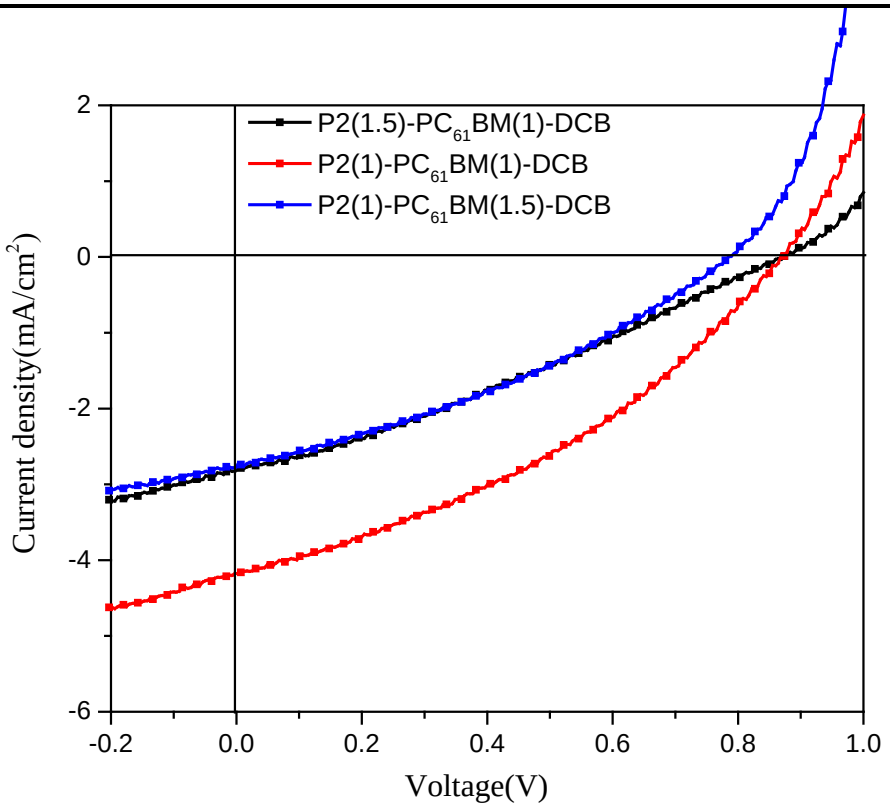

Figure 2-20 J-V curves based on **P2**: $PC_{61}BM$ with different ratio under AM 1.5G illumination.

Table 2-4 Summary of the OPV performance of **P2** with different weight ratios of $PC_{61}BM$ in CB.

Active layer	Ratio	Solvent	Annealing temperature (℃)	Jsc (mA/cm^2)	Voc (V)	FF	PCE %	Rs (ohm/ cm^2)	Rsh (ohm/ cm^2)
P2: $PC_{61}BM$	1.5: 1	DCB	RT	2.8	0.87	0.30	0.73	340	532
P2: $PC_{61}BM$	1: 1	DCB	RT	4.2	0.87	0.36	1.31	87	353
P2: $PC_{61}BM$	1: 1.5	DCB	RT	2.8	0.78	0.34	0.73	268	583

Then, ITIC was used as the acceptor material instead of $PC_{61}BM$, and gave PCE 0.85%, with Jsc = 3.50 mA/cm^2, Voc = 0.81 V and FF = 0.30, as shown in **Figure 2-21** and **Table 2-5**. The morphology was studied by the AFM shown in **Figure 2-22**, the large grains were observed, and the surface roughness was high. This might due to the high degree of crystallinity of **P2**. Thus, the optimal performance was obtained by employing DCB as solvent with the ratio between **P2**: $PC_{61}BM$ as 1:1.

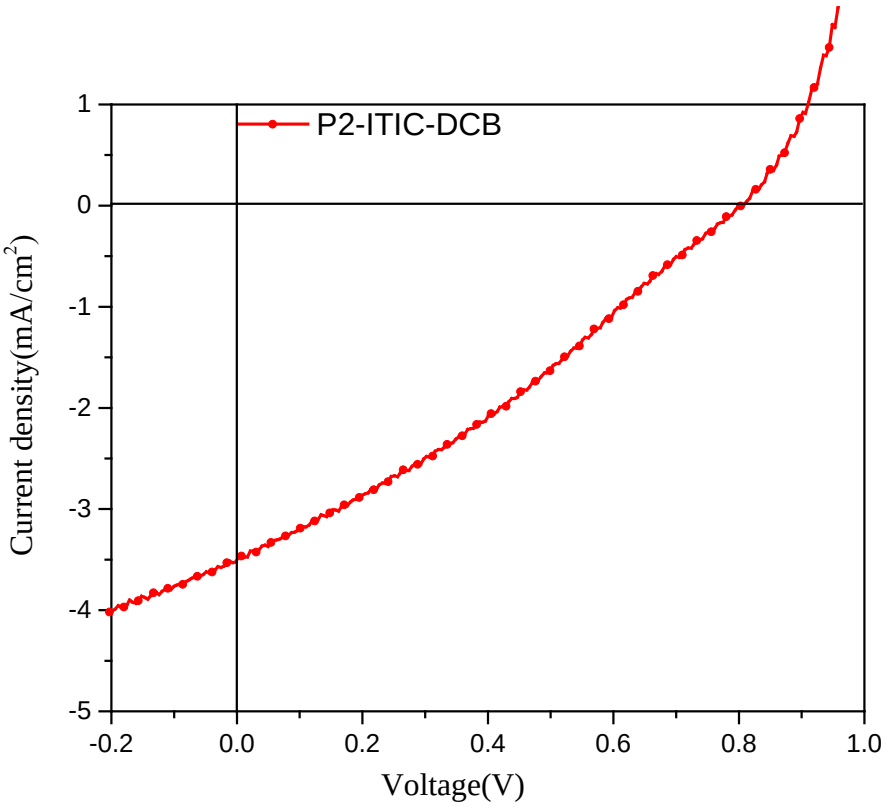

Figure 2-21 The J-V curve based on **P2**: ITIC dissolved in DCB under AM 1.5G illumination.

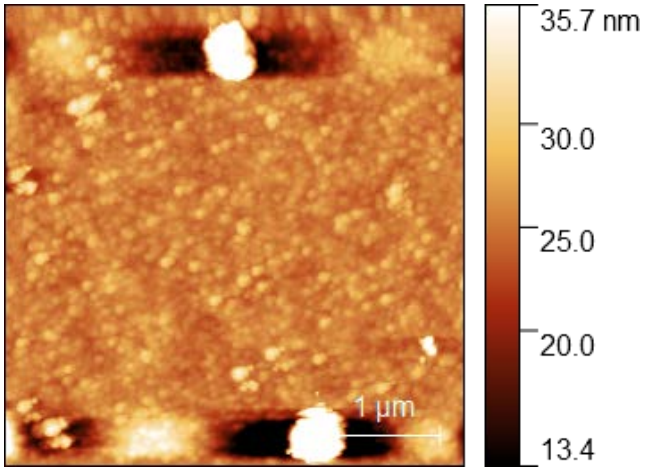

Figure 2-22 The AFM image of surface morphology with surface roughness **P2**: ITIC in DCB (RMS: 4.9 nm).

Table 2-5 Summary of the OPV performance of **P2** with ITIC in CB.

Active layer	Ratio	Solvent	Annealing temperature (℃)	Jsc (mA/cm^2)	Voc (V)	FF	PCE %	Rs (ohm/ cm^2)	Rsh (ohm /cm^2)
P2: ITIC	1: 1	DCB	RT	3.5	0.81	0.30	0.85	269	349

2.4 Synthesis and Characterizations of PBTDCA(BB)-TT

2.4.1 Structure Simulation by Density Functional Theory (DFT)

As the results have shown in section 2.3, **PBTDCA(BB)-BT** has too strong intermolecular interactions and high degree of crystallinity due to its symmetric backbone structure. By introducing smaller size comonomer building block TT into the polymer backbone might disturb the intermolecular packing, thus lowering the degree of crystallinity. The strategy was shown in **Figure 2-23**. In this chapter, we discuss the design of the D-A polymer **PBTDCA-TT (P3)**, using BTDCA as an acceptor and TT as a donor. As TT has similar electron property as BT, the electron property of **P3** might be similar as **P2**.

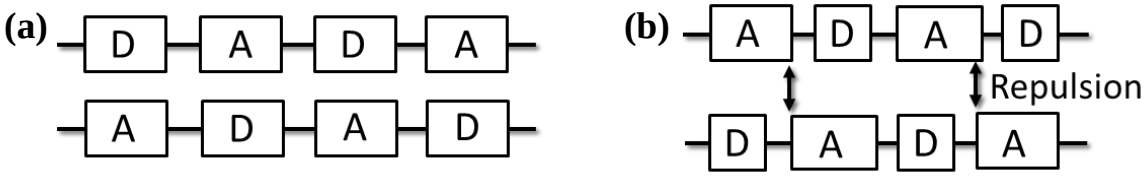

Figure 2-23 (a) Donor and acceptor with similar size. (b) Donor and acceptor with different size.

The geometry optimization was conducted on each repeating unit of the **PBTDCA-TT** by computer simulation based on density functional theory. The carbon chain on the amide of the polymer was substituted by methyl groups for simplifying the calculation as shown in **Figure 2-24 (a)**. The orbital surfaces of HOMO level and LUMO level of PBTDCA-Me-TT were

generated to visualize the electron distribution on the molecular orbitals and the calculated HOMO/LUMO levels with respect to vacuum (0 eV) are shown in **Figure 2-24 (b)** and **(c).**
It is clear from **Figure 2-24 (b)** and **(c)** that the electrons are evenly distributed over the whole molecule in both HOMO and LUMO of the PBTDCA-Me-TT. This indicates that the PBTDCA-Me-TT has sufficient π-π conjugation which facilitates electron transport.

(a)

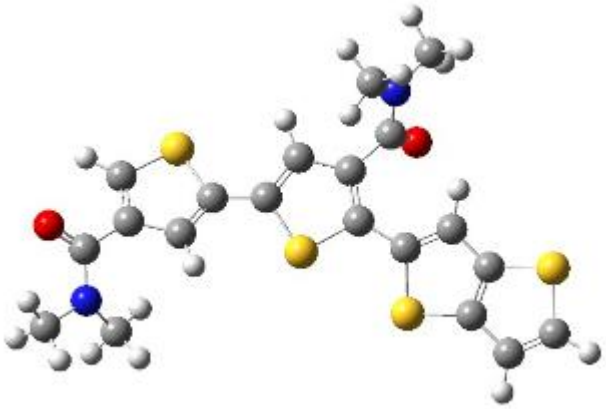

(b)

LUMO = -2.0 eV

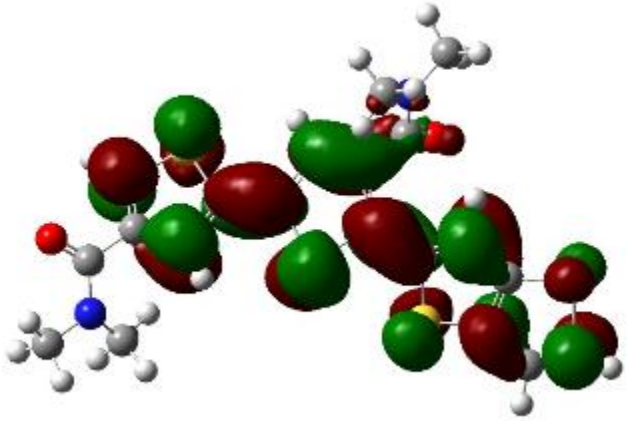

(c)

HOMO = -5.3 eV

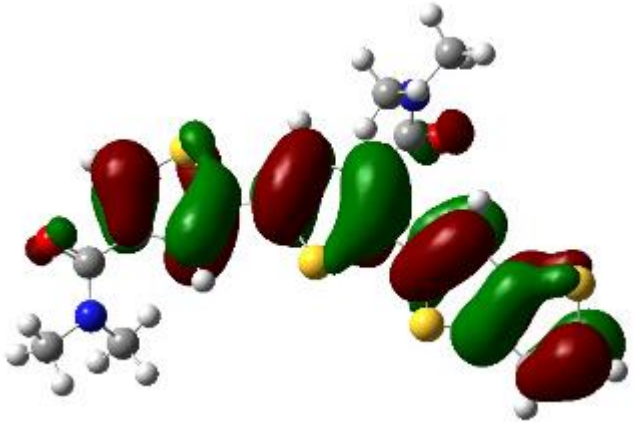

Figure 2-24 (a) Optimized geometry of PBTDCA-Me-TT. (b)HOMO/(c)LUMO orbitals of PBTDCA-Me-TT and the calculated HOMO/LUMO levels with respect to vacuum (0 eV).

2.4.2 Synthesis of PBTDCA(BB)-TT

As shown in **Scheme 3, PBTDCA-TT** was prepared via Stille coupling polymerization of BTDCA with 2,5-bis(trimethylstannyl)-thieno[3,2-b]thiophene, and purified using Soxhlet extraction. **PBTDCA-TT** showed poorer solubility than **P1** and **P2** which can be dissolved in tetrachloroethane, chlorobenzene and 1,2-dichlorobenzene and cannot be dissolved in chloroform.

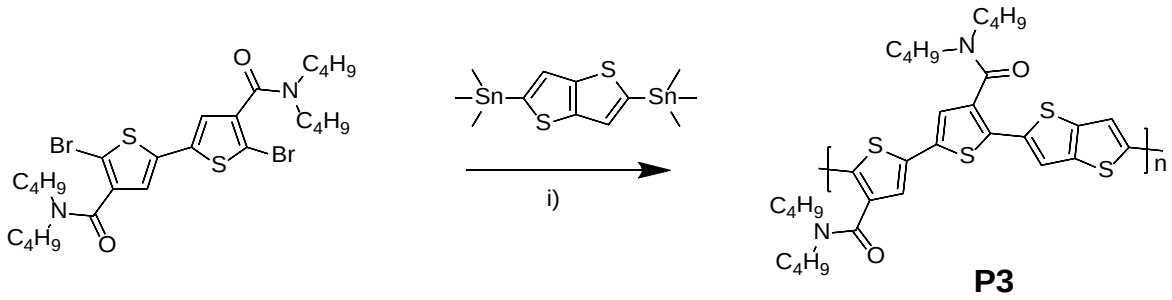

Scheme 3: Synthesis route towards the BTDCA based polymer. Reaction condition: i): Stille coupling 2,5-bis(trimethylstannyl)-thieno[3,2-b]thiophene/anhydrous chlorobenzene/$Pd(PPh_3)_4$ (5%). Yield: 78% in chlorobenzene for **P3**.

2.4.3 Characterization of PBTDCA(BB)-TT by DSC, TGA, UV-Vis, CV, and XRD

The molecular weight of **P3** was measured by MALDI-TOF-MS, using a Bruker AutoFlex Speed MALDI-TOF mass spectrometer from a matrix of DCTB (2500:1 matrix-to-polymer ratio) casted from chloroform. The Mn and the PDI were determined to be 7.7 kDa and 1.1 **(Figure 2-25).** TGA and DSC were used to characterize the crystallization and the thermal stability properties of **P3**. A 5% weight loss was observed at 422 °C **(Figure 2-26)** which is similar to the results obtained for **P1** and **P2**, indicating good thermal stability of this **P3** polymer. From the DSC curve, no noticeable exothermic or endothermic transitions were observed during the range of -20 °C to 350 °C **(Figure 2-27)**.

The UV-Vis absorption spectra of **P3** in solution and in thin film are shown in **Figure 2-28**. **P3** also exhibited typical single absorption peak, which is similar to **P1** and **P2**. In solution, the λ_{max} was 483 nm. The solid thin film of **P3** showed the maximum absorption wavelength at 504 nm, red shifted by 21 nm compared to the λ_{max} in solution. This red-shifting is attributed to the stronger intramolecular and intermolecular D-A interactions in solid state that make the backbone more coplanar and reduce the bandgap. The optical bandgap of the polymer thin film is calculated to be ~2.05 eV, using the thin film absorption onsets.

CV was used to reveal electrochemical property of the polymers (**Figure 2-29**). By using the oxidative onset potentials, the HOMO levels were estimated from the oxidation onset potentials to be -5.4 eV for **P3**.

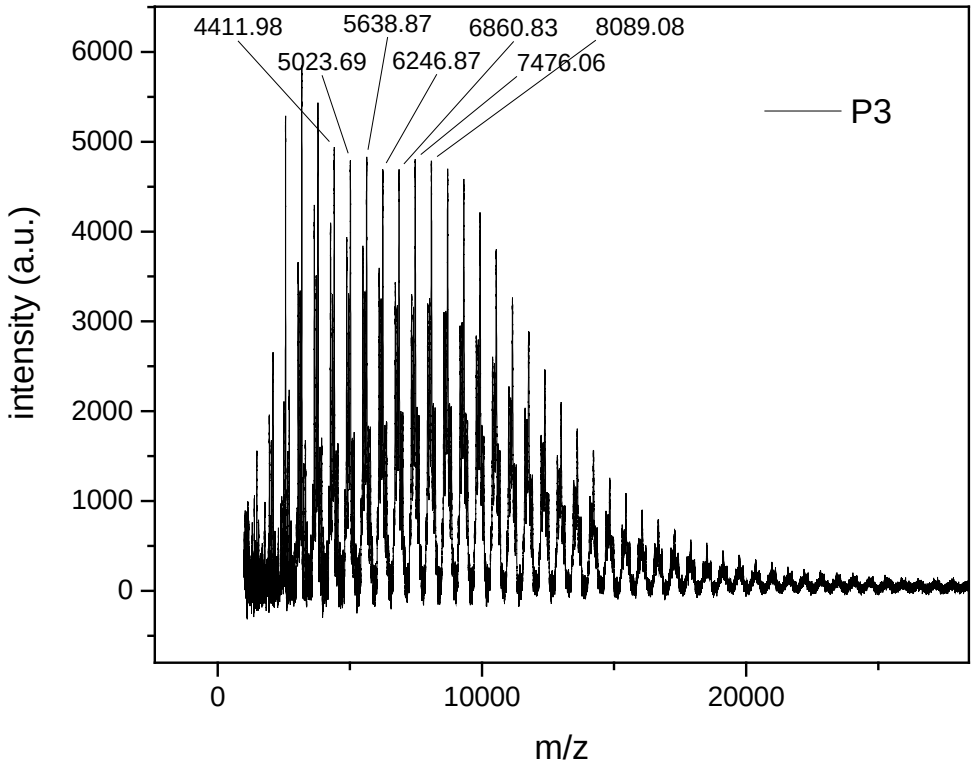

Figure 2-25 The molecular weight distribution of **P3** obtained by MALDI-TOF-MS from a matrix of DCTB (2500:1 matrix-to-polymer ratio) casted from chloroform.

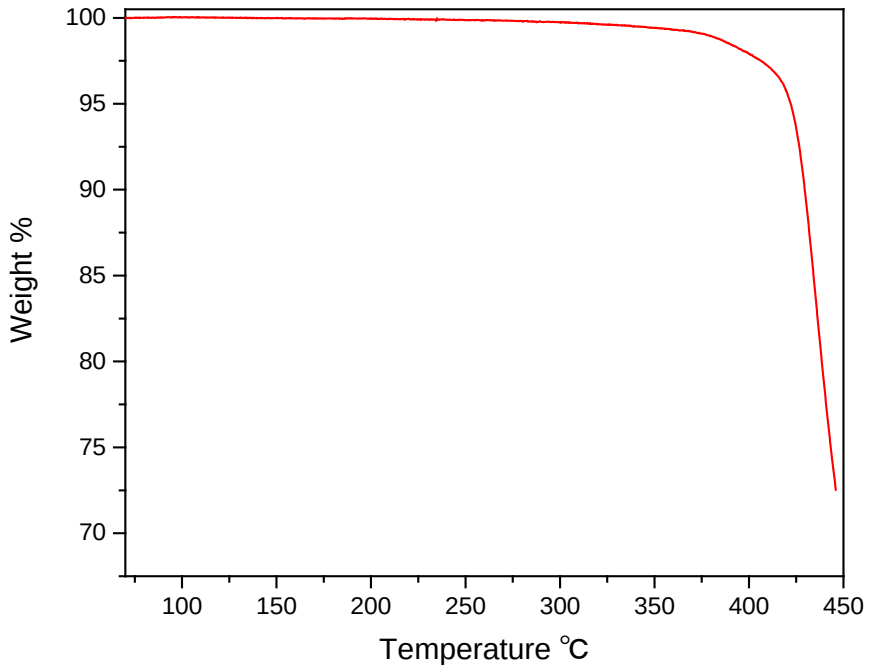

Figure 2-26 The TGA curve of **P3** obtained with temperature increasing rate of 10 °C min^{-1} in nitrogen.

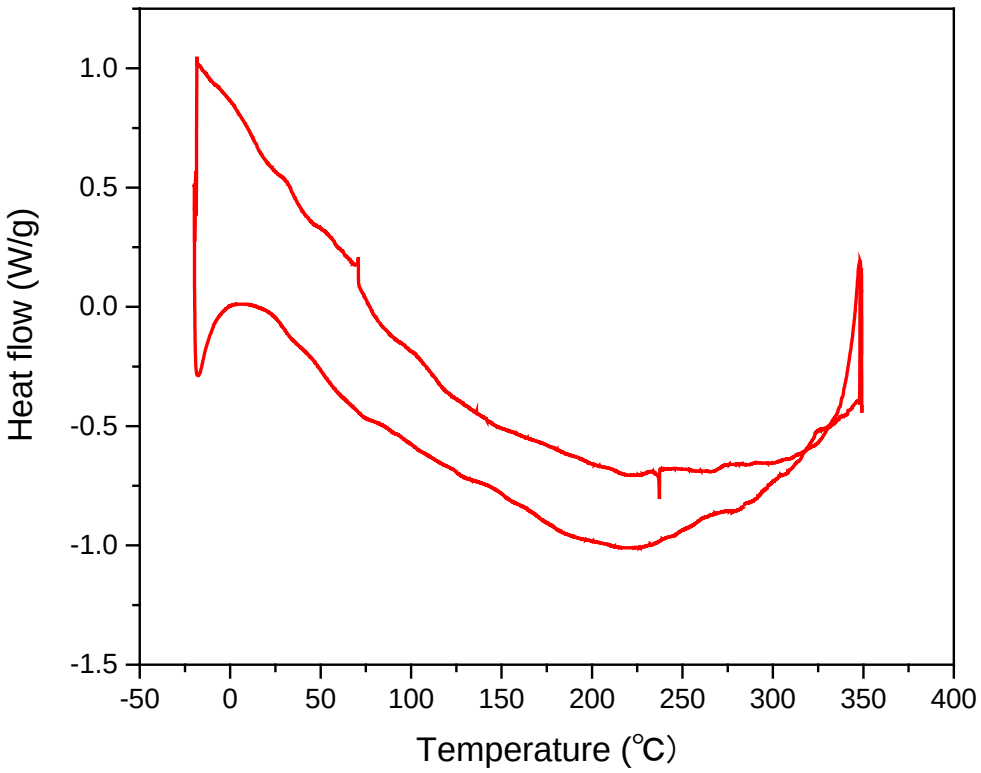

Figure 2-27 DSC profile of **P3** obtained at a scanning rate of 10 °C min^{-1} under nitrogen.

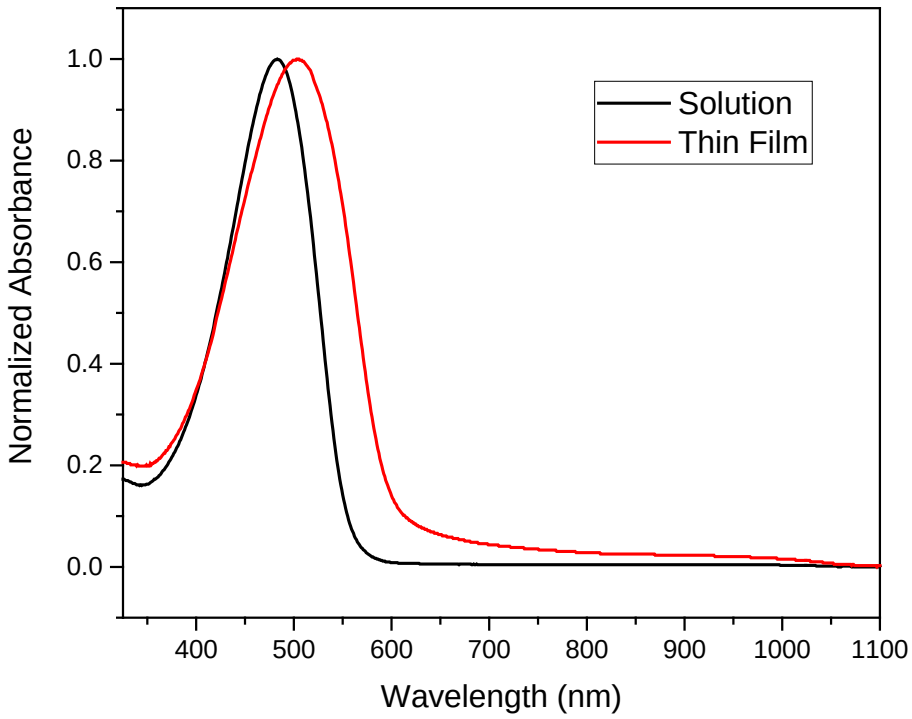

Figure 2-28 Normalized UV-vis absorption spectra of **P3** in solution and in thin film.

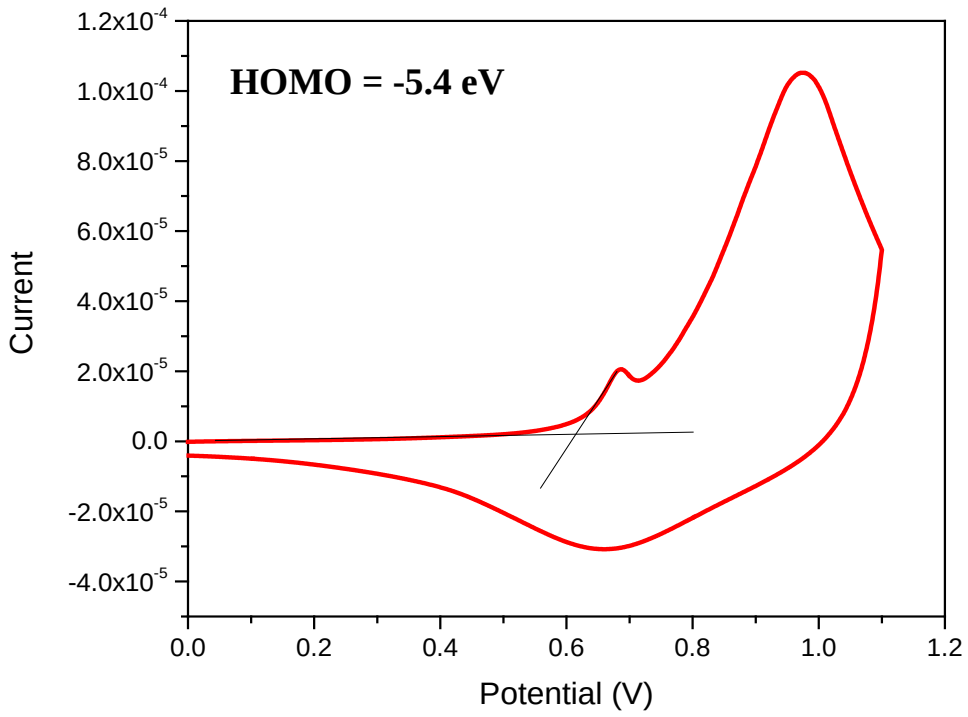

Figure 2-29 The CV diagram of **P3** at a scan rate of 0.1 V/s. The electrolyte was 0.1 M tetrabutylammonium hexafluorophosphate in anhydrous acetonitrile.

The packing of polymer thin films of **P3** was characterized by XRD. From **Figure 2-30**, **P3** showed broad hump at RT and 100 ℃ and intense diffraction peaks at 2θ = 4.62° and 4.47° at 150 ℃ and 200 ℃ annealed samples. These correspond to the interlayer lamellar *d*-spacing of 1.91 nm and 1.98 nm, respectively.

Compared the XRD results with **P2**, **P3** showed a less intense peak and smaller 2θ, indicating less strength of intermolecular reacting and packing. By using the TT building block instead of BT building block successfully decreases the degree of crystallinity as designed.

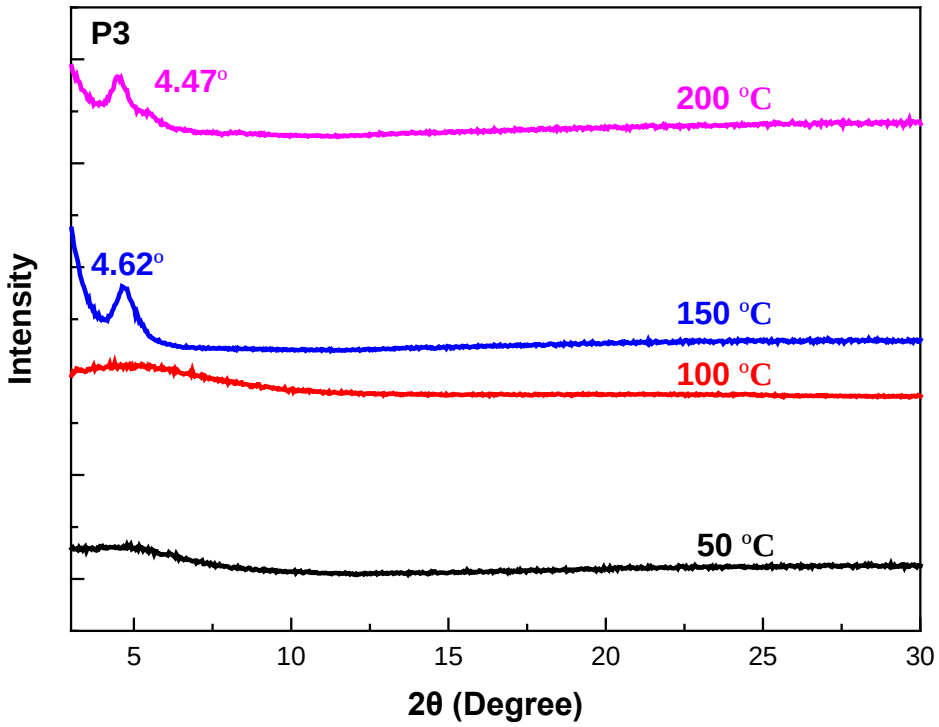

Figure 2-30 The XRD diagram obtained from the spin-coated **P3** thin film on DDTS-modified SiO_2/Si substrates.

2.4.4 OTFT Performances of PBTDCA(BB)-TT

The OTFT performance of **P3** was evaluated as channel semiconductors in BGBC OTFT devices fabricated on DDTS modified SiO_2/Si wafer substrates. The polymers showed p-type charge transport behavior **(Table 2-6** and **Figure 2-31)**. The devices annealed at RT, 100 ℃ and 150 ℃ showed similar hole mobilities, 7.5×10^{-5}, 9.4×10^{-5} and 1.0×10^{-4} $cm^2\ V^{-1}\ s^{-1}$, respectively. After annealing at 200 ℃, the best overall performance with hole mobility of 4.5×10^{-4} $cm^2\ V^{-1}\ s^{-1}$ was obtained. The output curves and transport curves were shown in **Figure 2-31**. These results match the results obtained by XRD, since higher degree of crystallinity gives higher mobility. Broad humps were observed for RT and 100 ℃ annealed films in XRD

results shown in **Figure 2-30.** After thermal treatment, more intense peaks were observed in the XRD spectrum, indicating a long range of ordered packing, thus higher hole mobility.

Table 2-6 Summary of BGBC OTFT performance of **P3**.

Polymer	Annealing[a] temperature (°C)	Hole mobility[b] (10^{-4} $cm^2 V^{-1} s^{-1}$)	Vth[c] (V)	$I_{ON/OFF}$
P3	RT	0.71 ± 0.042 (0.75)	-27	10^3
	100	0.93 ± 0.020 (0.94)	-33	10^3
	150	0.98 ± 0.010 (1.0)	-38	10^3
	200	4.2 ± 0.26 (4.5)	-44	10^3

[a] The devices were annealed in a glove box on a hotplate at the selected temperature for 20 min under argon. Hole mobilities were obtained in the saturated regions in hole enhancement modes. Each set of data were obtained from 3-5 OTFT devices.

[b] The average mobility ± standard deviation (maximum mobility) calculated from the saturation regions of the devices.

[c] The Vth calculated from the device with maximum mobility.

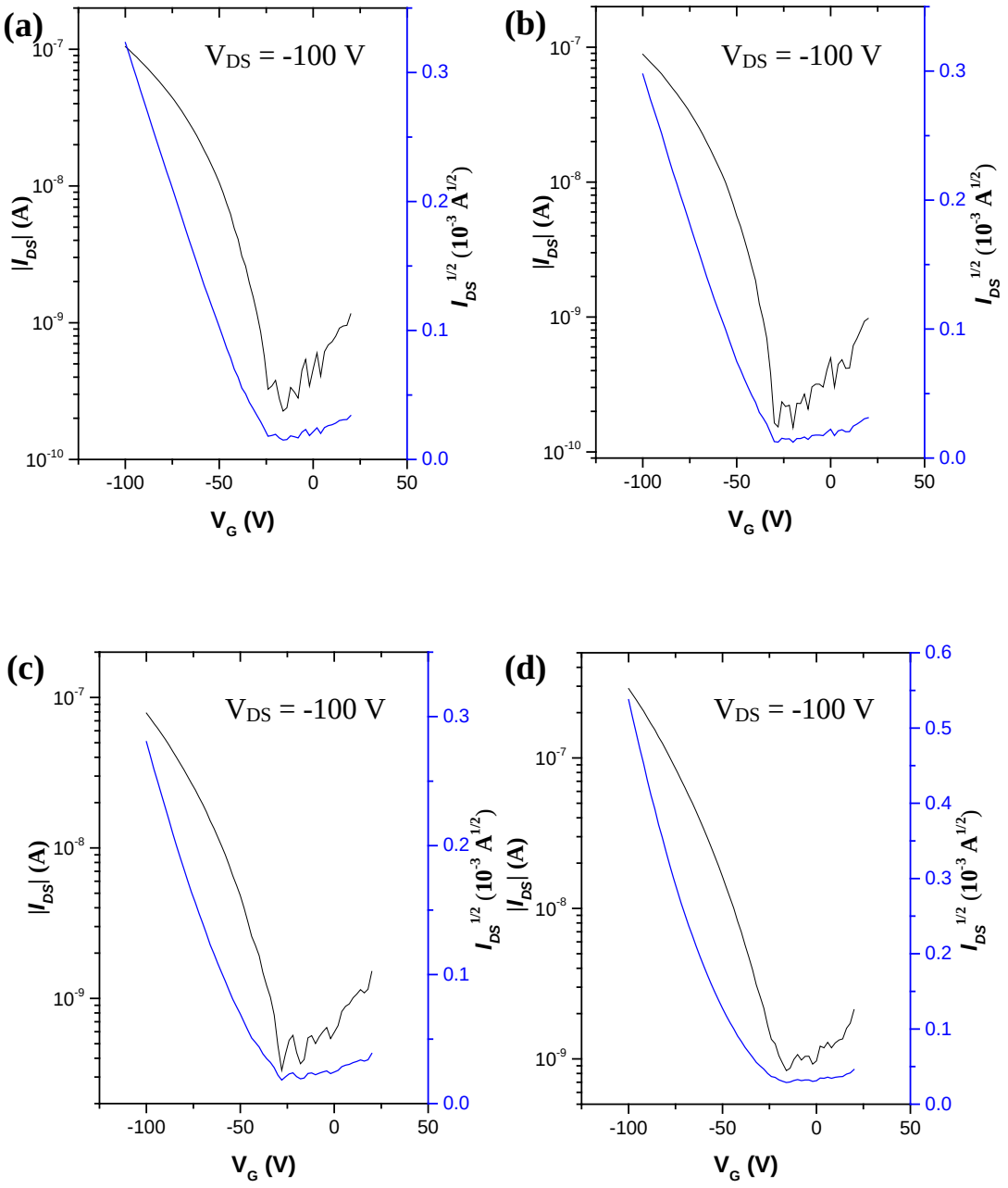
(a)
V_DS = -100 V
|I_DS| (A)
I_DS^1/2 (10^-3 A^1/2)
V_G (V)
(b)
V_DS = -100 V
|I_DS| (A)
I_DS^1/2 (10^-3 A^1/2)
V_G (V)
(c)
V_DS = -100 V
|I_DS| (A)
I_DS^1/2 (10^-3 A^1/2)
V_G (V)
(d)
V_DS = -100 V
|I_DS| (A)
I_DS^1/2 (10^-3 A^1/2)
V_G (V)

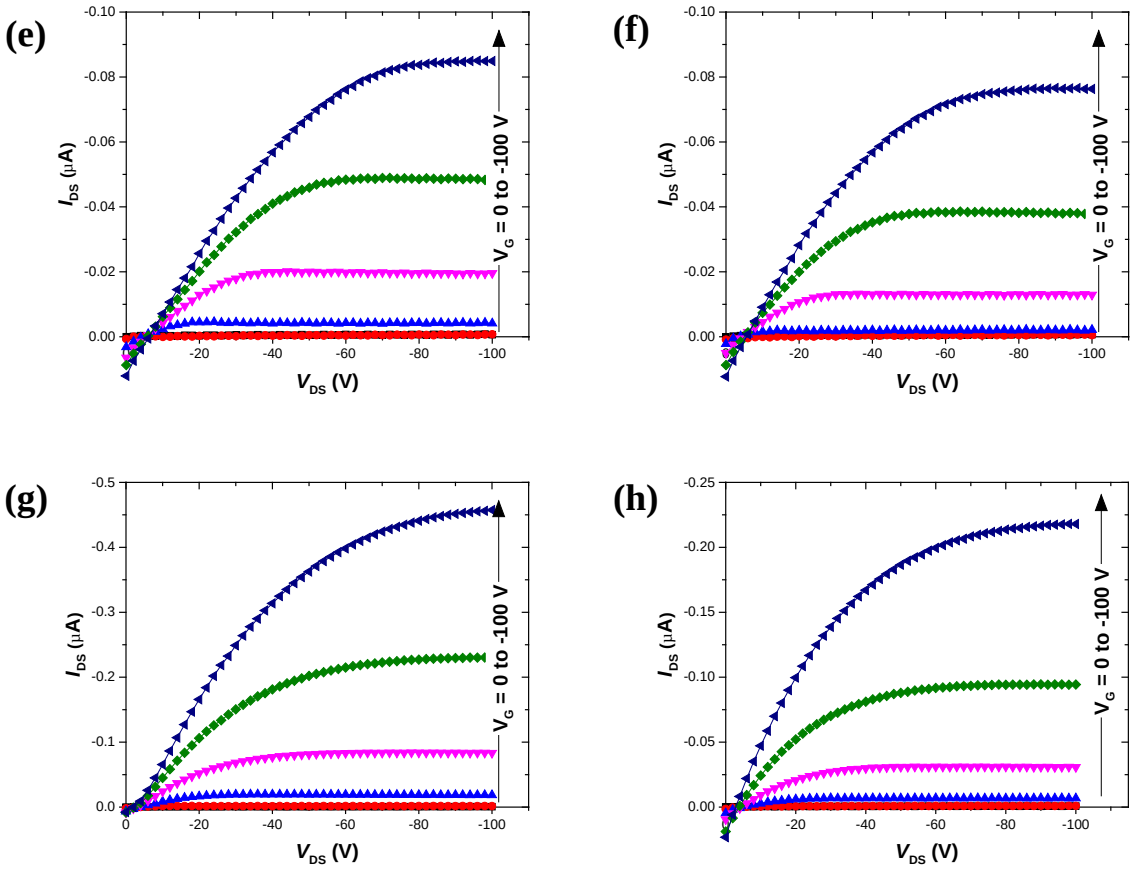

Figure 2-31 The transfer curves (a), (b), (c) and (d) and output curves (e), (f), (g) and (h) for OTFTs based on **P3** annealed at RT, 100 ℃, 150 ℃ and 200 ℃, respectively. Device dimensions: channel length (L) = 30 μm; channel width (W) = 1000 μm. V_G valued from 0 to -100 V in the step of -20 V in output curves.

2.4.5 OPV Performances of P3

Table 2-7 and **Figure 2-32** show the results and J-V curves of solar cells with **P3:** $PC_{61}BM$ as active layer dissolved in different solvent. The Voc is 0.82 V which is similar to **P2:** $PC_{61}BM$ with Voc = 0.87 V, due to their similar HOMO levels. As with the previous results, by replacing BT with TT decreased the degree of crystallinity of **P3**. The grain size decreased

compared with **P2**, as shown in **Figure 2-33**, thus increasing the Jsc and PCE. From **Figure 2-33,** the roughness of active layer in CB is lower (RMS: 3.5 nm) compared with that in DCB (RMS: 3.8 nm), indicating that changing the solvents can influence the film morphology. Thus **P3:** $PC_{61}BM$ in CB exhibits better performance with maximum PCE = 1.59% while PCE = 1.08% when solvent is DCB.

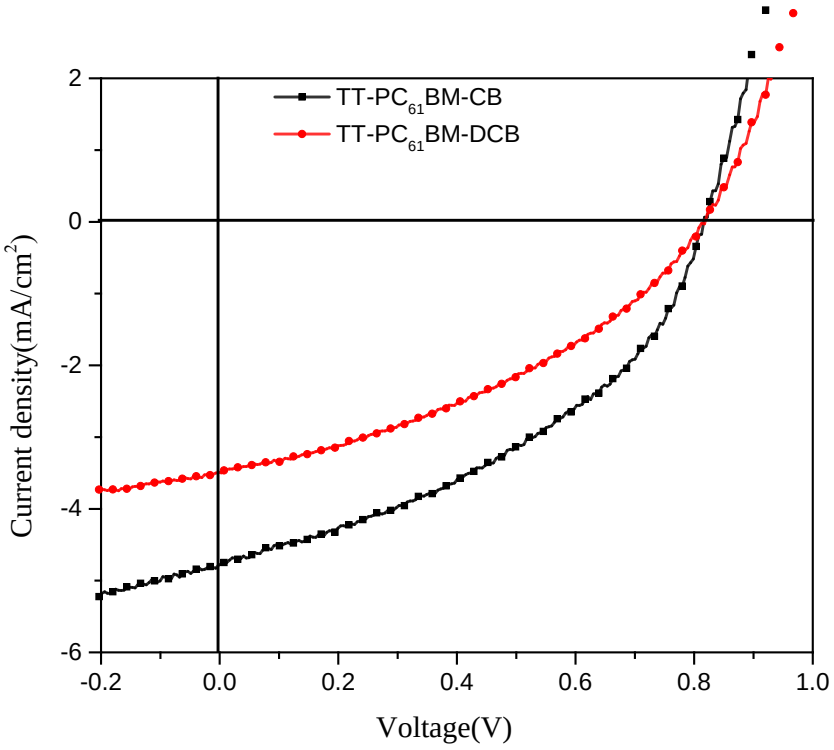

Figure 2-32 J-V curves based on **P3**: $PC_{61}BM$ dissolved in CB under AM 1.5G illumination.

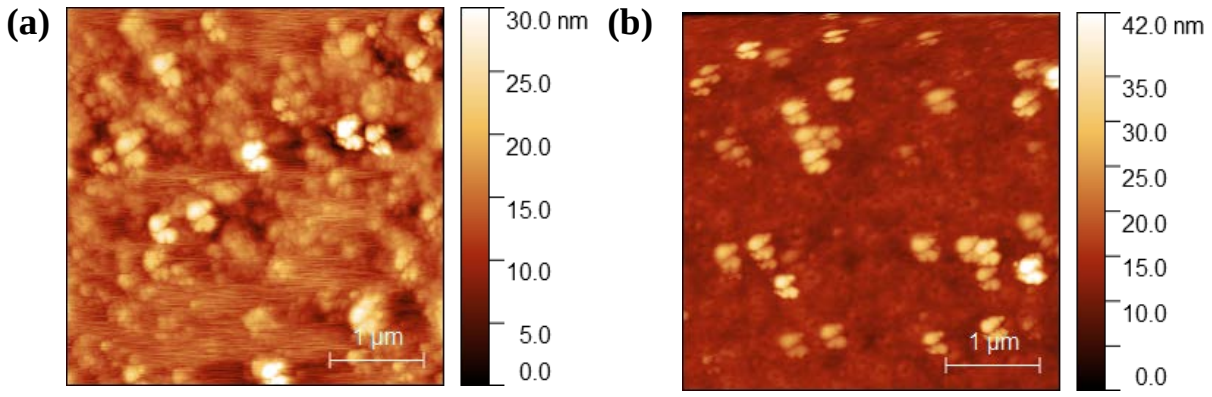

Figure 2-33 AFM images of surface morphology with surface roughness (a) **P3**: $PC_{61}BM$ in CB (RMS: 3.5 nm) (b) **P3**: $PC_{61}BM$ in DCB (RMS: 3.8 nm).

Table 2-7 Summary of the OPV performance of **P3** with $PC_{61}BM$ in CB.

Active layer	**Ratio**	**Solvent**	**Annealing temperature (°C)**	**Jsc (mA/cm^2)**	**Voc (V)**	**FF**	**PCE (%)**	**Rs (ohm/ cm^2)**	**Rsh (ohm/ cm^2)**
P3: $PC_{61}BM$	1: 1	CB	RT	4.8	0.82	0.41	1.59	87	420
P3: $PC_{61}BM$	1: 1	DCB	RT	3.5	0.82	0.38	1.08	363	590

Then the acceptor was changed to ITIC. As observed from AFM image of **P3**: ITIC films shown in **Figure 2-35**, the grain size and RMS are smaller than those in **P2**: ITIC film shown in **Figure 2-22**, revealing lower crystallization degree, which facilitate phase separation and charge separation and transportation**. Table 2-8** and **Figure 2-34** show the effect of different solvents when the acceptor is ITIC. Changing the solvent from CB to DCB, there is an obvious enhancement in Jsc from 7.3 mA/cm^2 to 9.9 mA/cm^2, corresponding with the PCE increase from 2.04% to 3.48%.

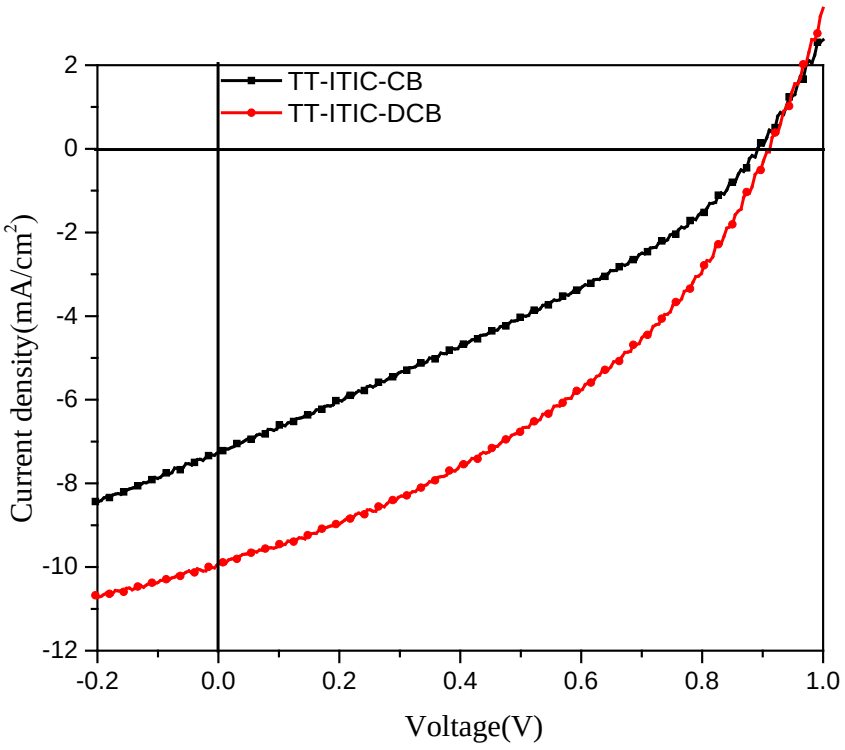

Figure 2-34 J-V curves based on **P3**: ITIC dissolved in CB and DCB under AM 1.5G illumination.

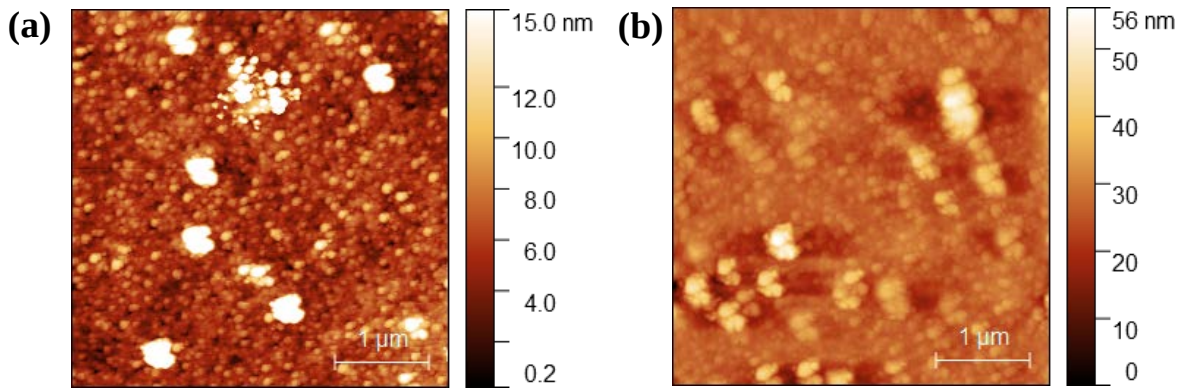

Figure 2-35 AFM images of surface morphology with surface roughness (a) **P3**: ITIC in CB (RMS: 3.6 nm) (b) **P3**: ITIC in DCB (RMS: 4.3 nm).

Table 2-8 Summary of the OPV performance of **P3** with ITIC in CB and DCB.

Active layer	Ratio	Solvent	Annealing temperature (℃)	Jsc (mA/cm^2)	Voc (V)	FF	PCE %	Rs (ohm/ cm^2)	Rsh (ohm/ cm^2)
P3: ITIC	1: 1	CB	RT	7.3	0.89	0.32	2.04	48	166
P3: ITIC	1: 1	DCB	RT	9.9	0.91	0.38	3.48	90	226

Later, 1,8-diiodooctane (DIO) (0.5% volume %) was added into the mixture as additive in order the optimize the phase separation, but we obtained lower PCE (2.04%) which enhance the polymer domain size. By further studying the **Figure 2-36**, it can be observed that there is still some grain scattered in active layer, then lower concentration was used for blend solution to 8 mg/mL (previous concentration: 10 mg/mL) in order to get smaller grain size and more uniform film.

From the results shown in **Table 2-9**, the fill factor improved from 0.39 to 0.43. However, as the concentration decreased, this resulted in a thinner active layer film. The active layer absorbed less light and Jsc dropped, leading to a decrease in PCE (3.29%). For the purpose of more uniform and thicker active layer film, the active layer was spin coated with hot solution on the post-annealing substrate at 100 ℃ with PEDOT: PSS coated. As solvent evaporated more quickly, the film got thicker resulting in an increase on Jsc (from 8.3 mA/cm^2 to 9.3 mA/cm^2), thus a higher PCE of 3.5% was obtained.

In addition, compared with the device based on P3HT: ITIC reported by Qin.[67] with optimized procedure, **P3**: ITIC showed higher values for Jsc, Voc and FF. The PCE of **P3**: ITIC was almost three times the PCE of P3HT: ITIC.

In conclusion, the newly designed **P3** based on P3HT not only successfully increased the Voc but also improved the charge generation, separation and transportation, thus almost triple the PCE than the one obtained by P3HT: ITIC shown in **Table 2-9**.

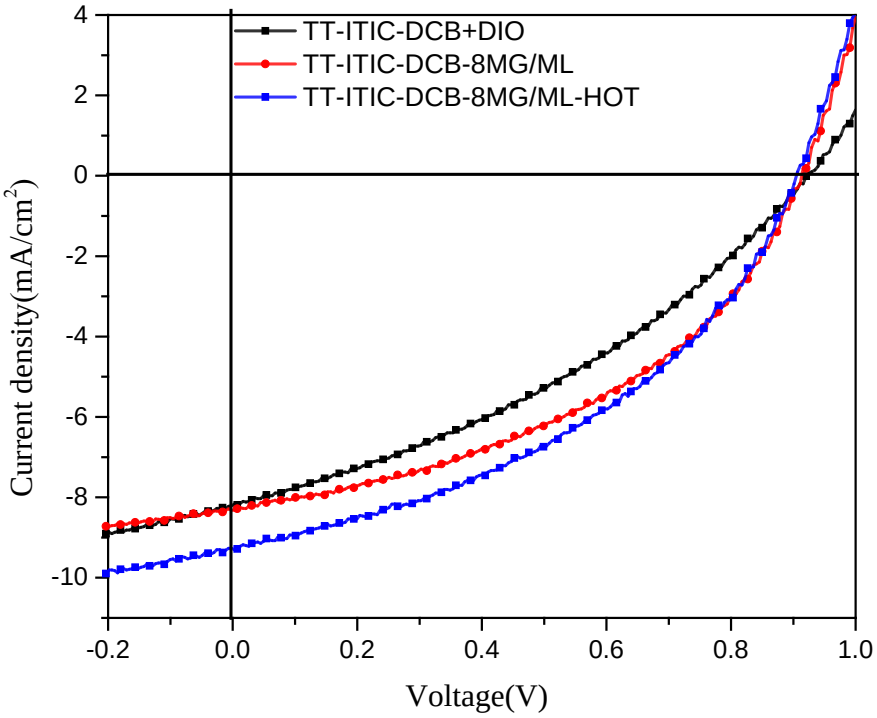

Figure 2-36 J-V curves based on **P3**: ITIC dissolved in DCB with different conditions under AM 1.5G illumination.

Table 2-9 Summary of the OPV performance of **P3** with ITIC in DCB with different conditions.

Active layer	**Ratio**	**Solvent**	**Annealing temperature (°C)**	**Jsc (mA/cm^2)**	**Voc (V)**	**FF**	**PCE (%)**	**Rs (ohm/ cm^2)**	**Rsh (ohm/ cm^2)**
P3: ITIC	1:1	DCB + DIO	RT	8.2	0.92	0.35	2.68	67	253
P3: ITIC	1:1	DCB (8 mg/mL)	RT	8.3	0.91	0.43	3.29	134	392
P3: ITIC	1:1	DCB (8 mg/mL)	Hot substrate	9.3	0.90	0.42	3.50	85	309
P3HT: ITIC[67]	1:1		160 °C	4.2	0.52	0.57	1.25		

2.5 Synthesis and Characterization of PBTDCA(BB)-T

2.5.1 Structure Simulation by Density Functional Theory (DFT)

As evident from section 2.4, we changed the comonomer building block form BT to TT, the crystallinity of the polymer was decreased we desired to be. At the same time, by decreasing the degree of crystallinity, the hole mobility of **P3** with TT also decreased, compared with **P2** with BT as the comonomer building block. The higher solar cell performance for **P3** might be an indication that the hole mobility was already sufficient for the application for OPVs. Beside TT, (T) is also a common building block for polymers, and by introducing T into the polymer can also decrease the crystallinity of the polymer. Furthermore, T shows less electron donating property from TT, which can lower the HOMO level compared with the HOMO level of **P3.** In this chapter, we design another D-A polymer **PBTDCA-T (P4)** shown in **Figure 2-37**, using BTDCA as an acceptor and T as the comonomer building block.

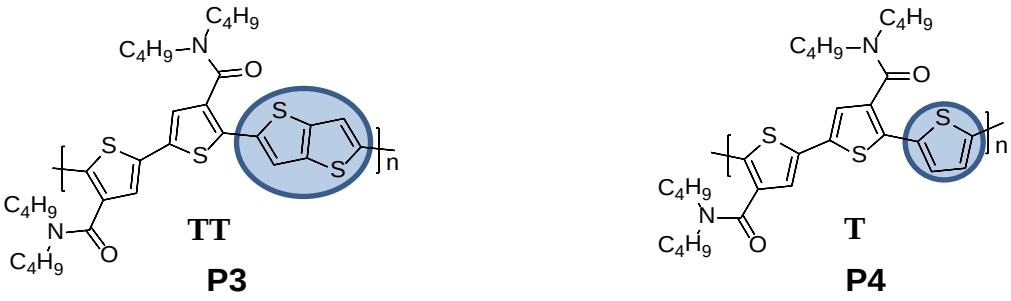

Figure 2-37 Polymer structures for **P3** and **P4**.

The geometry optimization was conducted on each repeating unit of the **PBTDCA-T** by computer simulation based on density functional theory. The carbon chain on the amide was substituted by methyl groups for simplifying the calculation as shown in **Figure 2-38 (a)**. The orbital surfaces of HOMO and LUMO of PBTDCA-Me-T were generated to visualize the electron distribution on the molecular orbitals and the calculated HOMO level and LUMO level with respect to vacuum (0 eV) are shown in **Figure 2-38 (b)** and **(c).** The calculated HOMO level for **P4** was -5.4 eV, which was lower than -5.3 eV for **P3**.

It is clear from **Figure 2-38** that the electrons are evenly distributed over the whole molecule in both HOMO level and LUMO level of the PBTDCA-Me-T. This indicates that the PBTDCA-Me-T has high degree of conjugation.

(a)

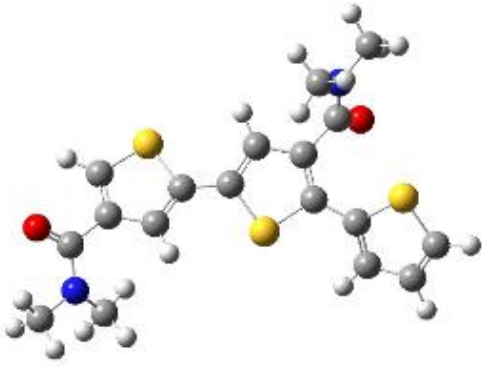

(b)

LUMO = -1.8 eV

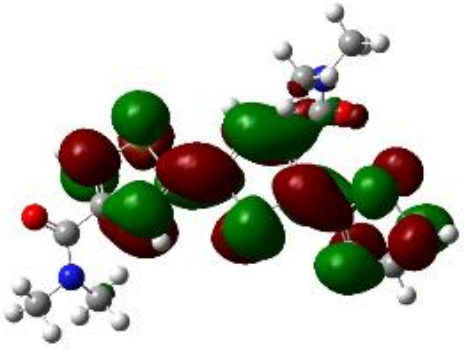

(c)

HOMO = -5.4 eV

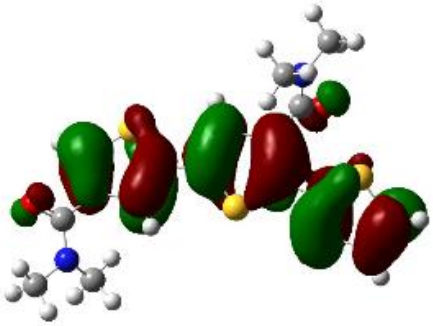

Figure 2-38 (a) Optimized geometry of PBTDCA-Me-T. (b) HOMO and (c) LUMO orbitals of PBTDCA-Me-T and the calculated HOMO/LUMO levels with respect to vacuum (0 eV).

2.5.2 Synthesis of PBTDCA(BB)-T

PBTDCA-T was prepared via Stille coupling of BTDCA with 2,5-2,5-bis(trimethylstannyl)thiophene, and purified using Soxhlet extraction shown in **Scheme 4**. **PBTDCA-T** showed good solubility and can be dissolved in common organic solvents: chloroform, chlorobenzene and 1,2-dichlorobenzene.

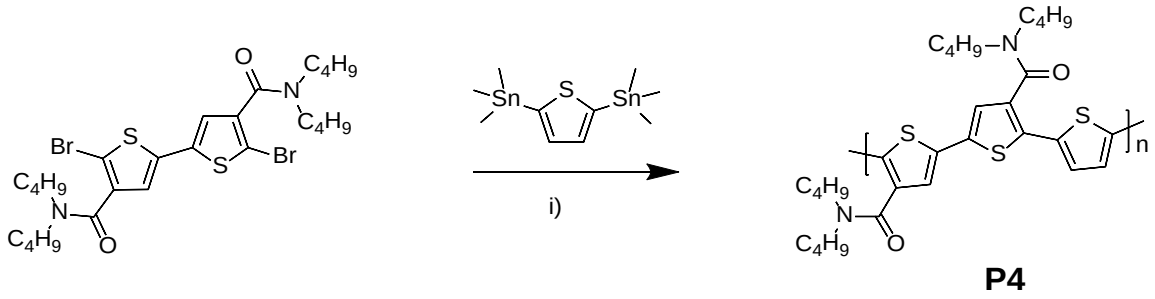

P4

Scheme 4: Synthesis route towards the BTDCA based polymer. Reaction condition: i): Stille coupling 2,5-bis(trimethylstannyl)thiophene/anhydrous chlorobenzene/$Pd(PPh_3)_4$ (5%). Yield: 86% in chloroform for **P4.**

2.5.3 Characterization of PBTDCA(BB)-T by UV-Vis, CV, and XRD

The molecular weight of **P4** was measured by MALDI-TOF-MS, using a Bruker AutoFlex Speed MALDI-TOF mass spectrometer from a matrix of DCTB (2500:1 matrix-to-polymer ratio) casted from chloroform. The Mn and the PDI were determined to be 4.8 kDa and 1.2 **(Figure 2-39).** The UV-Vis absorption spectra of **P4** in solution and in thin film are shown in **Figure 2-40**. **P4** exhibited similar single absorption peak as **P3**. In solution, the λ_{max} was 480 nm. In solid state, **P4** showed the maximum absorption wavelength at 489 nm, only red shifted by 9 nm compared to the λ_{max} in solution, while the absorption wavelength of **P3** red shifted by 21 nm. The larger absorption wavelength red shift means stronger intramolecular and intermolecular D-A interactions in solid state compared with the solution. From this trend, it can be concluded that **P4** showed less conjugation strength between the polymer chains compared with **P3**. The optical bandgap was calculated for the **P4** thin film, using the thin film absorption onsets and found to be ~2.09 eV.

CV was used to reveal the electrochemical properties of the polymers (**Figure 2-41**). The HOMO level calculated from the oxidation onset potentials was -5.3 eV for **P4**. Comparing the HOMO levels of **P3** and **P4** (-5.3 eV vs -5.4 eV), it can be inferred that changing the comonomer building block from TT to T (from **P3** to **P4**) caused a minor change in the HOMO level of only 2%.

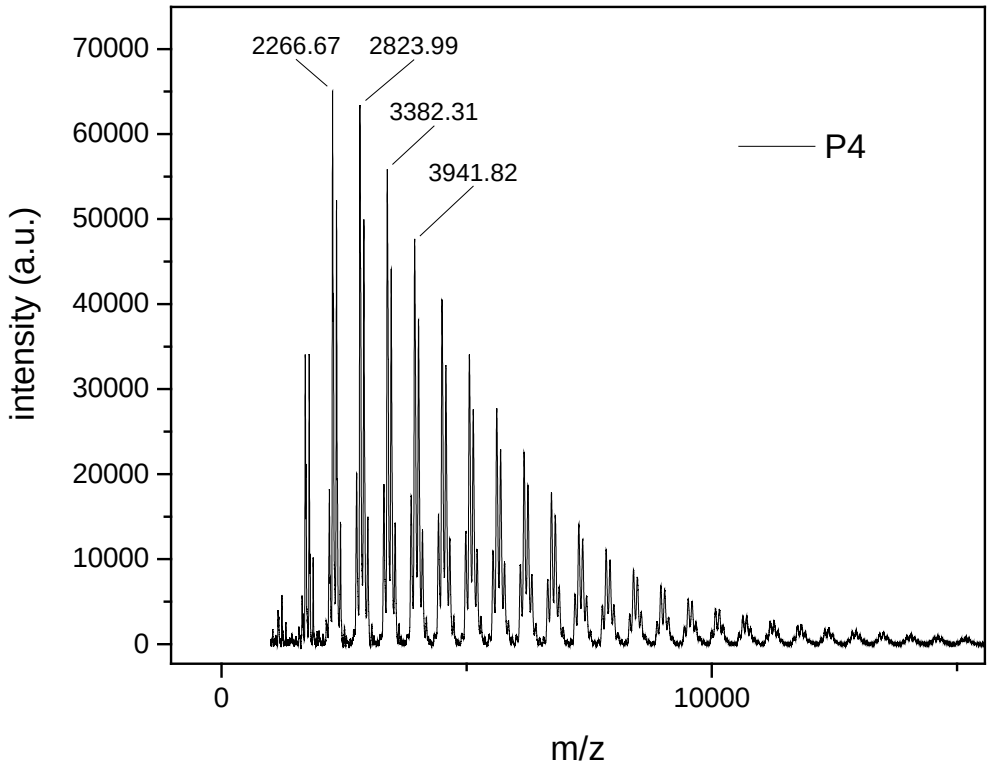

Figure 2-39 The molecular weight distribution of **P4** obtained by MALDI-TOF-MS from a matrix of DCTB (2500:1 matrix-to-polymer ratio) casted from chloroform.

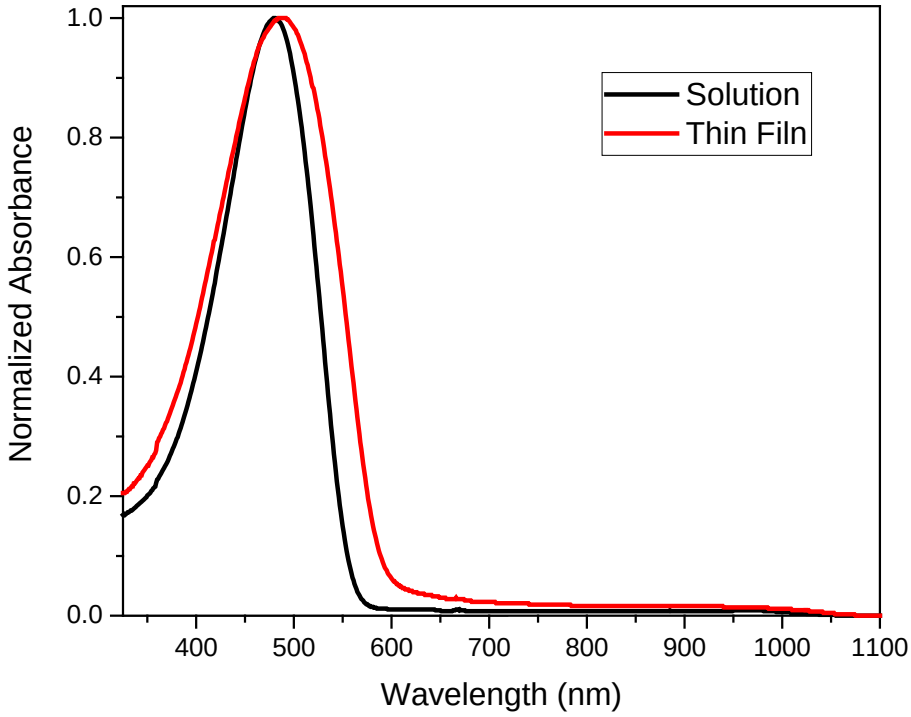

Figure 2-40 Normalized UV-vis absorption spectra of **P4** in the solution and in the thin film.

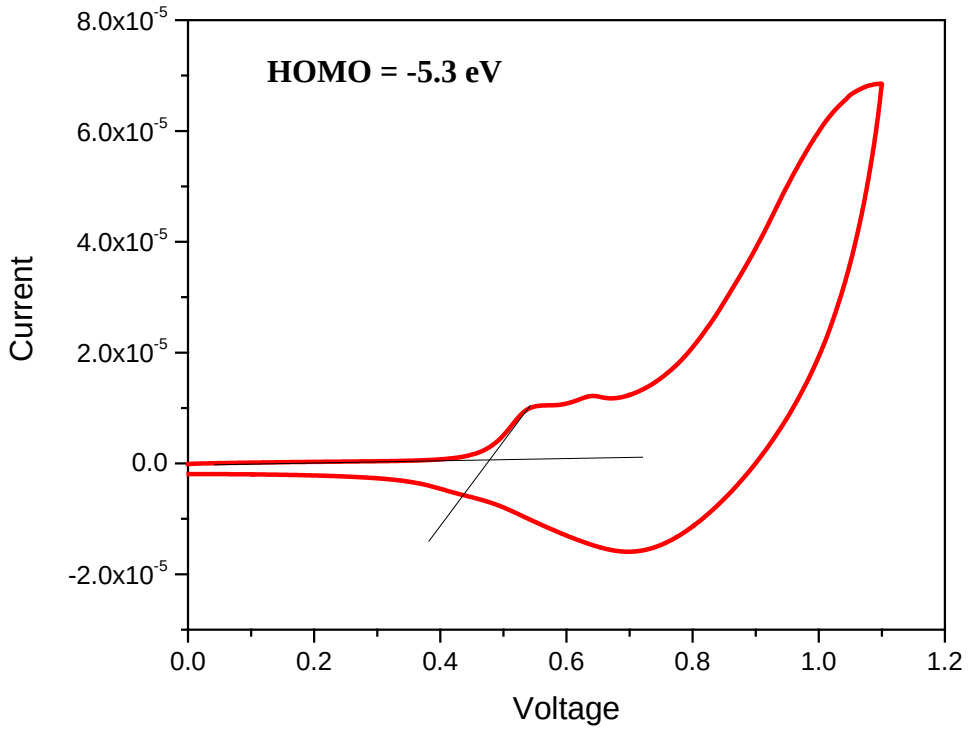

Figure 2-41 The CV diagram of **P4** at a scan rate of 0.1 V/s. The electrolyte was 0.1 M tetrabutylammonium hexafluorophosphate in anhydrous acetonitrile.

The packing of polymer thin films of **P4** was then characterized by XRD. As shown in **Figure 2-42**, no significant peaks were observed for the thin films annealed at RT, 100 ℃ and 150 ℃. **P4** showed almost completely amorphous morphology. Only when the annealing temperature reached 200 ℃, a weak diffraction peak at $2\theta = 5.53°$ with the corresponding interlayer lamellar *d*-spacing of 1.60 nm was observed.

Comparing the XRD results with **P3**, **P4** showed less ordered packing as well as weak interaction between polymer chains in the solid state. Using the T building block instead of BT building block successfully decrease the degree of crystallinity which is the desired material property.

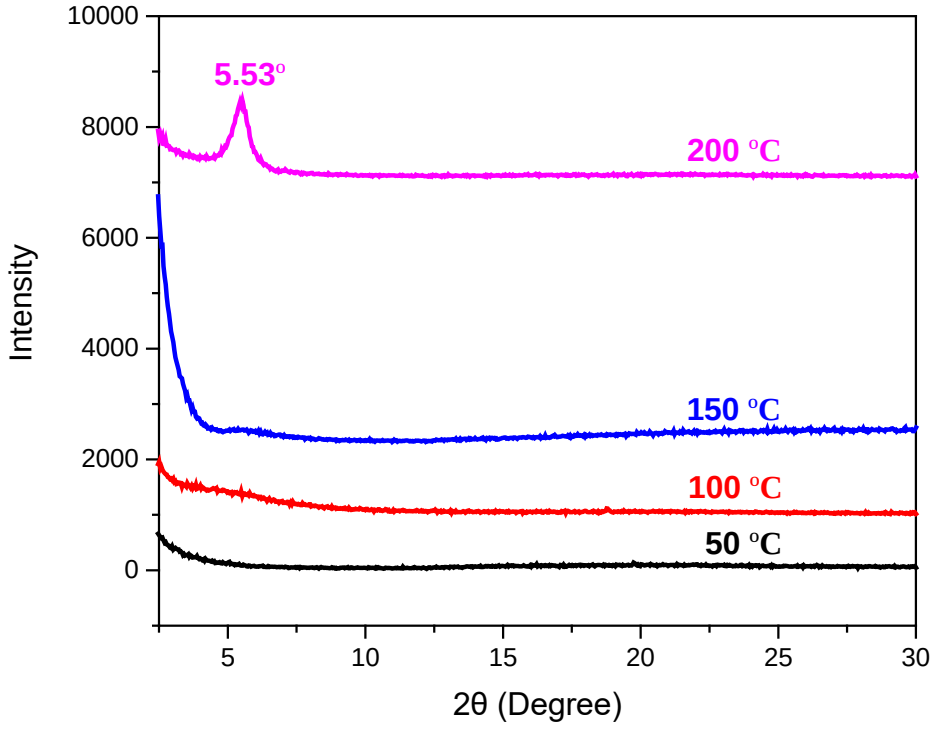

Figure 2-42 The XRD diagram obtained from the spin-coated **P4** thin film on DDTS-modified SiO_2/Si substrates.

2.5.4 OTFT Performances of PBTDCA(BB)-T

In agreement with the XRD results, showing poor crystallinity, **P4** exhibited relatively low hole mobility (shown in **Table 2-10)** compared to **P1**, **P2** and **P3**. The devices based on **P4** did not even turn on until the devices were annealed at 150 ℃ (shown in **Figure 2-43**). The slashes (/) in **Table 2-10** mean the devices were not turned on. The amorphous morphology would create more boundaries between grains which might trap holes and result in large Vth. The hole mobility was slightly increased to 3.0×10^{-5} $cm^2 V^{-1} s^{-1}$ after the devices were annealed at higher temperature (200 ℃).

Table 2-10 Summary of BGBC OTFT performance of **P4**.

Polymer	Annealing[a] temperature (°C)	Hole mobility[b] (10^{-5} cm^2 V^{-1} s^{-1})	Vth[c] (V)	$I_{ON/OFF}$
P4	RT	/	/	/
	100	/	/	/
	150	1.50 ± 0.45 (2.0)	-75	10^3
	200	2.7 ± 0.25 (3.0)	-68	10^2

[a] The devices were annealed in a glove box on a hotplate at the selected temperature for 20 min under argon. Hole mobilities were obtained in the saturated regions in hole enhancement modes. Each set of data were obtained from 3-5 OTFT devices.

[b] The average mobility ± standard deviation (maximum mobility) calculated from the saturation regions of the devices. The slashes (/) mean the devices were not turned on.

[c] The Vth calculated from the device with maximum mobility.

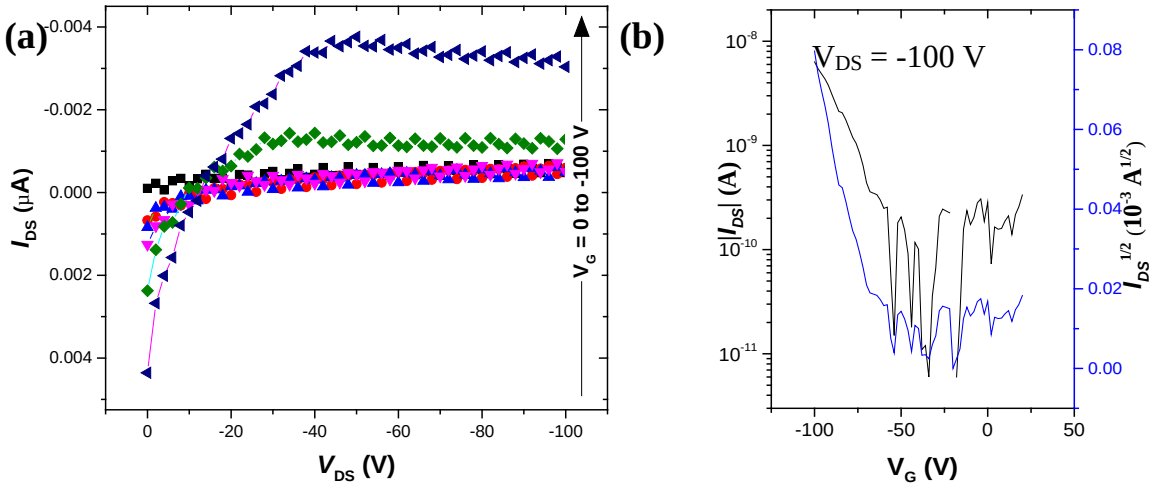

Figure 2-43 The best output curve for OTFTs based on **P4** (a) and transfer curve for OTFTs based on P4 (b). Device dimensions: channel length (L) = 30 μm; channel width (W) = 1000 μm. V_G valued from 0 to -100 V in the step of -20 V in output curves.

2.5.5 OPV Performances of P4

The solar cell results based on **P4** are shown in **Figure 2-44** and **Table 2-11**. The efficiency of the **P4** solar cells decreased at higher temperature (150 ℃, PCE: 0.18%) as compared to the RT unannealed (PCE: 0.43%). This is consistent with the previous results where high temperature has resulted in lower efficiency.

Also, the lower Jsc and low fill factor for these devices means the charge collection efficiency is low. Moreover, the PCE is quite low for this polymer compared to other polymers studied, although the solubility in chloroform (CF) is quite high.

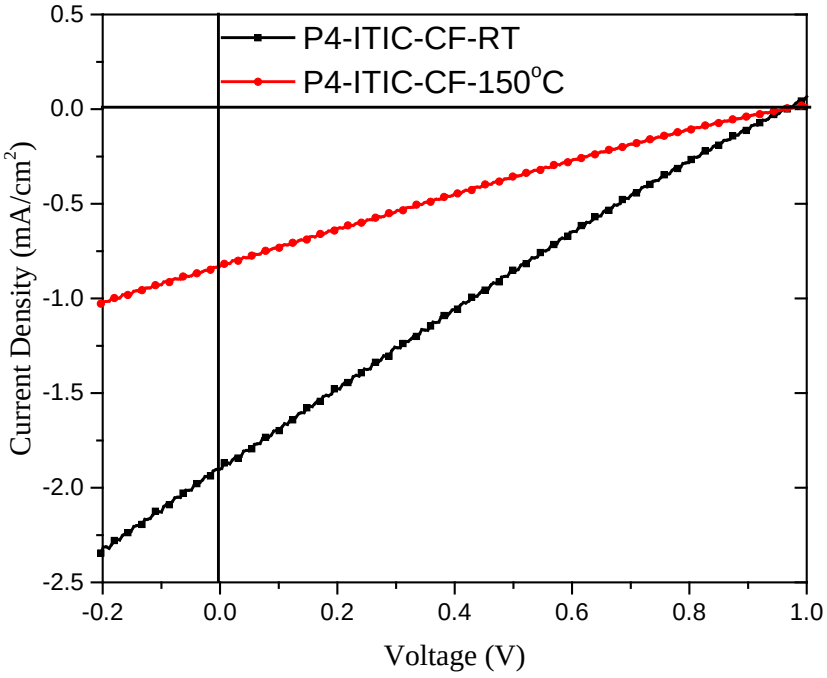

Figure 2-44 J-V curves based on **P4**: ITIC under AM 1.5G illumination.

Table 2-11 Summary of the OPV performance of **P4** with ITIC in CF.

Active layer	Ratio	Solvent	Annealing temperature (℃)	Jsc (mA/cm^2)	Voc (V)	FF	PCE %	Rs (ohm/ cm^2)	Rsh (ohm/ cm^2)
P4: ITIC	1: 1	CF	RT	1.9	0.96	0.24	0.43	609	481
P4: ITIC	1: 1	CF	150 ℃	0.8	0.96	0.23	0.18	1563	1042

2.6 Summary and Future Directions

In this chapter, four polymers based on BTDCA electron-deficient building block were synthesized and characterized. All the polymers in this work have been reported for the first time. Firstly, DFT was conducted to study the molecule geometry, electron distribution, and energy levels of the BTDCA. By comparing the energy levels with BT, the HOMO level was decreased as desired.

As proof of concept, **P1** and **P2** were synthesized with different lengths of side chains, using BT as comonomer unit. Both polymers showed good thermal stability, similar single absorption peak in UV-vis absorption spectra (typical for PT materials) and deeper HOMO level -5.3 eV as compared to P3HT (-4.9 eV). XRD of **P2** showed higher degree of crystallinity and closer interlamellar packing distance than **P1**, due to the shorter side chain, resulting in higher hole mobility (up to 1.4×10^{-2} cm^2 V^{-1} s^{-1}) which is almost ten times that of **P1** (up to 2×10^{-3} cm^2 V^{-1} s^{-1}). From preliminary OPV results, both polymers exhibited higher Voc (up to 0.87 V) than P3HT (0.59 V) using same acceptor $PC_{61}BM$. But the PCE for **P1** and **P2** based solar cells were low, probably due to the high crystallinity of the polymers which can form large grains in the thin film as observed from AFM images, which reduced the charge separation and transportation efficiency.

Based on the previous results, **P3** was synthesized with smaller comonomer unit TT instead of BT in polymer to decrease the crystallinity. The decrease in crystallinity was confirmed via XRD. By decreasing the crystallinity, the hole mobility also decreased to 4.5×10^{-4} cm^2 V^{-1} s^{-1} for **P3**. Interestingly, even with the lower hole mobility, higher PCE was achieved for **P3**: ITIC blend. The PCE was as high as 3.5%, which is four times that of **P2**: ITIC blend (0.85%). This might be due to the optimized thin film morphology. It was noticed that, the solubility of **P3** was not that good after structure optimization.

P4 was synthesized by using T as comonomer unit, which is even smaller than TT to decrease the crystallinity. From the **P4** XRD, only a weak peak was observed after the thin film of **P4** was annealed at 200 ℃. As a result, low hole mobility 3.0×10^{-5} cm^2 V^{-1} s^{-1} for **P4** was obtained. As for the performance of the solar cells, due to its too good solubility and very disordered chain packing, the ideal bi-continuous morphology could not be obtained. This resulted in lower Jsc and low fill factor for **P4** based devices, which means the charge collection efficiency was low.

For the future direction, the BTDCA electron-efficient building block can be polymerized with different comonomer building block[68,69] to broaden the light absorption as well as to balance the crystallinity and solubility to form good morphology of the solar cells active layer. Besides, different ITIC based acceptor materials[70–72] can be used to match with the donor polymers made in this chapter to achieve better solar cells performance. In a nutshell, the preliminary results demonstrated that the BTDCA is a promising electron acceptor building block for constructing, which can bring higher Voc than classic PT materials in OSC applications.

2.7 Experimental Section

2.7.1 Materials and Characterization

MALDI-TOF mass spectra were performed using a Bruker AutoFlex Speed MALDI-TOF mass spectrometer from a matrix of DCTB (2500:1 matrix-to-polymer ratio) casted from chloroform. TGA measurements were carried out on TA Instruments SDT 2960 at a scan rate

of 10 °C min^{-1} under nitrogen. The UV-Vis absorption spectra of polymers were recorded on a Thermo Scientific model GENESYS™ 10S VIS spectrophotometer. CV data were obtained on a CHI600E electrochemical analyser using an Ag/AgCl reference electrode and two Pt disk electrodes as the working and counter electrodes in a 0.1 M tetrabutylammonium 64 hexafluorophosphate solution in acetonitrile at a scan rate of 100 mV s^{-1}. Ferrocene was used as the reference, which has a HOMO level value of -4.8 eV.[73] NMR data was recorded with a Bruker DPX 300 MHz spectrometer with chemical shifts relative to tetramethylsilane (TMS, 0 ppm). XRD measurement are carried out with a Bruker D8 Advance powder diffractometer with Cu Kα radiation (λ = 0.15406 nm) using standard Bragg-Brentano geometry. AFM images were taken on polymer thin films spin-coated on the SiO_2/Si substrates with a Dimension 3100 scanning probe microscope.

2.7.2 Fabrication and Characterization of OTFT Devices

The hole mobility of the polymer was measured by the BGBC configuration for all OTFT devices. The OTFT devices fabrication was carried out as follows:

First, the gold source and drain pairs were patterned on a heavily n-doped SiO_2/Si wafer with 300 nm thickness of SiO_2 by conventional photolithography and thermal deposition. Then, the small square wafers that contain a set of transistors were cut from the large wafer and were placed into an aluminum dish (or glass petri dish, in either case) with acetone and sonicated in an ultra-sonic bath for 20 min at room temperature. Subsequently, acetone was removed and 2-propanol (IPA) was added followed by ultrasonication for an additional 20 min. After sonication, the wafers were dried by using nitrogen gas and treated with oxygen plasma for 2 min with low air flow. Wafers were immersed into pure ethanol, chloroform, 20 mL of a 10 mM solution of octadecanethiol in ethanol for 1 hour and pure ethanol in a covered petri dish successively. After that, wafers were immersed in 100 mL DI Water in covered petri dish, and four drops of 1: 10: 10 (HNO_3: HCl: H_2O) were added. The wafers were kept for one min. Wafers were removed and rinsed with deionized water. Wafers were dried with nitrogen gas and subsequently on hot plate at 120 °C for 10 min. In the next step, wafers were put in a solution of DDTS in toluene (3% DDTS in toluene) at room temperature for 20 min. The

substrates were then rinsed with toluene to remove multilayers of DDTS and dried under a nitrogen flow. Then a polymer solution in dichloromethane (5 mg/mL) was spin-coated onto the substrate at 1000 rpm for 60 s to obtain a polymer film, which was further subjected to thermal annealing at different temperatures for 20 min in an argon filled glove box. All the OTFT devices have a channel length (L) of 30 μm and a channel width (W) of 1000 μm and were characterized in the same glove box using an Agilent B2912A Semiconductor Analyzer. The hole and electron mobilities are calculated in the saturation regime according to the following equation:

$$I_{DS} = \frac{\mu C_i W}{2L}(V_G - V_T)^2$$

where I_{DS} is the drain-source current, μ is charge carrier mobility, C_i is the gate dielectric layer capacitance per unit area (~ 11.6 nF cm^{-2}), V_G is the gate voltage, V_T is the threshold voltage, L is the channel length (30 μm), and W is the channel width (1000 μm).

2.7.3 Fabrication and Characterization of Conventional Type Polymer Solar Cells

All the conventional polymer solar cells were fabricated in the following configuration ITO/PEDOT: PSS/Active layer/LiF/Al shown in **Figure 2-17**. The ITO substrates were placed in ultra-sonic bath immersed in deionized water and acetone for 20 min each at 40 °C. Then the substrates were taken out and placed on aluminum foil. The substrates were cleaned by Q-tips with acetone. Substrates were then sonicated for 20 min at 40 °C in IPA, followed by the cleaning using Q-tips again. The substrates were dried in the vacuum and placed into the air plasma cleaner for 10 min. A ~40 nm thin layer of PEDOT: PSS (Al 4083) was deposited through spin-coating at 4000 rpm and dried subsequently at 150 °C for 20 min in air. Then the substrates were transferred to a nitrogen filled glove box, where the polymer donor and the acceptor blend layer was spin-coated onto the PEDOT: PSS layer via different spin speed. The substrates were then placed onto the hotplate, annealed at different temperatures for 10 min for thermal treatment in nitrogen.

Finally, a thin layer of LiF (1 nm) and a layer of Al (100 nm) electrode were deposited in vacuum onto the substrate at P ≈ 5.0 × 10^{-6} Pa. The active area was 0.0574 cm^2. The current

density–voltage (J-V) characteristics of the polymer solar cells were measured on an Agilent B2912A Semiconductor Analyser with a ScienceTech SLB300-A Solar Simulator. A 450 W xenon lamp and an air mass (AM) 1.5 filter were used as the light source.

2.7.4 Synthesis Procedures

Synthesis of 5-Bromothiophene-3-carboxylic acid (1)

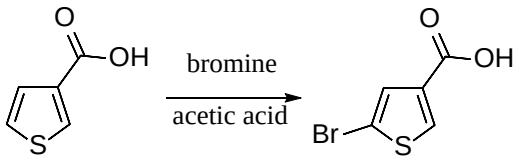

1

To a solution of thiophene-3-carboxylic acid (6.00 g, 46.8 mmol) in 60 mL of acetic acid, bromine (7.47 g, 46.8 mmol) was added dropwise. The mixture was stirred at room temperature overnight, and then water was added. Some white solid was formed, then the precipitate was filtered and recrystallized with hot water: methanol (4:1) to give Compound 1 as white solid. Yield: 4.68 g, (49%).

^{1}H NMR (300 MHz, chloroform-*d*) δ 8.11 (d, *J* = 1.5 Hz, 1H), 7.51 (d, *J* = 1.5 Hz, 1H).

Synthesis of N, N-dihexyl-3-thiophenecarbamide (2)

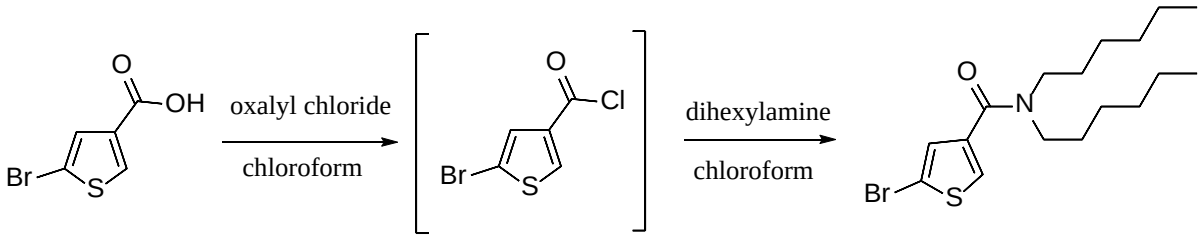

1 **2**

The solution of (1) 5-bromothiophene-3-carboxylic acid (1.86 g, 9 mmol) in 12 mL of anhydrous chloroform was put in a 50 mL heat gun-dried two-neck round bottom flask. The solution was cooled to 0 °C in an ice bath. Oxalyl chloride (2.29 g, 18 mmol) was added dropwise followed with one drop of dimethylformamide (DMF) as a catalyst. The solution was allowed to warm to room temperature for 4h. Unreacted oxalyl chloride was removed under

reduced pressure. The intermediate product was used immediately for the next step, due to its very poor stability in air.

To a 50 mL heat gun-dried two-neck round bottom flask, dihexylamine (3.34 g, 15 mmol) in 10 mL of anhydrous chloroform was added. The solution was cooled to 0 °C in an ice bath. Crude 5-bromothiophene-3-carbonyl chloride was dissolved in 5 mL of anhydrous chloroform and added dropwise carefully. Then the solution was allowed to warm to room temperature and stirred overnight. The reaction was quenched by addition of water. The organic phase was further washed with brine twice and dried over anhydrous Na_2SO_4. Upon removal of solvent in vacuo, the crude product was further purified by silica gel column chromatography with hexane: ethyl acetate (5:1) to give Compound 2. Yield: 3.23 g, (96%).

^{1}H NMR (300 MHz, chloroform-*d*) δ 7.32 (s, 1H), 7.10 (s, 1H), 3.34 (d, *J* = 31.0 Hz, 4H), 1.42 (dd, *J* = 99.2, 21.6 Hz, 18H), 0.89 (d, *J* = 5.8 Hz, 6H).

Synthesis N^4, N^4, $N^{4'}$, $N^{4'}$-tetrahexyl-[2,2'-bithiophene]-4,4'-dicarboxamide (3)

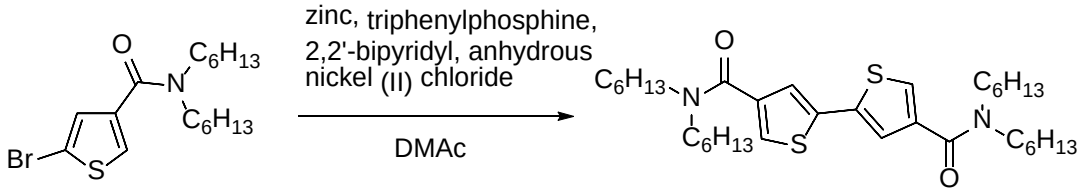

2 **3**

To a 50 mL round bottom flask, N, N-dihexyl-3-thiophenecarbamide (2.6 g, 7 mmol), zinc powder (1.83 g, 28 mmol), triphenylphosphine (0.92 g, 3.5 mmol), 2,2’-bipyridyl (0.077 g, 0.49 mmol), anhydrous nickel (II) chloride (0.063 g, 0.49 mmol) were added. The mixture was vacuumed and filled with argon three times and then dimethylacetamide (DMAc) (20 mL) was added. The mixture was heated to 80 °C and maintained overnight (the thin layer chromatography (TLC) showing no starting material). The reaction mixture was cooled down to room temperature and poured into a cold HCl. After extraction with ethyl acetate, the organic phase was dried with anhydrous Na_2SO_4. The solvent was removed under reduced pressure. Purification via silica gel column chromatography with hexane: ethyl acetate (3:1) to give Compound 3. Yield: 1.20 g, (57%).

^{1}H NMR (300 MHz, chloroform-*d*) δ 7.31 (s, 2H), 7.22 (s, 2H), 3.38 (d, *J* = 27.5 Hz, 8H), 1.54 (m, 8H), 1.32 (m, 24H), 0.88 (s, 12H).

Synthesis of 5,5'-Dibromo-N^4, N^4, N$^{4'}$, N$^{4'}$-tetrahexyl-[2,2'-bithiophene]-4,4'-dicarboxamide (4)

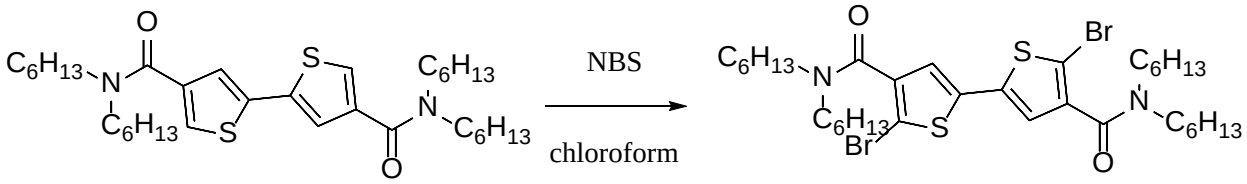

3 **4**

To a 25 mL two-neck round bottom flask, N^4, N^4, N$^{4'}$, N$^{4'}$-tetrahexyl-[2,2'-bithiophene]-4,4'-dicarboxamide (3) (0.59 g, 1 mmol) and N-bromosuccinimide (NBS) (0.375 g, 2.1 mmol) were added. The mixture was degassed and filled with argon three times and then mixture of chloroform (5 mL) and trifluoracetic acid (1 mL) were added. The mixture was stirred in the dark covered with aluminum foil for 2 h (TLC showing no starting materials). The mixture was extracted with chloroform several times and the organic phases were combined washed by sodium sulfite aqueous solution. The organic phase was concentrated through reduced pressure and dried with anhydrous Na_2SO_4. Purification via silica gel column chromatography, flushed by ethyl acetate/hexane (1:4) to give Compound 4. Yield: 0.75 g, (95%).

^{1}H NMR (300 MHz, chloroform-*d*) δ 6.89 (s, 2H), 3.47 (t, *J* = 7.6 Hz, 4H), 3.22 (t, *J* = 7.5 Hz, 4H), 1.65 – 1.49 (m, 8H), 1.34 – 1.15 (m, 24H), 0.87 (d, *J* = 21.4 Hz, 12H). ^{13}C NMR (75 MHz, chloroform-*d*) δ 164.61, 139.04, 137.02, 123.63, 109.49, 48.45, 44.65, 31.56, 31.18, 28.56, 27.35, 26.66, 26.16, 22.58, 22.41, 14.02, 13.94.

Synthesis of 5-Bromo-N, N-dibutylthiophene-3-carboxamide (5)

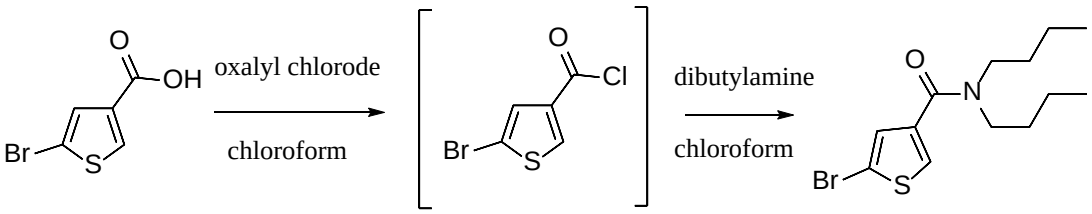

1 **5**

To a solution of (1) 5-bromothiophene-3-carboxylic acid (1.64 g, 7.9 mmol) in 12 mL of anhydrous chloroform was put in a 50 mL heat gun-dried two-neck round bottom flask. The solution was cooled to 0 °C in an ice bath. Oxalyl chloride (2 g, 15.8 mmol) was added dropwise followed with one drop of DMF as a catalyst. The solution was allowed to warm to room temperature for 4 h. Unreacted oxalyl chloride was removed under reduced pressure. The intermediate product was used immediately for the next step, due to its very poor stability in air.

To a 50 mL heat gun-dried two-neck round bottom flask, dibutylamine (2.05 g, 15.8 mmol) in 10 mL of anhydrous chloroform was added. The solution was cooled to 0 °C in an ice bath. Crude 5-bromothiophene-3-carbonyl chloride was dissolved in 5 mL of anhydrous chloroform and added dropwise carefully. Then the solution was allowed to warm to room temperature and stirred overnight. The reaction was quenched by addition of water. The organic phase was further washed with brine twice and dried over anhydrous Na_2SO_4. Upon removal of solvent in vacuum, the crude product was further purified by silica gel column chromatography with hexane: ethyl acetate (5:1) to give Compound 5. Yield: 2.33 g, (95%).

^{1}H NMR (300 MHz, chloroform-*d*) δ 7.31 (s, 1H), 7.10 (s, 1H), 3.34 (d, *J* = 26.8 Hz, 4H), 1.64 – 1.13 (m, 8H), 0.90 (m, 6H).

Synthesis N^4, N^4, $N^{4'}$, $N^{4'}$-tetrabutyl-[2,2'-bithiophene]-4,4'-dicarboxamide (6)

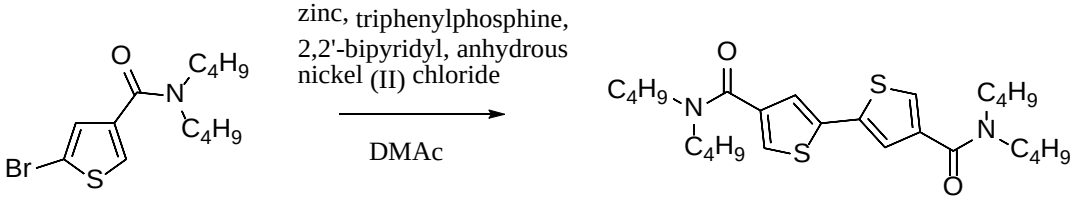

5 **6**

To a 50 mL round bottom flask, 5-bromo-N, N-dibutylthiophene-3-carboxamide (2.23 g, 7 mmol), zinc powder (1.83 g, 28 mmol), triphenylphosphine (0.92 g, 3.5 mmol), 2,2'-bipyridyl (0.077 g, 0.49 mmol), anhydrous nickel (II) chloride (0.063 g, 0.49 mmol) were added. The mixture was degassed and filled with argon three times and then DMAc (15 mL) was added. The mixture was heated to 80 ℃ and maintained overnight (the TLC showing no starting material). The reaction mixture was cooled down to room temperature and poured into cold HCl. After extraction with ethyl acetate, the organic phase was dried with anhydrous Na_2SO_4. The solvent was removed under reduced pressure. Purification via silica gel column chromatography with hexane: ethyl acetate (3:1) to give Compound 6. Yield: 1.05 g, (63%). ^{1}H NMR (300 MHz, chloroform-*d*) δ 7.31 (d, *J* = 1.3 Hz, 2H), 7.22 (d, *J* = 1.3 Hz, 2H), 3.39 (d, *J* = 28.5 Hz, 8H), 1.62 (s, 24H), 0.92 (d, *J* = 21.4 Hz, 12H). ^{13}C NMR (75 MHz, chloroform-*d*) δ 164.67, 139.04, 137.05, 123.64, 109.52, 48.21, 44.42, 30.77, 29.51, 20.25, 19.71, 13.88, 13.57.

Synthesis 5,5'-Dibromo-N^4, N^4, $N^{4'}$, $N^{4'}$-tetrabutyl-[2,2'-bithiophene]-4,4'-dicarboxamide (7)

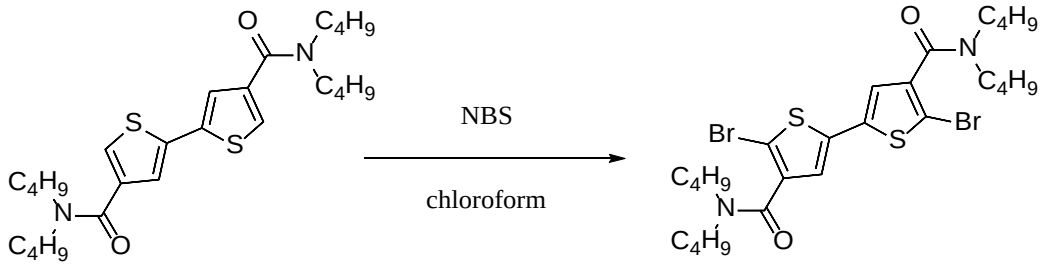

6 **7**

To a 25 mL two-neck round bottom flask, N^4, N^4, $N^{4'}$, $N^{4'}$-tetrahexyl-[2,2'-bithiophene]-4,4'-dicarboxamide (6) (0.7378 g, 1.5 mmol) and NBS (0.5784 g, 3.15 mmol) were added. The mixture was degassed and filled with argon three times and then mixture of chloroform (7.5 mL) and trifluoracetic acid (1.5 mL) were added. The mixture was stirred in the dark covered with aluminum foil for 5 h (TLC showing no starting materials). The mixture was extracted with chloroform several times and the organic phases were combined washed by sodium sulfite aqueous solution. The organic phase was concentrated through reduced pressure and dried with anhydrous Na_2SO_4. Purification via silica gel column chromatography, flushed by ethyl acetate/hexane (1:3) to give Compound 7. Yield: 0.90 g, (94%).

^{1}H NMR (300 MHz, chloroform-*d*) δ 6.89 (s, 2H), 3.54 – 3.42 (t, *J* = 7.5 Hz, 4H), 3.22 (t, *J* = 7.5 Hz, 4H), 1.72 – 1.33 (m, 16H), 0.97 (t, *J* = 7.3 Hz, 6H), 0.82 (t, *J* = 7.3 Hz, 6H).

Synthesis of P1

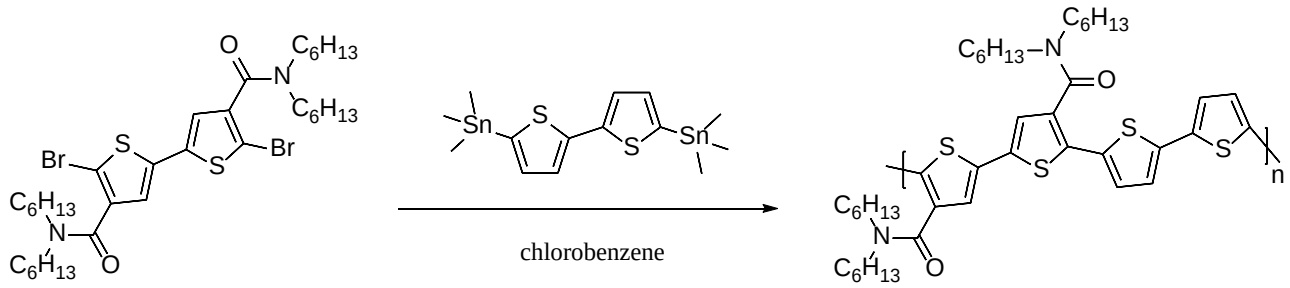

P1

To a 25 mL double-neck round-bottom flask, 5,5'-dibromo-N4, N4, N4', N4'-tetrahexyl-[2,2'-bithiophene]-4,4'-dicarboxamide (152.8 mg, 0.205 mmol) and 5, 5'-bis(trimethylstannyl)-2,2'-bithiophene (100.2 mg, 0.205 mmol) were added. After degassing and refilling argon three times, toluene (4 mL) was added to dissolve the mixture, followed by addition of $Pd(PPh_3)_4$. The mixture was heated to reflux for 24 h. The reaction mixture was cooled down to room temperature and poured into MeOH (150 mL). The precipitate was collected by filtration and subjected to Soxhlet extraction with acetone and hexane successively. The residual was dissolved in chloroform. The polymer was recovered as solid from the chloroform fraction by precipitation from methanol. The solid was dried under vacuum. Yield: 0.128g, (80%) in chloroform fraction.

Synthesis of P2

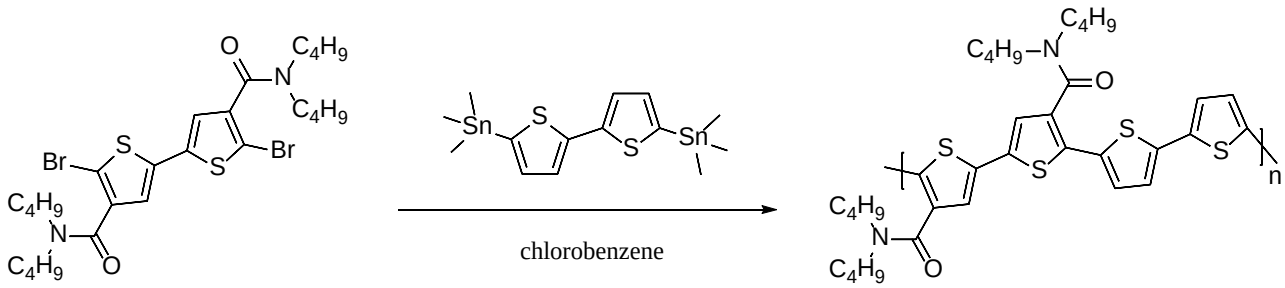

P2

To a 25 mL double-neck round-bottom flask, 5,5'-dibromo-N4, N4, N4', N4'-tetrabutyl-[2,2'-bithiophene]-4,4'-dicarboxamide (190 mg, 0.3 mmol) and 5, 5'-bis(trimethylstannyl)-2,2'-bithiophene (147.6 mg, 0.3 mmol) were added. After degassing and refilling argon three times, toluene (5 mL) was added to dissolve the mixture, followed by addition of $Pd(PPh_3)_4$. The mixture was heated to reflux for 24 h. The reaction mixture was cooled down to room temperature and poured into MeOH (150 mL). The precipitate was collected by filtration and subjected to Soxhlet extraction with acetone and hexane successively. The residual was dissolved in chloroform. The polymer was recovered as solid from the chloroform fraction by precipitation from methanol. The solid was dried under vacuum. Yield: 0.155g, (78%) in chlorobenzene fraction.

Synthesis of P3

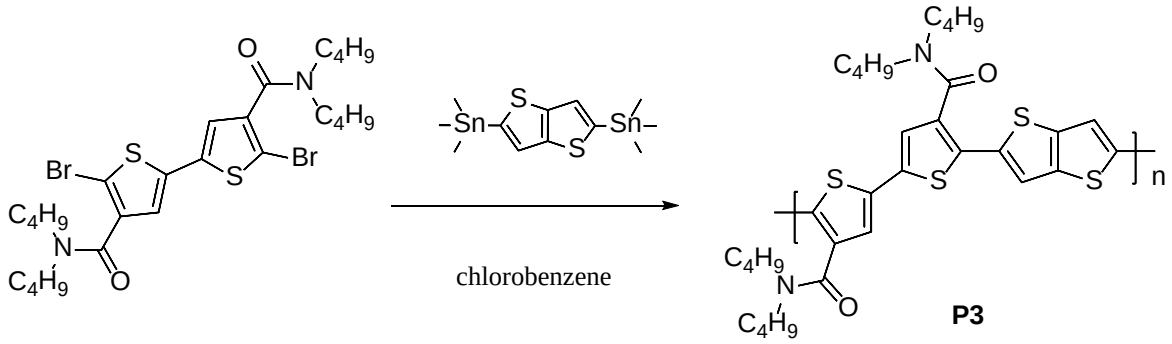

P3

To a 25 mL double-neck round-bottom flask, 5,5'-dibromo-N^4, N^4, $N^{4'}$, $N^{4'}$-tetrabutyl-[2,2'-bithiophene]-4,4'-dicarboxamide (158.6 mg, 0.25 mmol) and 2,5-bis(trimethylstannyl)-thieno[3,2-b]thiophene (116.5 mg, 0.25 mmol) were added. After degassing and refilling argon

three times, chlorobenzene (4 mL) was added to dissolve the mixture, followed by addition of $Pd(PPh_3)_4$. The mixture was heated to 120 ℃ for 40 h. The reaction mixture was cooled down to room temperature and poured into MeOH (100 mL). The precipitate was collected by filtration and subjected to Soxhlet extraction with acetone and hexane and chloroform successively. The residual was dissolved in chlorobenzene. The polymer was recovered as solid from the chlorobenzene fraction by precipitation from methanol. The solid was dried under vacuum. Yield = 0.109g, (78%) in chlorobenzene fraction.

Synthesis of P4

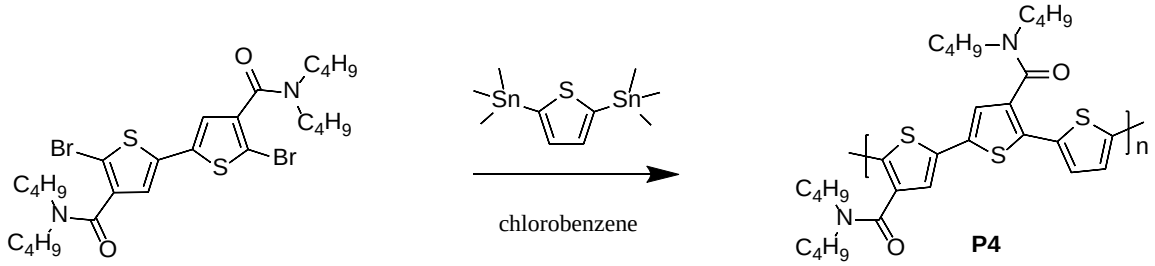

To a 25 mL double-neck round-bottom flask 5,5'-dibromo-N^4, N^4, $N^{4'}$, $N^{4'}$-tetrabutyl-[2,2'-bithiophene]-4,4'-dicarboxamide (126.9 mg, 0.2 mmol) and 2,5-bis(trimethylstannyl)thiophene (82 mg, 0.2 mmol). After degassing and refilling argon three times, chlorobenzene (4 mL) was added to dissolve the mixture, followed by addition of $Pd(PPh_3)_4$ (11.6 mg, 0.01 mmol). The mixture was heated to 120 ℃ for 40 h. The reaction mixture was cooled down to room temperature and poured into hexane (100 mL). The solid was collected and subjected to Soxhlet extraction with hexane and chloroform. The polymer was recovered as solid from the chloroform fraction by precipitation from hexane. The solid was dried under vacuum. Yield: 0.120g, (86%) in chloroform fraction.

Chapter 3 Synthesis and Characterization of BTDCA(H)-based Polymers with Hydrogen Bonding

3.1 Polymer with Hydrogen Bonding

Bulk heterojunction (BHJ) solar cells have aroused great interest in the research field for their potential application as highly efficient and low-cost solar cells, to deal with energy conservation. The morphology of the active layer in the BHJ solar cells is the key factor for the total performance of the devices. It is suggested that achieving a bi-continuous nanoscale of the donor and acceptor domain size would prompt a more efficient charge separation and transport. Much of the efforts such as further thermal treatment like thermal annealing or solvent annealing and the use of solvent additives have been made to optimize the morphology of the active layer.[17,19,74–79] Beside the processing treatments, we also can achieve the desired morphology by applying self-assembly or self-organization during molecular design.[80–85]

To construct the self-assembling architectures, hydrogen bonding is an ideal choice since it is highly selective, directional and creates strong interaction between molecules.[86–89] Many delicate examples are present in nature of the existence of hydrogen bonding like in DNA and proteins. In the hydrogen bond, a hydrogen atom can be shared between an H-bond donor and an H-bond acceptor carrying electron lone pairs.

Hydrogen bonded organic dyes have been used into semiconductors in many applications. Dhar[90] applied N-H bonded into diketopyrrolopyrrole (DPP) based π-conjugated systems in OTFT, which significantly increased the charge transport mobility. Yanagisawa[91] and Głowacki[92] also used free NH groups in DPP forming hydro bonding for OTFT. Besides, several researchers demonstrated the employment of hydrogen bonding in BHJ solar cells improve the overall device performance.[93–97]

Table 3-1 Strength of several noncovalent forces.[98]

Type of interaction or bonding	Strength (kJ mol^{-1})
covalent bond	100-400
Coulomb	250
hydrogen bond	10-65
ion-dipole	50-200
dipole-dipole	5-50
cation-π	5-80
π-π	0-50
van der Waals forces	<5

From **Table 3-1**, the hydrogen bond typically shows the force strength range 10-65 kJ mol^{-1} which is much smaller than the covalent bond which has a homolytic bond dissociation energy that ranges between 100 and 400 kJ mol^{-1}. However, hydrogen bonding can play an important role in determining the molecular packing in the solid state which is crucial for the formation of donor-acceptor domains and light absorption.[98]

Compared to van der Waals force (less than 5 kJ mol^{-1}) and π-π interaction forces (0-50 kJ mol^{-1}),[99–102] which are inevitably present in the donor and acceptor domains, hydrogen bonding can be selectively incorporated and designed.

In this chapter, we introduce hydrogen bonding into molecular structure by the interaction between amine proton donor (-NRH) and carbonyl group (=O) acceptors. The amide group with carbonyl group provide hydrogen-bonding ability which has stronger driving force for self-assembly beyond π−π stacking. The purpose was to achieve the active layer film with better connectivity, higher hole mobility, and ultimately better OPV performance by self-assembling introduced by hydrogen bonding between the donor materials.

3.2 Structure Simulation by Density Functional Theory (DFT)

In order to introduce hydrogen bonding into the molecule, 2-butyloctan-1-amine or 2-hexyldecan-1-amine was simply attached onto our starting material (5-bromothiophene-3-carboxylic acid).

D-A polymer **PBTDCA(H)-BT** was designed using BTDCA with two different lengths of carbon chains as an acceptor and copolymerized with BT as a comonomer unit. First, we studied the geometry optimization of each repeating unit of the **PBTDCA(H)-BT** by computer simulation based on density functional theory. During the computer simulation, the carbon chain on the amide was substituted by methyl groups for simplifying the calculation as shown in **Figure 3-1 (a)**. The orbital surfaces of HOMO/LUMOs of PBTDCA(H)-Me-BT were generated to visualize the electron distribution on the molecular orbitals and the calculated HOMO/LUMO energy levels with respect to vacuum (0 eV) are shown in **Figure 3-1 (b)** and **(c).**

It is clear from **Figure 3-1** that the electrons are evenly distributed over the whole molecule in both the HOMO and LUMO of the PBTDCA(H)-Me-BT. This indicates that the PBTDCA(H)-Me-BT has high degree of conjugation.

(a)

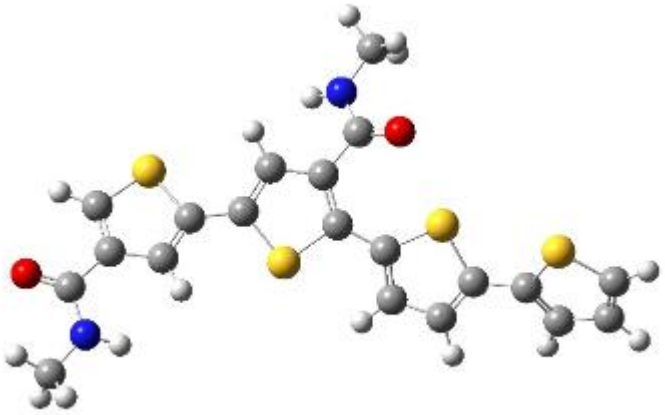

(b)

LUMO = -2.0 eV

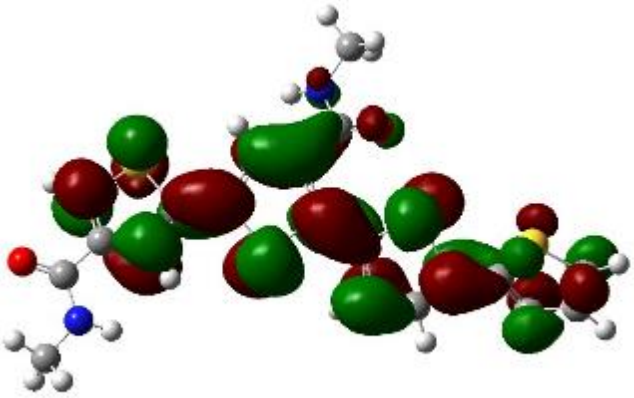

(c)

HOMO = -5.2 eV

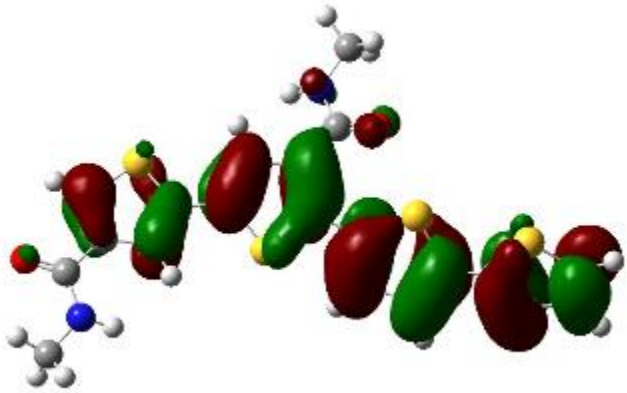

Figure 3-1 (a) optimized geometry of PBTDCA(H)-Me-BT. (b) HOMO /(c)LUMO orbitals of PBTDCA(H)-Me-BT and the calculated HOMO/LUMO levels with respect to vacuum (0 eV).

3.3 Synthesis of PBTDCA(H)-BT

After introducing hydrogen bonding into the polymer, the side chain length was optimized again to obtain appropriate properties of the polymers such as solubility. Different lengths of branched chains were used for **P5 (C12)** and **P6 (C16).** Both **P5** and **P6** were prepared via Stille coupling polymerization of BTDCA(H) with 5,5′-bis(trimethylstannyl)-2,2′-bithiophene,

and purified using Soxhlet extraction shown in **Scheme 5**. During the Soxhlet extraction, **P5** and **P6** showed very poor solubility, and could not be dissolved in common organic solvents such as chloroform, chlorobenzene and dichlorobenzene. Later, the more polar solvent *m*-cresol was used to test the dissolution of the two polymers. **P5** still could not be dissolved in *m*-cresol. The synthesis procedures are shown in section 3.8 and the following NMR spectra are shown in Appendix A.

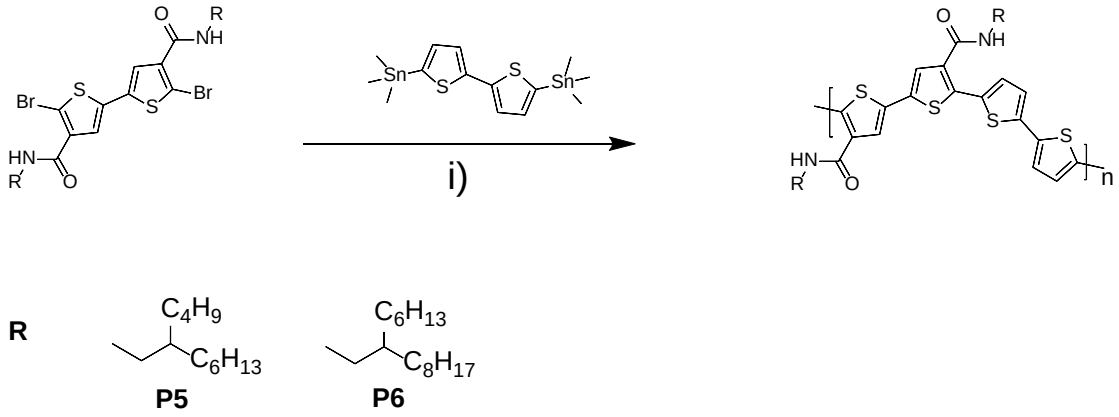

Scheme 5: Synthesis route towards the BTDCA(H) based polymer. Reaction condition: i): Stille coupling 5,5′-bis(trimethylstannyl)-2,2′-bithiophene/anhydrous chlorobenzene/ $Pd(PPh_3)_4$ (5%). Yield: 85% in *m*-cresol for **P6**.

3.4 Characterization of PBTDCA(H)-BT by DSC, TGA, UV-Vis, CV, FTIR and XRD

As **P5** could be dissolved in common solvents with the unoptimized side chain, the following characterizations were focused on **P6**. First, DSC and TGA were used to characterize the crystallization and the thermal stability properties of **P6**. A 5% weight loss was observed at 422 °C **(Figure 3-2)**, indicating good thermal stability of this **P6** polymer. From the DSC curve, no noticeable exothermic or endothermic transitions were observed during the range of -20 °C to 340 °C **(Figure 3-3)**. From the TGA and DSC results, by introducing hydrogen bonding into the polymer did not decrease the thermal stability of the polymer.

The UV-Vis absorption spectra of **P6** in thin film as compared with **P1** and **P2** are shown in **Figure 3-4**, as all these three polymers used BT as an acceptor. **P3** exhibited typical single absorption peak which is similar to those of **P1** and **P2**. The λ_{max} for **P1** and **P2** thin films were 503 nm and 495 nm while **P6** exhibited more red-shift adsorption wavelength at 547 nm. Moreover, a weak shoulder appeared at 581 nm, indicating the more extended conjugation of the polymer chains in the solid state compared with **P1** and **P2**. The optical bandgap of the polymer thin film was calculated to be ~1.87 eV, using the thin film absorption onsets. This is much lower than **P1** and **P2** with ~2.04 eV. Interestingly, according to the UV-Vis absorption spectra, introducing hydrogen bonding into the **P6**, resulted in a more ordered inter chains stacking, thus lowering the bandgap.

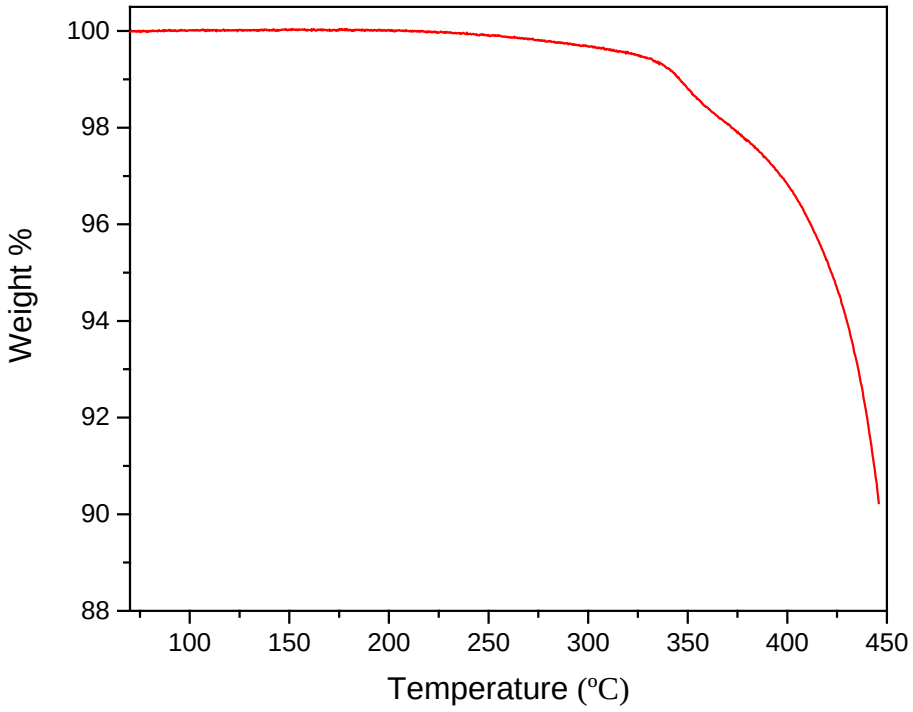

Figure 3-2 The TGA curve of **P6** obtained with temperature increasing rate of 10 °C min^{-1} in nitrogen.

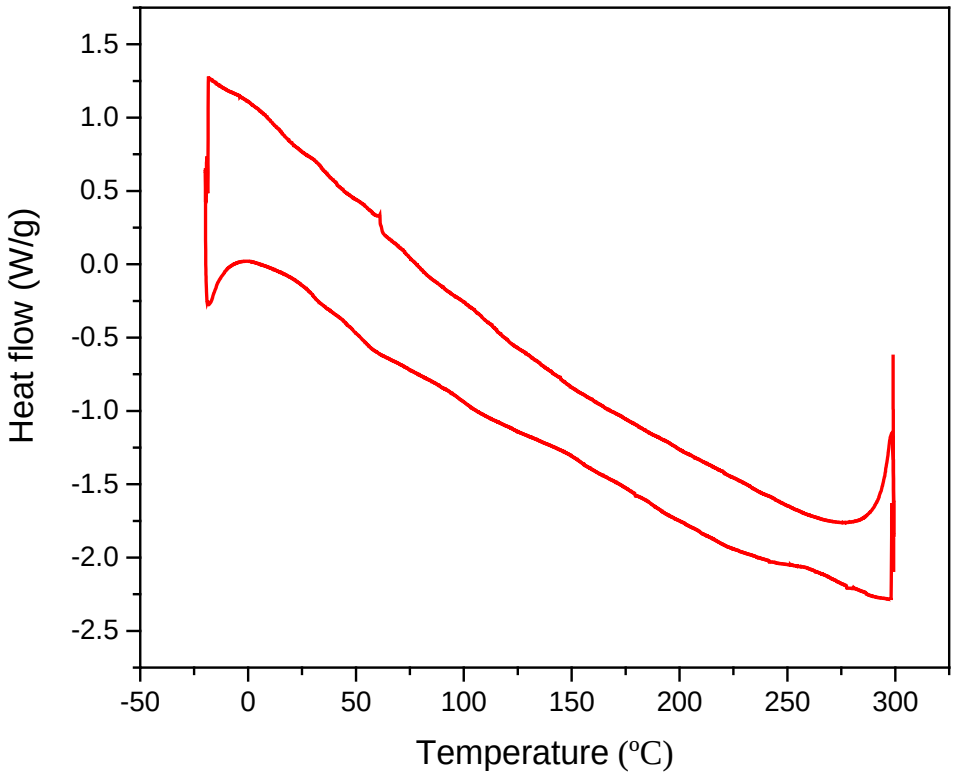

Figure 3-3 DSC profile of **P6** obtained at a scanning rate of 10 °C min^{-1} under nitrogen.

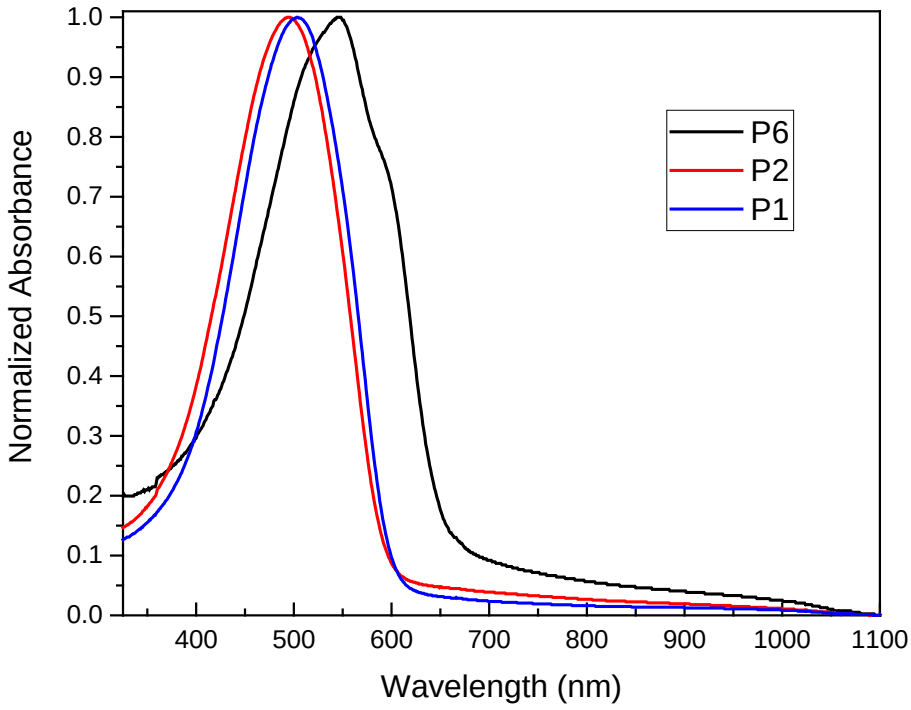

Figure 3-4 Normalized UV-vis absorption spectra of **P1**, **P2** and **P6** in thin film.

CV was used to reveal the electrochemical behavior of the polymers (**Figure 3-5**). By using the oxidative onset potentials, the HOMO levels were estimated from the oxidation onset potentials to be -5.4 eV for **P6**. Similar result was found for **P1** and **P2**. This shows that changing the side chain might not change the HOMO level significantly.

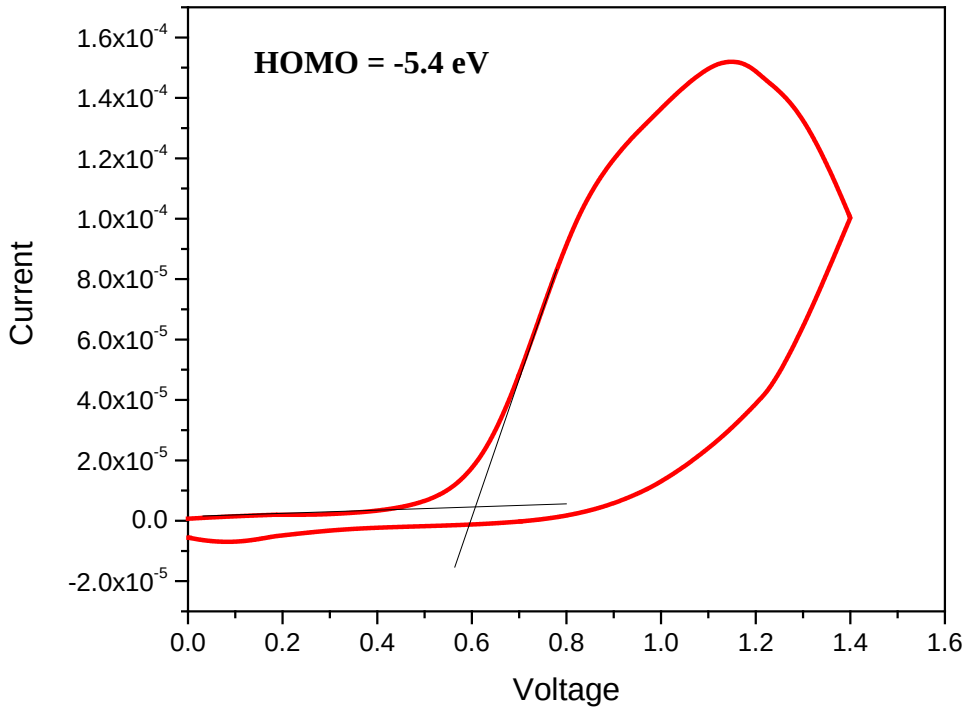

Figure 3-5 The CV diagram of **P6** at a scan rate of 0.1 V/s. The electrolyte was 0.1 M tetrabutylammonium hexafluorophosphate in anhydrous acetonitrile.

The packing of polymer thin films of **P6** was characterized by XRD. As shown in **Figure 3-6**, at RT and 100 ℃, small peaks can be seen while other polymers in this work did not show a distinct peak until annealed at 100 ℃. After the thin film was annealed at 150 ℃ and 200 ℃, **P6** showed more intense peaks at 2θ = 4.08° and 4.12°, which correspond to the interlayer lamellar *d*-spacing of 2.17 nm and 2.15 nm, respectively.

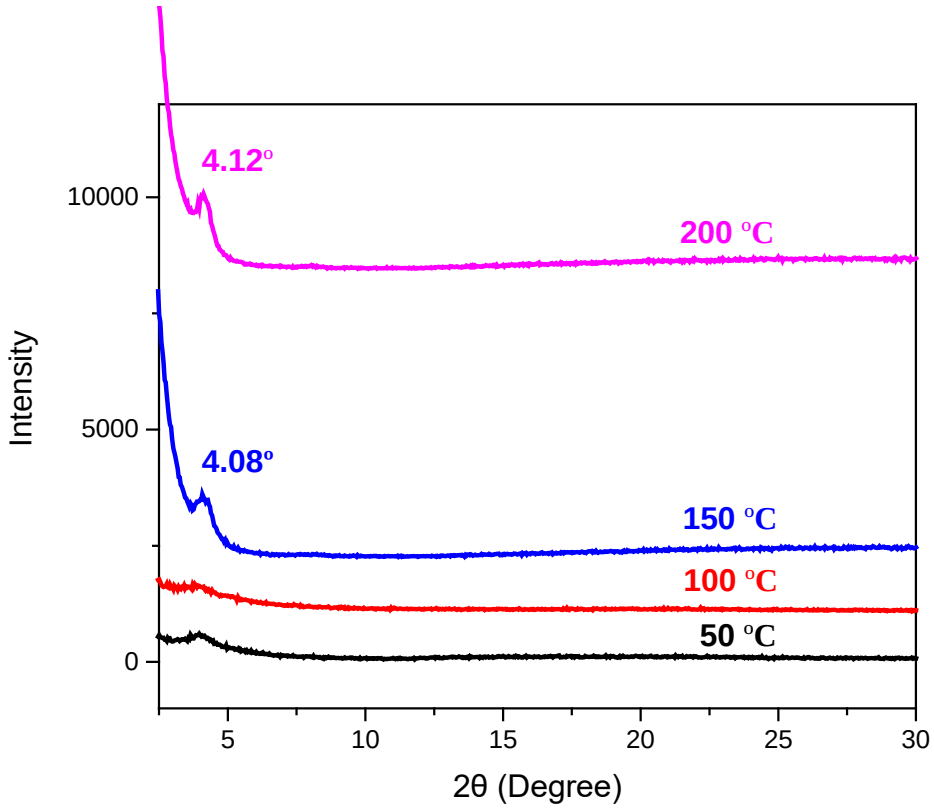

Figure 3-6 The XRD diagram obtained from the spin-coated **P6** thin film on DDTS-modified SiO_2/Si substrates.

In addition, FTIR was used to characterize the hydrogen bonding in **P6**. The sample was prepared by dropping **P6** solution onto sodium chloride optical crystals and removing the solvent by vacuum which was then annealed at 100 ℃, 150 ℃ and 200 ℃ for 20 min successively. The FTIR spectra for the sample annealed at different temperature **(Figure 3-7)** showed an N-H stretching frequency at 3292 cm^{-1} which was characteristic for hydrogen bonded amide groups.[96,103]

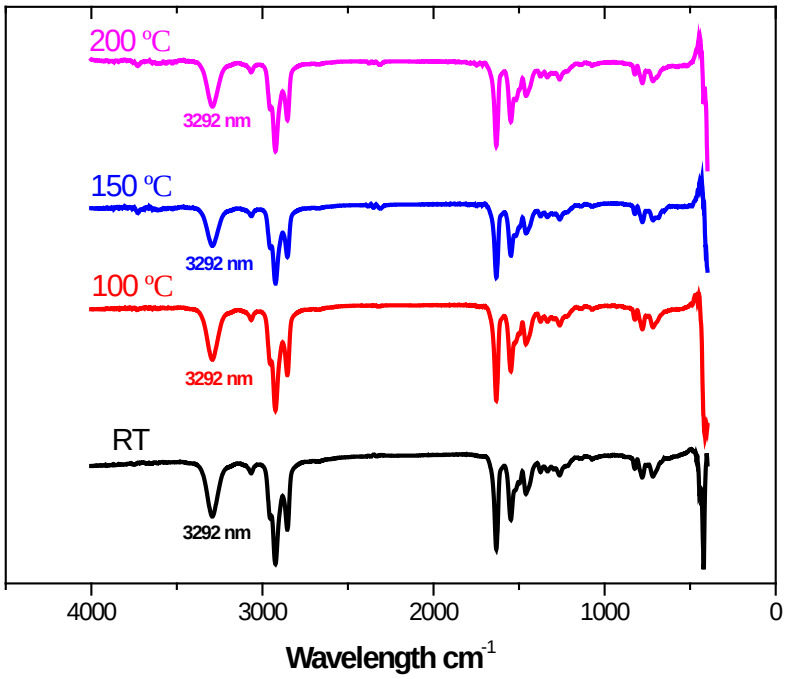

Figure 3-7 The FTIR spectra of **P6** in solid state.

3.5 OTFT Performances of PBTDCA(H)-BT

The OTFT performance of **P6** was evaluated as channel semiconductors in bottom-gate, bottom-contact OTFT devices fabricated on DDTS modified SiO_2/Si wafer substrates. The OTFT fabrications and characterizations are shown in section 2.7.2. The polymers showed p-type charge transport behavior **(Table 3-2)**. The transfer curves and output curves are shown in **Figure 3-8**. At RT, the hole mobility was measured to be 6.4×10^{-3} $cm^2 V^{-1} s^{-1}$, which is the highest among all the polymers in this work and ten times that of **P2** 3.3×10^{-4} $cm^2 V^{-1} s^{-1}$. After annealing at higher temperature (150 ℃ and 200 ℃), the hole mobility quickly increased by one order of magnitude to 10^{-2} $cm^2 V^{-1} s^{-1}$ and reached the highest hole mobility of 2.6×10^{-2} $cm^2 V^{-1} s^{-1}$. From the previous results and OTFT results, the hydrogen bonding improved

the interaction between the polymer chains for long range ordered packing, resulting in better connectivity and higher hole mobility in the polymer thin film.

Table 3-2 Summary of BGBC OTFT performance of **P6**.

Polymer	Annealing[a] temperature (°C)	Hole mobility[b] (10^{-2} cm^2 V^{-1} s^{-1})	Vth[c] (V)	$I_{ON/OFF}$
P6	RT	0.63 ± 0.012 (0.64)	-68	10^4
	100	1.4 ± 0.12 (1.5)	-50	10^5
	150	2.2 ± 0.025 (2.2)	-49	10^4
	200	2.5 ± 0.092 (2.6)	-54	10^5

[a] The devices were annealed in a glove box on a hotplate at the selected temperature for 20 min under argon. Hole mobilities were obtained in the saturated regions in hole enhancement modes. Each set of data were obtained from 3-5 OTFT devices.

[b] The average mobility ± standard deviation (maximum mobility) calculated from the saturation regions of the devices.

[c] The Vth calculated from the device with maximum mobility.

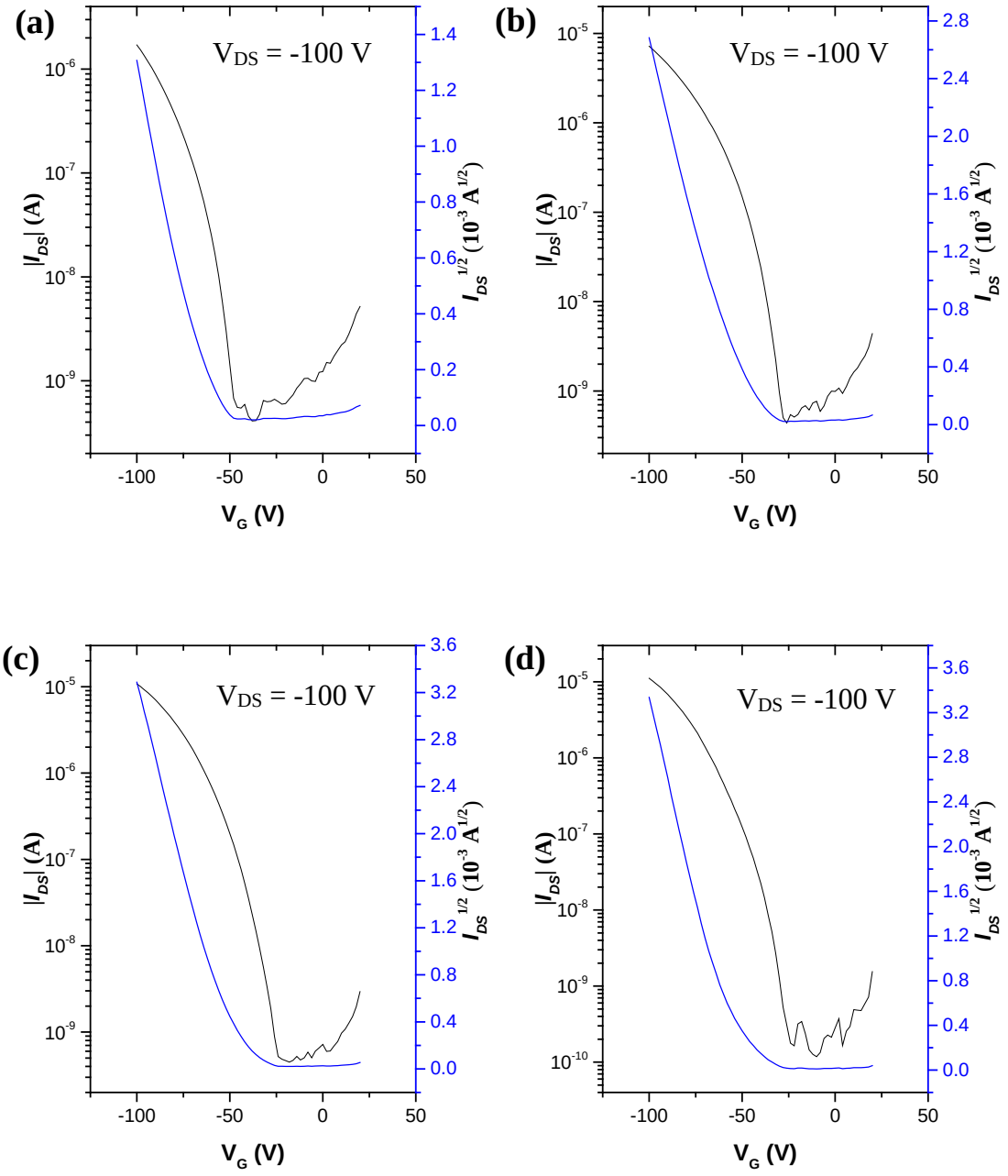
(a)
V_DS = -100 V
|I_DS| (A)
I_DS^1/2 (10^-3 A^1/2)
V_G (V)
(b)
V_DS = -100 V
|I_DS| (A)
I_DS^1/2 (10^-3 A^1/2)
V_G (V)
(c)
V_DS = -100 V
|I_DS| (A)
I_DS^1/2 (10^-3 A^1/2)
V_G (V)
(d)
V_DS = -100 V
|I_DS| (A)
I_DS^1/2 (10^-3 A^1/2)
V_G (V)

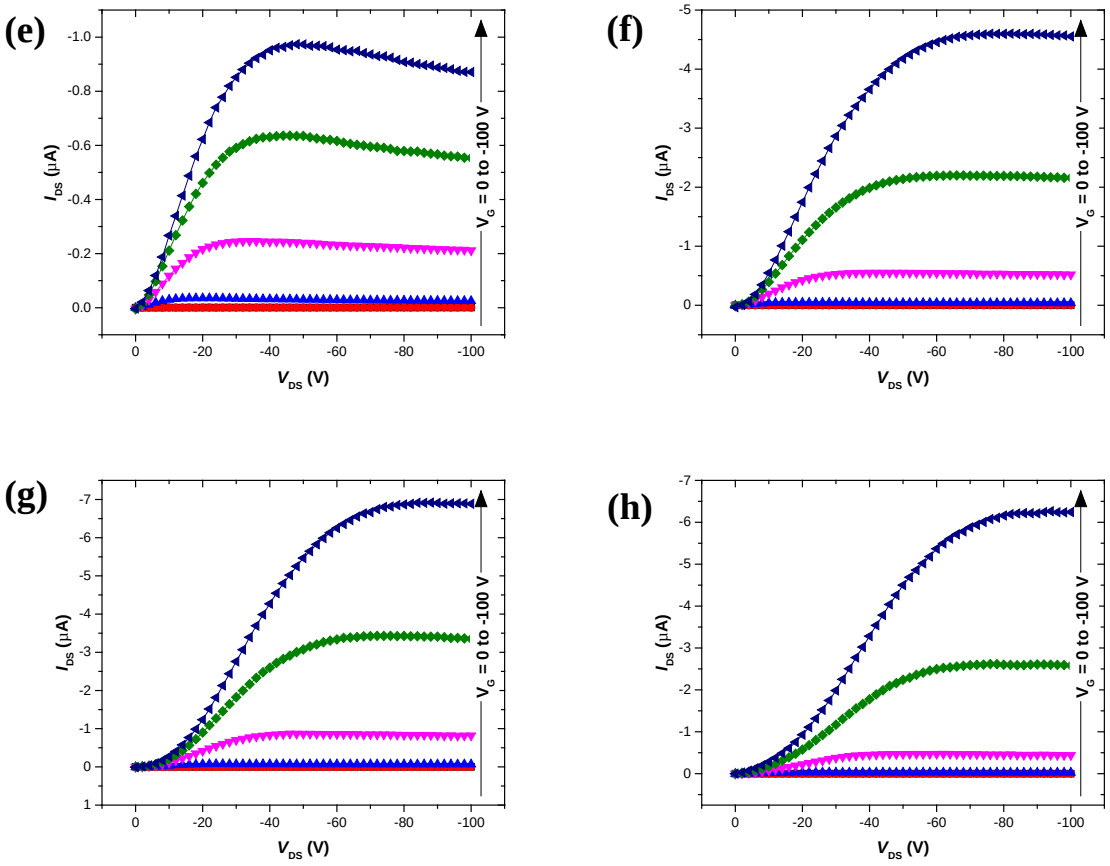

Figure 3-8 The transfer curves (a), (b), (c) and (d) and output curves (e), (f), (g) and (h) for OTFTs based on **P6** annealed at RT, 100 ℃, 150 ℃ and 200 ℃, respectively. Device dimensions: channel length (L) = 30 μm; channel width (W) = 1000 μm. V_G valued from 0 to -100 V in the step of -20 V in output curves.

3.6 OPV Performances of P6

The results for **P6** based solar cells are shown in **Figure 3-9** and **Table 3-3**. The OPV fabrications and characterizations are shown in section 2.7.3. As for the poor solubility of **P6**, the film showed uneven and rough grainy morphology visible with the naked eye, which prevent the formation of bi-continuous and interpenetrating morphology. Therefore, although

the HOMO level of **P6** is similar to **P3** and **P2**, the Voc is much lower (0.45 V). Consequently, the device based on **P6**: $PC_{61}BM$ showed poor performance (PCE = 0.14%).

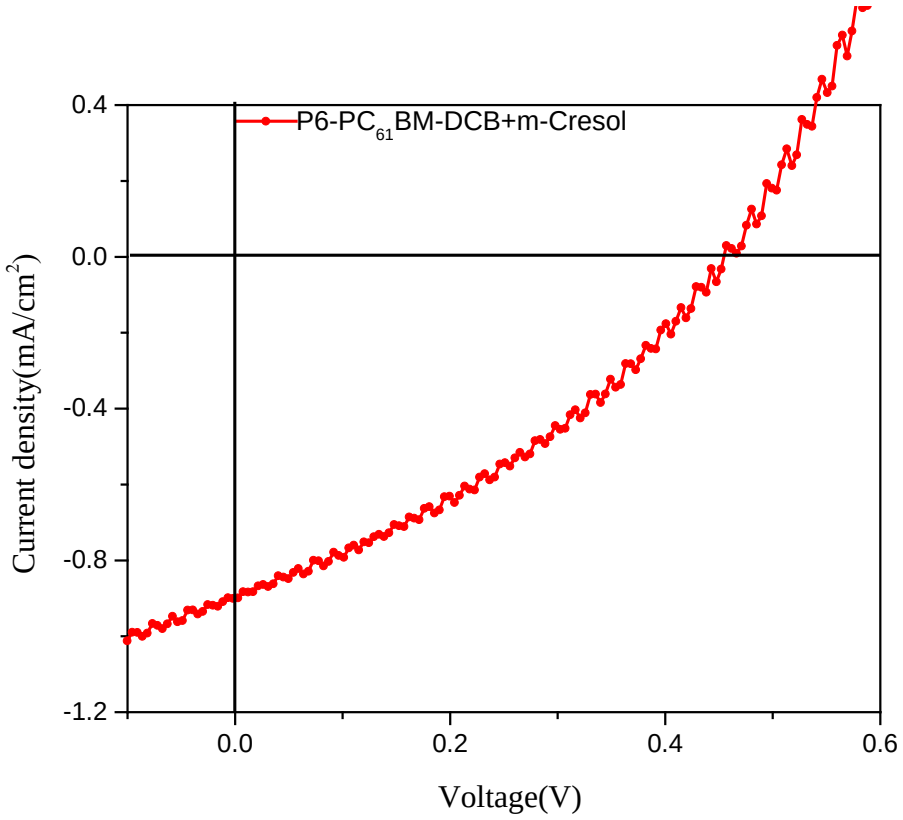

Figure 3-9 The J-V curve based on **P6**: $PC_{61}BM$ under AM 1.5G illumination.

Table 3-3 Summary of OPV performance of **P6**: $PC_{61}BM$

Active layer	**Ratio**	**Solvent**	**Annealing temperature (℃)**	**Jsc (mA/cm^2)**	**Voc (V)**	**FF**	**PCE %**	**Rs (ohm/ cm^2)**	**Rsh (ohm/ cm^2)**
P6: $PC_{61}BM$	1: 1	DCB (10%) + *m*-cresol (90%)	RT	0.9	0.45	0.35	0.14	278	918

3.7 Summary and Future Directions

Hydrogen bonding was introduced into BTDCA to form BTDCA(H) for its self-assembling architectures which can strengthen interactions between polymer chains. **P5** and **P6** were synthesized with different lengths of side chains and using BT as comonomer unit. Both **P5** and **P6** showed very poor solubility in common organic solvents. **P6** could be dissolved in a more polar solvent (*m*-cresol), while **P5** could not be dissolved due to its shorter side chain, which prompted interactions between molecules. **P6** showed good thermal stability from TGA data. From UV-vis absorption spectra, **P6** showed more extended conjugation of the polymer chains in the solid state compared with **P1** and **P2**, probably due to the strengthened intermolecular interaction by hydrogen bonding. As the result, **P6** showed high hole mobility (up to 2.6 $\times 10^{-2}$ $cm^2 V^{-1} s^{-1}$), which is 18 times that of **P2**. For solar cells performance, although the HOMO level of **P6** was similar to **P3**, **P6** based solar cells showed even low Voc. And the film showed uneven and rough grainy morphology visible with the naked eye due to poor solubility. Due to the high mobility and hydrogen bonding, future work can apply **P6** into organic semiconductor sensors such as pH sensor. Another approach can focus on improving the solubility of **P6** for solar cell application.

3.8 Experimental Section

3.8.1 Synthesis Procedures

Synthesis of 5-Bromo-N-(2-butyloctyl)-thiophene-3-carboxamide (8)

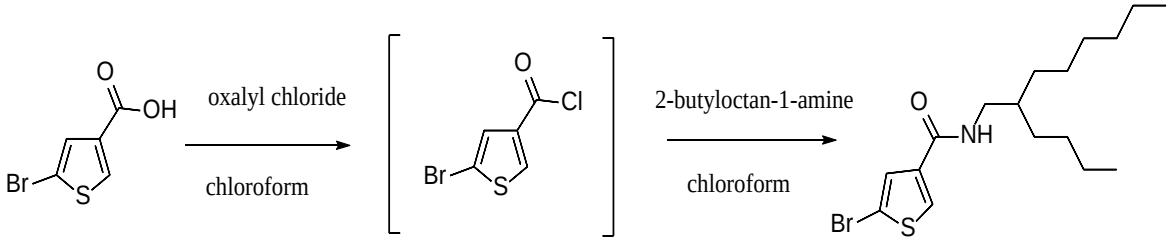

1 **8**

5-Bromothiophene-3-carboxylic acid was dissolved in 20 mL of anhydrous chloroform in a heat gun-dried round bottom flask. The solution was cooled to 0 °C in an ice bath. Oxalyl chloride was added dropwise followed with one drop of DMF as a catalyst. The solution was allowed to warm to room temperature overnight. Unreacted oxalyl chloride was removed under reduced pressure.

To a heat gun-dried round bottom flask, 2-butyloctan-1-amine in 5 mL of anhydrous chloroform was added. The solution was cooled to 0 °C in an ice bath. Crude 5-Bromothiophene-3-carbonyl chloride dissolved in 10 mL of anhydrous chloroform was added dropwise. The solution was stirred at room temperature overnight. The reaction was quenched by addition of water. The organic layer was separated and rinsed with brine and dried over Na_2SO_4. Upon removal of solvent in vacuo, the crude product was further purified by silica gel column chromatography with hexane: ethyl acetate (5:1) to give Compound 8. Yield 2.80 g, (86%).

^{1}H NMR (300 MHz, chloroform-*d*) δ 7.73 (d, *J* = 2.0 Hz, 1H), 7.30 (d, *J* = 1.8 Hz, 1H), 5.88 (s, 1H), 3.33 (td, *J* = 6.1, 2.1 Hz, 2H), 1.57 (s, 1H), 1.40 – 1.26 (m, 16H), 0.97 – 0.85 (m, 6H).

Synthesis of N^4, $N^{4'}$-bis(2-butyloctyl)-[2,2'-bithiophene]-4,4'-dicarboxamide (9)

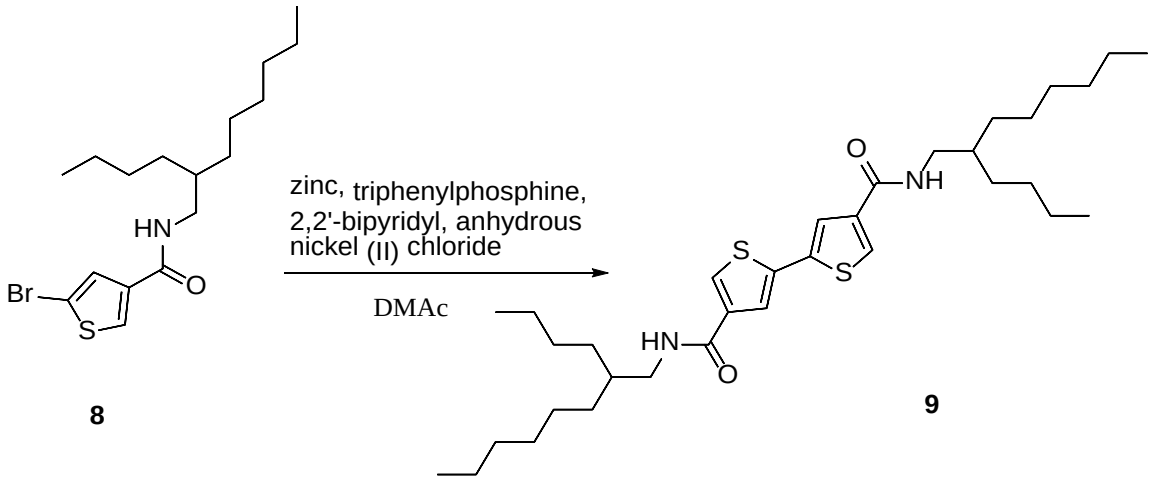

8 **9**

To a 50 mL of flask were added N, N-dihexyl-3-thiophenecarbamide, zinc powder, triphenylphosphine, 2,2'-bipyridyl, anhydrous nickel (II) chloride. The mixture was degassed and filled with argon three times and then DMAc (18 mL) was added. The mixture was heated

to 80 °C and maintained overnight (the TLC showing no starting material). The reaction mixture was cooled down to room temperature and poured into a cold HCl. After extraction with ethyl acetate, the organic layer was dried with Na_2SO_4. The solvent was removed under reduced pressure. The crude product was dissolved in chloroform and precipitated in diethyl ether. Compound 9 was collected by filtration and dried in the vacuum. Yield: 0.65 g, (31%). ^{1}H NMR (300 MHz, chloroform-*d*) δ 7.70 (s, 2H), 7.43 (s, 2H), 5.91 (t, *J* = 5.8 Hz, 2H), 3.37 (t, *J* = 6.0 Hz, 4H), 1.37 – 1.26 (m, 32H), 0.89 (q, *J* = 7.0 Hz, 12H).

Synthesis of 5,5'-Dibromo-N^4, N$^{4'}$-bis(2-butyloctyl)-[2,2'-bithiophene]-4,4'-dicarboxamide (10)

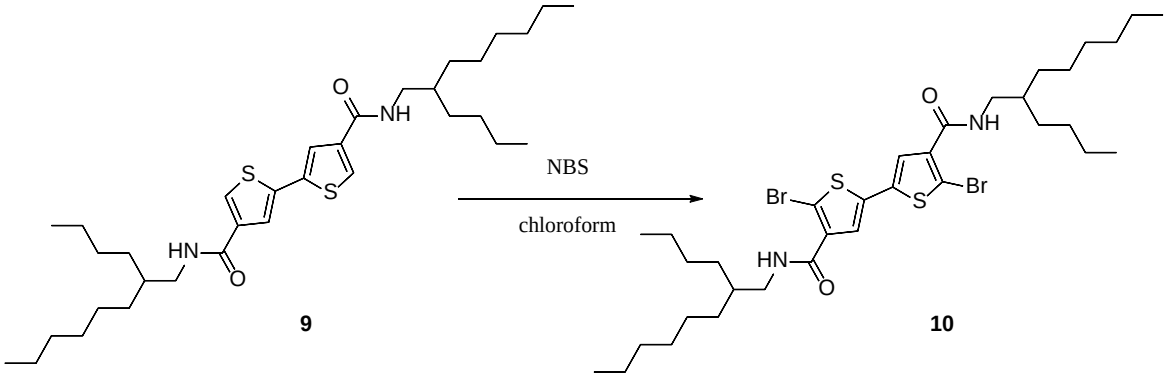

9 **10**

N^4, N$^{4'}$-bis(2-butyloctyl)-[2,2'-bithiophene]-4,4'-dicarboxamide (0.5 g, 0.85 mmol) was dissolved in a mixture of chloroform (5 mL) and trifluoracetic acid (1 mL). NBS (0.3173 g, 1.78 mmol) was then added to the solution and stirred overnight in the dark covered with aluminum foil. The mixture was extracted with chloroform several times and the organic phase was combined and washed by sodium sulfite aqueous solution. The organic phase was dried with Na_2SO_4 and the solvent was removed under reduced pressure. The crude product was washed by diethyl ether and collected by filtration. Compound 10 was dried in vacuum. Yield: 0.58 g, (92%).

^{1}H NMR (300 MHz, chloroform-*d*) δ 7.37 (s, 2H), 6.43 (t, *J* = 5.7 Hz, 2H), 3.40 (t, *J* = 5.8 Hz, 4H), 1.62 (s, 2H), 1.31 (dd, *J* = 13.3, 5.8 Hz, 32H), 0.96 – 0.83 (m, 12H). ^{13}C NMR (75 MHz,

chloroform-*d*) δ 161.55, 137.40, 135.65, 126.23, 110.83, 43.06, 37.75, 32.00, 31.83, 31.66, 29.66, 28.88, 26.65, 23.02, 22.65, 14.09.

Synthesis of P5

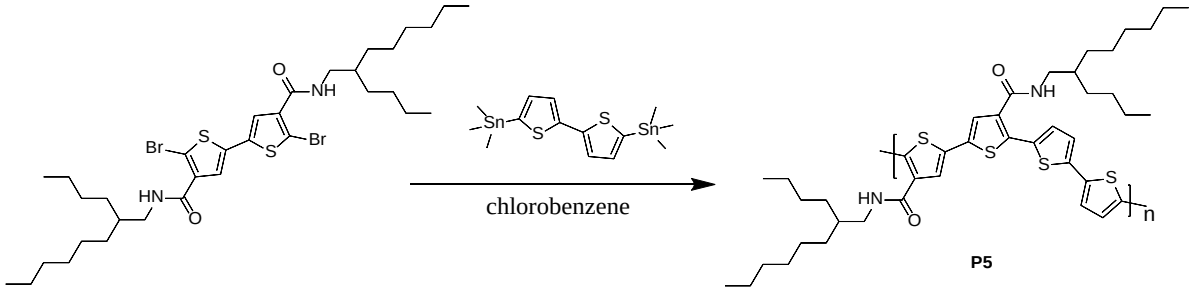

To a 25 mL double-neck round-bottom flask, N^4, $N^{4'}$-bis(2-butyloctyl)-[2,2'-bithiophene]-4,4'-dicarboxamide (149.4 mg, 0.2 mmol) and 5, 5'-bis(trimethylstannyl)-2,2'-bithiophene (98.4 mg, 0.2 mmol) were added. After degassing and refilling argon three times, chlorobenzene (7 mL) was added to dissolve the mixture, followed by addition of $Pd(PPh_3)_4$ (11.6 mg, 0.01 mmol). The mixture was heated to 120 ℃ for 40 h. The reaction mixture was cooled down to room temperature and poured into MeOH (100 mL). The precipitate was collected by filtration and subjected to Soxhlet extraction with acetone, hexane, chloroform and chlorobenzene. The polymer showed very poor solubility which cannot be dissolved in common organic solvents.

Synthesis of 2-Hexyldecan-1-amine (11)

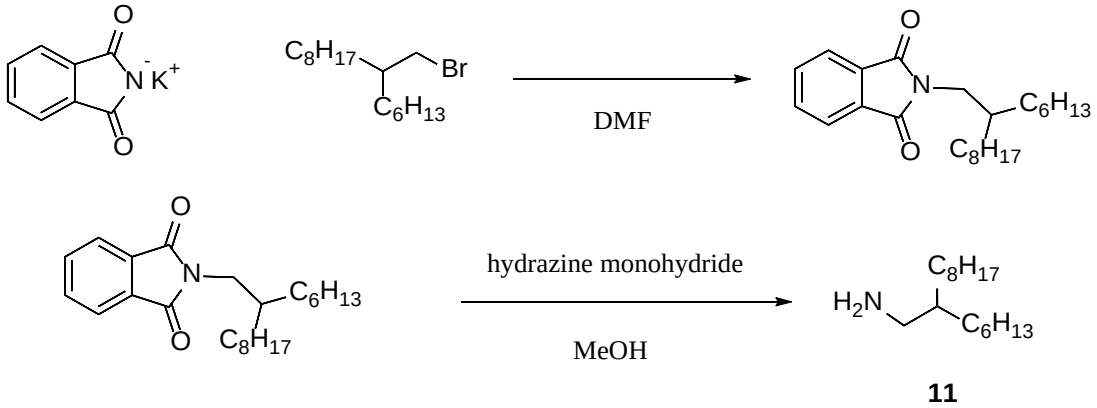

7-(Bromomethyl)pentadecane and potassium phthalimide were dissolved in DMF in a 100 mL 2-neck round-bottom. The mixture was stirred on hot plate at 90 ℃ overnight. The solution

was extracted with DCM and DI water for three times to remove DMF and other trace amounts of impurity. The organic phases were collected and concentrated through vacuum. Column was firstly flushed by hexane, to remove alkyl chains, and any other impurities. Once TLC showed removal of impurities, solvent was switched to pure DCM. The intermediate product (2-(2-hexyldecyl)-isoindoline-1,3-dione) was obtained.

To a solution of in MeOH (90 mL), hydrazine monohydride was added and refluxed overnight. After the solution was cooled to room temperature, the mixture was evaporated under vacuum. The residue was dissolved in DCM and washed with 10 wt % KOH aq. (100 mL × 2) and saturated NaCl aq. (100 mL × 2). The organic phases were dried with Na_2SO_4 and concentrated through vacuum. The compound was used for the subsequent reaction without further purification, as colorless oil. Yield: 6.67 g, (93%).

^{1}H NMR (300 MHz, chloroform-*d*) δ 2.59 (d, *J* = 3.9 Hz, 2H), 1.26 (s, 27H), 0.93 – 0.83 (m, 6H).

Synthesis of 5-Bromo-N-(2-hexyldecyl)-thiophene-3-carboxamide (12)

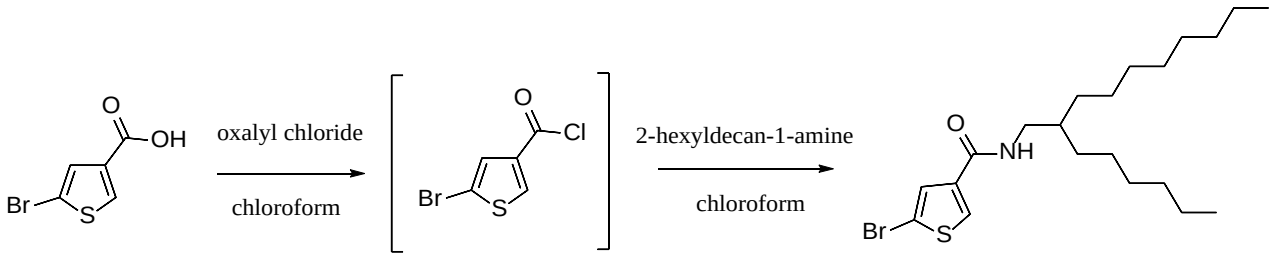

1 **12**

5-Bromothiophene-3-carboxylic acid (2.28 g, 11 mmol) was dissolved in 20 mL of anhydrous chloroform in a heat gun-dried round bottom flask. The solution was cooled to 0 °C in an ice bath. Oxalyl chloride (2.80 g, 22 mmol) was added dropwise followed with one drop of DMF as a catalyst. The solution was allowed to warm to room temperature overnight. Unreacted oxalyl chloride was removed under reduced pressure.

To a heat gun-dried round bottom flask, 2-hexyldecan-1-amine (5.31 g, 22 mmol) in 5 mL of anhydrous chloroform was added. The solution was cooled to 0 °C in an ice bath. Crude 5-bromothiophene-3-carbonyl chloride dissolved in 10 mL of anhydrous chloroform was added

dropwise. The solution was stirred at room temperature overnight. The reaction was quenched by addition of water. The organic layer was separated and rinsed with brine and dried with Na_2SO_4. Upon removal of solvent in vacuo, the crude product was further purified by silica gel column chromatography with hexane: ethyl acetate (5:1) to give Compound 12. Yield: 4.2 g, (95%).

^{1}H NMR (300 MHz, chloroform-*d*) δ 7.73 (d, *J* = 1.6 Hz, 1H), 7.30 (d, *J* = 1.6 Hz, 1H), 5.87 (t, *J* = 5.7 Hz, 1H), 3.33 (t, *J* = 6.0 Hz, 2H), 1.60 – 1.53 (m, 1H), 1.33 – 1.24 (m, 24H), 0.90 – 0.85 (m, 6H).

Synthesis of N^4, $N^{4'}$-bis(2-hexyldecyl)-[2,2'-bithiophene]-4,4'-dicarboxamide (13)

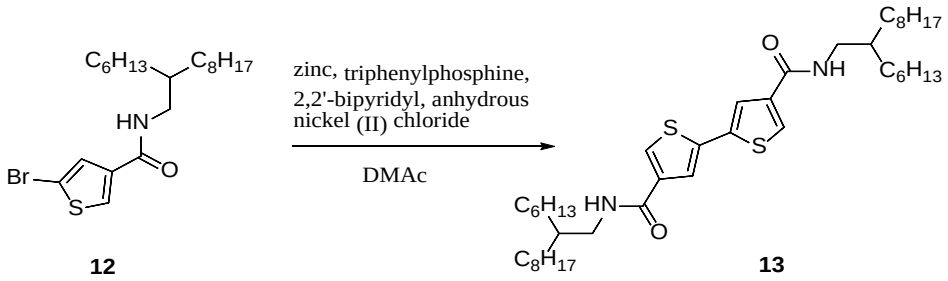

12 **13**

To a 50 mL of flask were added 5-bromo-N-(2-hexyldecyl)-thiophene-3-carboxamide, zinc powder, triphenylphosphine, 2,2'-bipyridyl, anhydrous nickel (II) chloride. The mixture was degassed and filled with argon three times and then DMAc (18 mL) was added. The mixture was heated to 80 ℃ and maintained overnight (the TLC showing no starting material). The reaction mixture was cooled down to room temperature and poured into a cold HCl. After extraction with ethyl acetate, the organic layer was dried with Na_2SO_4. The solvent was removed under reduced pressure. The crude product was dissolved in chloroform and precipitated in diethyl ether. Compound 13 was collected by filtration and dried in the vacuum. Yield: 0.65 g, (31%).

^{1}H NMR (300 MHz, chloroform-*d*) δ 7.70 (d, *J* = 1.5 Hz, 2H), 7.43 (d, *J* = 1.6 Hz, 2H), 5.90 (t, *J* = 5.8 Hz, 2H), 3.36 (t, *J* = 6.0 Hz, 4H), 1.35 – 1.24 (m, 50H), 0.87 (dt, *J* = 7.0, 3.5 Hz, 6H).

Synthesis of 5,5'-Dibromo-N^4, $N^{4'}$-bis(2-hexyldecyl)-[2,2'-bithiophene]-4,4'-dicarboxamide (14)

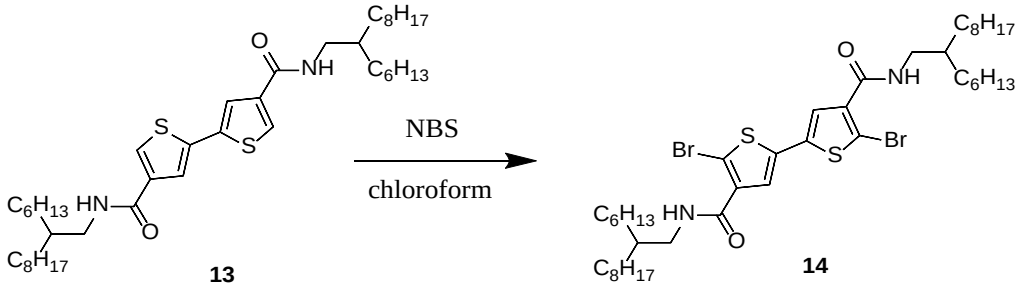

N^4, $N^{4'}$-bis(2-hexyldecyl)-[2,2'-bithiophene]-4,4'-dicarboxamide (0.6 g, 0.85 mmol) was dissolved in a mixture of chloroform (5 mL) and trifluoracetic acid (1 mL). NBS (0.32 g, 1.78 mmol) was then added to the solution and stirred overnight in the dark covered with aluminum foil. The mixture was extracted with chloroform several times and the organic phases were combined and washed by sodium sulfite aqueous solution. The organic phase was dried with Na_2SO_4 and the solvent was removed under reduced pressure. The crude product was purified via column chromatography using chloroform as elute solvent, then washed by diethyl ether and collected by filtration. Compound 14 was dried in vacuum. Yield: 0.58 g, (78%).

^{1}H NMR (300 MHz, chloroform-*d*) δ 7.37 (s, 2H), 6.42 (t, *J* = 5.6 Hz, 2H), 3.40 (t, *J* = 5.8 Hz, 4H), 1.62 (s, 2H), 1.37 – 1.25 (m, 48H), 0.91 – 0.84 (m, 12H). ^{13}C NMR (75 MHz, chloroform-*d*) δ 161.55, 137.40, 135.64, 126.16, 110.85, 43.08, 37.77, 31.99, 31.90, 31.83, 30.00, 29.66, 29.58, 29.31, 26.68, 26.65, 22.66, 14.10.

Synthesis of P6

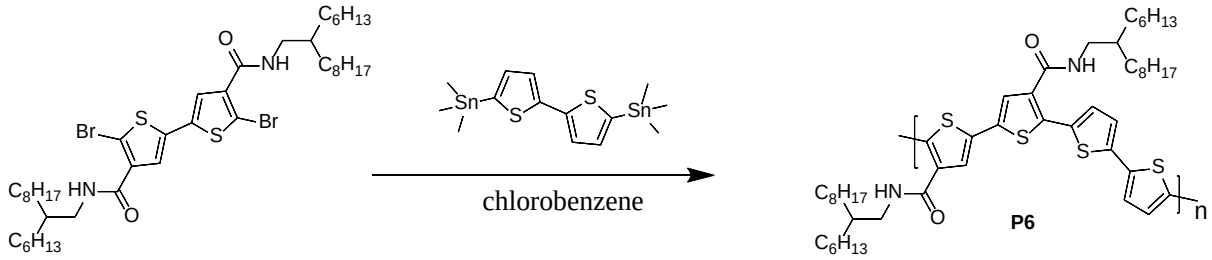

To a 25 mL double-neck round-bottom flask of 5,5'-dibromo-N^4, $N^{4'}$-bis(2-hexyldecyl)-[2,2'-bithiophene]-4,4'-dicarboxamide (171.8 mg, 0.2 mmol) and 5, 5'-bis(trimethylstannyl)-2,2'-bithiophene (98.4 mg, 0.2 mmol). After degassing and refilling argon three times,

chlorobenzene (7 mL) was added to dissolve the mixture, followed by addition of $Pd(PPh_3)_4$ (11.56 mg, 0.01 mmol). The mixture was heated to 120 ℃ for 40 h. The reactant was cooled down to room temperature and poured into MeOH (100 mL). The precipitate was collected by filtration and subjected to Soxhlet extraction with acetone, hexane, chloroform and chlorobenzene and *m*-cresol. The polymer was finally recovered in *m*-cresol. Yield: 0.137 g, (85%).

Chapter 4 Summary and Future Directions

The novel electron-deficient building blocks BTDCA and BTDCA(H) (with hydrogen bonding) were prepared and incorporated into D-A copolymers. The polymer design with the PT backbone was based on P3HT, a well-studied donor material for OPVs, which has planar conformation, high crystallinity and strong inter- and intramolecular interactions. However, the relative high HOMO level leads to inevitable drawbacks, resulting in low Voc in solar cells. The new design employs an amide electron-deficient functional group in order to fix this problem. Different side chain lengths of the polymers were tuned and three electron rich building blocks, BT, TT and T, were used to form copolymers. All of the polymers in this work have been reported for the first time.

In chapter 2, DFT was used to study the coplanarity, electron distribution, and energy levels of the BTDCA. By comparing the energy levels with BT, the HOMO level was decreased as desired.

As a proof of concept, **P1** and **P2** were synthesized with different lengths of side chains, using BT as comonomer unit. Both polymers showed high thermal stability, similar single absorption peak in UV-vis absorption spectra (typical for PT materials) and deeper HOMO level -5.3 eV as compared to P3HT (-4.9 eV). XRD of **P2** showed higher degree of crystallinity than **P1**, due to shorter side chain, resulting in higher hole mobility (up to 1.4×10^{-2} $cm^2 V^{-1} s^{-1}$), which is almost ten times that of **P1** (up to 2×10^{-3} $cm^2 V^{-1} s^{-1}$). From preliminary OPVs results, both polymers exhibited higher Voc (up to 0.87 V) than P3HT (0.59 V) using same acceptor $PC_{61}BM$. Thus, the Voc was improved in these solar cells by attaching amide functional group onto the PT.

Though Voc for **P1** and **P2** based solar cells were increased compared with P3HT based solar cells, the PCE values were low. This low PCE might be due to the high crystallinity which can form large grains in the thin film as observed from AFM images, which reduced the charge separation and transportation efficiency.

Based on section 2.4, **P3** was synthesized with smaller comonomer unit TT instead of BT to decrease the crystallinity. As TT has similar electron property as BT, and the HOMO level for **P3** stayed similar as **P1** and **P2**. From the XRD results, the decrease in crystallinity was confirmed. By decreasing the crystallinity, the hole mobility also decreased to 4.5×10^{-4} cm^2 V^{-1} s^{-1} for **P3**. Interestingly, even with the lower hole mobility, higher PCE was achieved for **P3**: ITIC blend. The PCE was as high as 3.5%, which is four times that of **P2**: ITIC blend (0.85%). The might be due to the optimized thin film morphology. It can be noted that, the solubility of **P3** was not that good after structure optimization. Future work based on **P3** can be focused on the following options:

- Increase the solubility by using the longer side chain, but at the same time, longer chain might decrease the crystallinity which can reduce the charge transportation efficiency.
- Co-solvent[104] and different additives[105,106] can be used to optimize the morphology of the active layer.
- $PC_{61}BM$ and ITIC might not be the perfect acceptor materials which match **P3**, hence finding new acceptors[70–72] may improve the morphology in the blend thin films.

Higher PCE was obtained by using small comonomer units TT in **P3** to decrease the high crystallinity from **P2**. **P4** was synthesized by using T as comonomer unit, which is even smaller than TT. From the XRD, **P4** showed amorphous orientation from RT to 150 ℃ annealing temperature. Only a weak peak was observed after the thin film of **P4** was annealed at 200 ℃. As a result, the OTFTs based on **P4** did not turn on until the devices were annealed at 150 ℃ and low hole mobility 3.0×10^{-5} cm^2 V^{-1} s^{-1} was obtained. As for the performance of the solar cells, due to its good solubility and very disordered chain packing, the ideal bi-continuous morphology could not be obtained, thus resulting in less Jsc and lower FF for **P4** based devices, which means the charge collection efficiency was low.

In chapter 3, hydrogen bonding was introduced into BTDCA to form BTDCA(H), for its self-assembling architectures which can strengthen interaction between polymer chains. **P5** and **P6** were synthesized with different lengths of side chain and using BT as comonomer unit. Both **P5** and **P6** showed very poor solubility which could not be dissolved in common organic

solvents. **P6** could be dissolved in a more polar solvent (*m*-cresol), while **P5** still could not be dissolved due to its shorter side chain which caused interactions between molecules. Future work can focus on making random copolymer using BTDCA and BTDCA(H) as acceptor building blocks in order to increase the solubility of the polymer.[107] From UV-vis absorption spectra, **P6** showed more extended conjugation of the polymer chains in the solid state compared with **P1** and **P2**. Thus, **P6** showed high hole mobility (up to 2.6×10^{-2} $cm^2 V^{-1} s^{-1}$) which is two times that of **P2**. For solar cells performance, although the HOMO level of **P6** is similar to **P3**, **P6** based solar cells showed even low Voc. And the film showed uneven and rough grainy morphology visible with the naked eye due to the poor solubility. Later work might focus on increasing the solubility of **P6** since this polymer has ordered molecular packing and highest hole mobility among the polymers in this work.

Bibliography

1 C. Philibert, *Solar Energy Perspectives*, OECD Publishing, Minneapolis, Minnesota, 2011.

2 A. M. Bagher, Introduction to Organic Solar Cells, *Sustainable Energy*, *Sustainable Energy*, 2014, **2**, 85–90.

3 S. Günes, H. Neugebauer and N. S. Sariciftci, Conjugated Polymer-based Organic Solar Cells, *Chemical Reviews*, 2007, **107**, 1324–1338.

4 J. A. Merrigan, *Sunlight to Electricity*, MIT Press, Cambridge, Massachusetts, 1975.

5 Annual Energy Outlook 2018, https://www.eia.gov/outlooks/aeo/pdf/AEO2018.pdf.

6 B. Kippelen and J. L. Brédas, Organic Photovoltaics, *Energy & Environmental Science*, 2009, **2**, 251.

7 R. Memming, *Photoelectrochemical Solar Energy Conversion*, Springer, Berlin, Heidelberg, 1988.

8 P. A. Basore, Large-area Deposition for Crystalline Silicon on Glass Modules, *3rd World Conference on Photovoltaic Energy Conversion*, Osaka, Japan, 2003.

9 R. W. Miles, K. M. Hynes and I. Forbes, Photovoltaic Solar Cells: An Overview of State-of-the-art Cell Development and Environmental Issues, *Progress in Crystal Growth and Characterization of Materials*, 2005, **51**, 1–42.

10 R. N. Bhattacharya, W. Batchelor, J. E. Granata, F. Hasoon, H. Wiesner, K. Ramanathan, J. Keane and R. N. Noufi, CuIn Ga Se -based Photovoltaic Cells, *Solar Energy Materials and Solar Cells*, 1998, **55**, 83–94.

11 H. H. Afify, R. S. Momtaz, W. A. Badawy and S. A. Nasser, Some Physical Properties of Fluorine-doped SnO_2 Films Prepared by Spray Pyrolysis, *Journal of Materials Science: Materials in Electronics*, 1991, **2**, 40–45.

12 Z. Hong, L. Dou, G. Li and Y. Yang, *Tandem Solar Cell—Concept and Practice in Organic Solar Cells*, Springer, Berlin, Heidelberg, 2015.

13 M. Váry, M. Perný, M. Kusko and E. Firický, Organic Semiconductors for Solar Cells – an Overview, *Elektroenergetika*, 2011, **4**, 14–16.

14 G. Dennler, M. C. Scharber and C. J. Brabec, Polymer-Fullerene Bulk-Heterojunction Solar Cells, *Advanced Materials*, 2009, **21**, 1323–1338.

15 M. Kaltenbrunner, M. S. White, E. D. Głowacki, T. Sekitani, T. Someya, N. S. Sariciftci and S. Bauer, Ultrathin and Lightweight Organic Solar Cells with High Flexibility, *Nature Communications*, 2012, **3**, 770.

16 C. W. Tang, Two-layer Organic Photovoltaic Cell, *Applied Physics Letters*, 1986, **48**, 183–185.

17 G. Yu, J. Gao, J. C. Hummelen, F. Wudl and A. J. Heeger, Polymer Photovoltaic Cells: Enhanced Efficiencies via a Network of Internal Donor-Acceptor Heterojunctions, *Science*, 1995, **270**, 1789–1791.

18 P. K. Watkins, A. B. Walker and G. L. B. Verschoor, Dynamical Monte Carlo Modelling of Organic Solar Cells: The Dependence of Internal Quantum Efficiency on Morphology, *Nano Letters*, 2005, **5**, 1814–1818.

19 K. M. Coakley and M. D. McGehee, Conjugated Polymer Photovoltaic Cells, *Chemistry of Materials*, 2004, **16**, 4533–4542.

20 C. R. McNeill and N. C. Greenham, Conjugated-Polymer Blends for Optoelectronics, *Advanced Materials*, 2009, **21**, 3840–3850.

21 J. Peet, J. Y. Kim, N. E. Coates, W. L. Ma, D. Moses, A. J. Heeger and G. C. Bazan, Efficiency Enhancement in Low-bandgap Polymer Solar Cells by Processing with Alkane Dithiols, *Nature Materials*, 2007, **6**, 497–500.

22 M. Svensson, F. Zhang, S. C. Veenstra, W. J. H. Verhees, J. C. Hummelen, J. M. Kroon, O. Inganäs and M. R. Andersson, High-Performance Polymer Solar Cells of an Alternating Polyfluorene Copolymer and a Fullerene Derivative, *Advanced Materials*, 2003, **15**, 988–991.

23 S. Li, L. Ye, W. Zhao, S. Zhang, S. Mukherjee, H. Ade and J. Hou, Energy-Level Modulation of Small-Molecule Electron Acceptors to Achieve over 12% Efficiency in Polymer Solar Cells, *Advanced Materials*, 2016, **28**, 9423–9429.

24 Y. Lin, F. Zhao, Y. Wu, K. Chen, Y. Xia, G. Li, S. K. K. Prasad, J. Zhu, L. Huo, H. Bin, Z. G. Zhang, X. Guo, M. Zhang, Y. Sun, F. Gao, Z. Wei, W. Ma, C. Wang, J. Hodgkiss, Z. Bo, O.

Inganäs, Y. Li and X. Zhan, Mapping Polymer Donors toward High-Efficiency Fullerene Free Organic Solar Cells, *Advanced Materials*, 2017, **29**, 1604155.

25 L. Meng, Y. Zhang, X. Wan, C. Li, X. Zhang, Y. Wang, X. Ke, Z. Xiao, L. Ding, R. Xia, H. L. Yip, Y. Cao and Y. Chen, Organic and Solution-processed Tandem Solar Cells with 17.3% Efficiency, *Science*, 2018, **361**, 1094–1098.

26 J. Hou, O. Inganäs, R. H. Friend and F. Gao, Organic Solar Cells Based on Non-fullerene Acceptors, *Nature Materials*, 2018, **17**, 119–128.

27 F. Zhang, X. Xu, W. Tang, J. Zhang, Z. Zhuo, J. Wang, J. Wang, Z. Xu and Y. Wang, Recent Development of the Inverted Configuration Organic Solar Cells, *Solar Energy Materials and Solar Cells*, 2011, **95**, 1785–1799.

28 W. L. Leong, G. C. Welch, L. G. Kaake, C. J. Takacs, Y. Sun, G. C. Bazan and A. J. Heeger, Role of Trace Impurities in the Photovoltaic Performance of Solution Processed Small-Molecule Bulk Heterojunction Solar Cells, *Chemical Science*, 2012, **3**, 2103.

29 M. C. Scharber, D. Mühlbacher, M. Koppe, P. Denk, C. Waldauf, A. J. Heeger and C. J. Brabec, Design Rules for Donors in Bulk-Heterojunction Solar Cells—Towards 10 % Energy-Conversion Efficiency, *Advanced Materials*, 2006, **18**, 789–794.

30 U. Scherf, E. Harth, A. Gügel, K. Müllen, U. Lemmer and J. Feldmann, Exciton Diffusion and Dissociation in Conjugated Polymer/Fullerene Blends and Heterostructures, *Physical Review B - Condensed Matter and Materials Physics*, 1999, **59**, 15346–15351.

31 J. J. M. Halls, K. Pichler, R. H. Friend, S. C. Moratti and A. B. Holmes, Exciton Diffusion and Dissociation in a Poly(p-phenylenevinylene)/C60 Heterojunction Photovoltaic Cell, *Applied Physics Letters*, 1996, **68**, 3120–3122.

32 G. Li, R. Zhu and Y. Yang, Polymer solar cells, *Nature Photonics*, 2012, **6**, 153–161.

33 L. Smilowitz, N. S. Sariciftci, R. Wu, C. Gettinger, A. J. Heeger and F. Wudl, Photoexcitation Spectroscopy of Conducting-polymer-C60 Composites: Photoinduced Electron Transfer, *Physical Review B*, 1993, **47**, 13835–13842.

34 L. Meng, Y. Zhang, X. Wan, C. Li, X. Zhang, Y. Wang, X. Ke, Z. Xiao, L. Ding, R. Xia, H. L. Yip, Y. Cao and Y. Chen, Organic and Solution-processed Tandem Solar Cells with 17.3% Efficiency, *Science*, 2018, **361**, 1094–1098.

35 R. D. McCullough, R. D. Lowe, M. Jayaraman and D. L. Anderson, Design, Synthesis, and Control of Conducting Polymer Architectures: Structurally Homogeneous Poly(3-alkylthiophenes), *The Journal of Organic Chemistry*, 1993, **58**, 904–912.

36 H. Mao, B. Xu and S. Holdcroft, Synthesis and Structure-property Relationships of Regioirregular Poly(3-hexylthiophenes), *Macromolecules*, 1993, **26**, 1163–1169.

37 T. A. Chen, X. Wu and R. D. Rieke, Regiocontrolled Synthesis of Poly(3-alkylthiophenes) Mediated by Rieke Zinc: Their Characterization and Solid-State Properties, *Journal of the American Chemical Society*, 1995, **117**, 233–244.

38 T. A. Chen and R. D. Rieke, The First Regioregular Head-to-tail Poly(3-hexylthiophene-2,5-diyl) and a Regiorandom Isopolymer: Nickel versus Palladium Catalysis of 2(5)-bromo-5(2)-(bromozincio)-3-hexylthiophene Polymerization, *Journal of the American Chemical Society*, 1992, **114**, 10087–10088.

39 T. Gruber, C. Kirchner, R. Kling, F. Reuss and A. Waag, ZnMgO Epilayers and ZnO–ZnMgO Quantum Wells for Optoelectronic Applications in the Blue and UV Spectral Region, *Applied Physics Letters*, 2004, **84**, 5359–5361.

40 M. Surin, P. Leclère, R. Lazzaroni, J. D. Yuen, G. Wang, D. Moses, A. J. Heeger, S. Cho and K. Lee, Relationship between the Microscopic Morphology and the Charge Transport Properties in Poly(3-hexylthiophene) Field-effect Transistors, *Journal of Applied Physics*, 2006, **100**, 033712.

41 S. Cho, K. Lee, J. Yuen, G. Wang, D. Moses, A. J. Heeger, M. Surin and R. Lazzaroni, Thermal Annealing-induced Enhancement of the Field-effect Mobility of Regioregular Poly(3-hexylthiophene) Films, *Journal of Applied Physics*, 2006, **100**, 114503.

42 G. Wang, J. Swensen, D. Moses and A. J. Heeger, Increased Mobility from Regioregular Poly(3-hexylthiophene) Field-effect transistors, *Journal of Applied Physics*, 2003, **93**, 6137–6141.

43 H. Sirringhaus, N. Tessler and R. H. Friend, Integrated Optoelectronic Devices Based on Conjugated Polymers, *Science*, 1998, **280**, 1741–1744.

44 D. H. Kim, Y. D. Park, Y. Jang, H. Yang, Y. H. Kim, J. I. Han, D. G. Moon, S. Park, T. Chang, C. Chang, M. Joo, C. Y. Ryu and K. Cho, Enhancement of Field-Effect Mobility Due

to Surface-Mediated Molecular Ordering in Regioregular Polythiophene Thin Film Transistors, *Advanced Functional Materials*, 2005, **15**, 77–82.

45 M. T. Dang, L. Hirsch, G. Wantz and J. D. Wuest, Controlling the Morphology and Performance of Bulk Heterojunctions in Solar Cells. Lessons Learned from the Benchmark Poly(3-hexylthiophene):[6,6]-phenyl- C_{61}-butyric Acid Methyl Ester System, *Chemical Reviews*, 2013, **113**, 3734–3765.

46 G. Li, V. Shrotriya, J. Huang, Y. Yao, T. Moriarty, K. Emery and Y. Yang, High-efficiency Solution Processable Polymer Photovoltaic Cells by Self-organization of Polymer Blends, *Nature Materials*, 2005, **4**, 864–868.

47 C. W. Schlenker and M. E. Thompson, The Molecular Nature of Photovoltage Losses in Organic Solar Cells, *Chemical Communications*, 2011, **47**, 3702.

48 S. Ko, E. T. Hoke, L. Pandey, S. Hong, R. Mondal, C. Risko, Y. Yi, R. Noriega, M. D. McGehee, J. L. Brédas, A. Salleo and Z. Bao, Controlled Conjugated Backbone Twisting for an Increased Open-circuit Voltage While Having a High Short-circuit Current in Poly(hexylthiophene) Derivatives, *Journal of the American Chemical Society*, 2012, **134**, 5222–5232.

49 M. Zhang, X. Guo, W. Ma, H. Ade and J. Hou, A Polythiophene Derivative with Superior Properties for Practical Application in Polymer Solar Cells, *Advanced Materials*, 2014, **26**, 5880–5885.

50 Y. Li, G. Zhang, G. Yang, Y. Guo, C. Di, X. Chen, Z. Liu, H. Liu, Z. Xu, W. Xu, H. Fu and D. Zhang, Extended π-conjugated Molecules Derived from Naphthalene Diimides toward Organic Emissive and Semiconducting Materials, *Journal of Organic Chemistry*, 2013, **78**, 2926–2934.

51 Y. Zhao, Y. Guo and Y. Liu, 25th Anniversary Article: Recent Advances in n-type and Ambipolar Organic Field-effect Transistors, *Advanced Materials*, 2013, **25**, 5372–5391.

52 J. Mei, Y. Diao, A. L. Appleton, L. Fang and Z. Bao, Integrated Materials Design of Organic Semiconductors for Field-effect Transistors, *Journal of the American Chemical Society*, 2013, **135**, 6724–6746.

53 H. Usta, A. Facchetti and T. J. Marks, N-channel Semiconductor Materials Design for Organic Complementary Circuits, *Accounts of Chemical Research*, 2011, **44**, 501–510.

54 X. Zhan, A. Facchetti, S. Barlow, T. J. Marks, M. A. Ratner, M. R. Wasielewski and S. R. Marder, Rylene and Related Diimides for Organic Electronics, *Advanced Materials*, 2011, **23**, 268–284.

55 G. Shen, X. Li, X. Wu, Y. Wang, H. Shan, J. Xu, X. Liu, Z. xiang Xu, F. Chen and Z. K. Chen, Naphthalene Tetracarboxylic Diimide (NDI)-based Polymer Solar Cells Processed by Non-halogenated Solvents, *Organic Electronics: physics, materials, applications*, 2017, **46**, 203–210.

56 Y. Li, P. Sonar, L. Murphy and W. Hong, High Mobility Diketopyrrolopyrrole (DPP)-based Organic Semiconductor Materials for Organic Thin Film Transistors and Photovoltaics, *Energy & Environmental Science*, 2013, **6**, 1684.

57 R. Stalder, J. Mei, K. R. Graham, L. A. Estrada and J. R. Reynolds, Isoindigo, A Versatile Electron-deficient Unit for High-performance Organic Electronics, *Chemistry of Materials*, 2014, **26**, 664–678.

58 C. B. Nielsen, M. Turbiez and I. McCulloch, Recent Advances in the Development of Semiconducting DPP-containing Polymers for Transistor Applications, *Advanced Materials*, 2013, **25**, 1859–1880.

59 L. Lu, T. Zheng, Q. Wu, A. M. Schneider, D. Zhao and L. Yu, Recent Advances in Bulk Heterojunction Polymer Solar Cells, *Chemical Reviews*, 2015, **115**, 12666–12731.

60 J. M. Szarko, J. Guo, Y. Liang, B. Lee, B. S. Rolczynski, J. Strzalka, T. Xu, S. Loser, T. J. Marks, L. Yu and L. X. Chen, When Function Follows Form: Effects of Donor Copolymer Side Chains on Film Morphology and BHJ Solar Cell Performance, *Advanced Materials*, 2010, **22**, 5468–5472.

61 Z. Liu, G. Zhang, Z. Cai, X. Chen, H. Luo, Y. Li, J. Wang and D. Zhang, New Organic Semiconductors with Imide/amide-containing Molecular Systems, *Advanced Materials*, 2014, **26**, 6965–6977.

62 Z. Fei, P. Boufflet, S. Wood, J. Wade, J. Moriarty, E. Gann, E. L. Ratcliff, C. R. Mcneill, H. Sirringhaus, J. S. Kim and M. Heeney, Influence of Backbone Fluorination in Regioregular

Poly(3-alkyl-4-fluoro)thiophenes, *Journal of the American Chemical Society*, 2015, **137**, 6866–6879.

63 F. Liu, Z. Zhou, C. Zhang, J. Zhang, Q. Hu, T. Vergote, F. Liu, T. P. Russell and X. Zhu, Efficient Semitransparent Solar Cells with High NIR Responsiveness Enabled by a Small-Bandgap Electron Acceptor, *Advanced Materials*, 2017, **29**, 1606574.

64 L. Leonat, G. Sbarcea and I. V. Branzoi, Cyclic Voltammetry for Energy Levels Estimation of Organic Materials, *U.P.B Sci. Bull, Series B*, 2013, **75**, 111–118.

65 J. Hou, T. L. Chen, S. Zhang, L. Huo, S. Sista and Y. Yang, An Easy and Effective Method to Modulate Molecular Energy Level of Poly(3-alkylthiophene) for High-Voc Polymer Solar Cells, *Macromolecules*, 2009, **42**, 9217–9219.

66 D. Chen, A. Nakahara, D. Wei, D. Nordlund and T. P. Russell, P3HT/PCBM Bulk Heterojunction Organic Photovoltaics: Correlating Efficiency and Morphology, *Nano Letters*, 2011, **11**, 561–567.

67 Y. Qin, M. A. Uddin, Y. Chen, B. Jang, K. Zhao, Z. Zheng, R. Yu, T. J. Shin, H. Y. Woo and J. Hou, Highly Efficient Fullerene-Free Polymer Solar Cells Fabricated with Polythiophene Derivative, *Advanced Materials*, 2016, **28**, 9416–9422.

68 Y. Liang, Z. Xu, J. Xia, S. T. Tsai, Y. Wu, G. Li, C. Ray and L. Yu, For the Bright Future-Bulk Heterojunction Polymer Solar Cells with Power Conversion Efficiency of 7.4%, *Advanced Materials*, 2010, **22**, E135–E138.

69 J. H. Park, J. I. Park, D. H. Kim, J. H. Kim, J. S. Kim, J. H. Lee, M. Sim, S. Y. Lee and K. Cho, Enhanced Device Performance of Organic Solar Cells via Reduction of the Crystallinity in the Donor Polymer, *Journal of Materials Chemistry*, 2010, **20**, 5860.

70 Z. Zheng, Q. Hu, S. Zhang, D. Zhang, J. Wang, S. Xie, R. Wang, Y. Qin, W. Li, L. Hong, N. Liang, F. Liu, Y. Zhang, Z. Wei, Z. Tang, T. P. Russell, J. Hou and H. Zhou, A Highly Efficient Non-Fullerene Organic Solar Cell with a Fill Factor over 0.80 Enabled by a Fine-Tuned Hole-Transporting Layer, *Advanced Materials*, 2018, **30**, 1801801.

71 X. Song, N. Gasparini, M. M. Nahid, H. Chen, S. M. Macphee, W. Zhang, V. Norman, C. Zhu, D. Bryant, H. Ade, I. McCulloch and D. Baran, A Highly Crystalline Fused-Ring n-Type

Small Molecule for Non-Fullerene Acceptor Based Organic Solar Cells and Field-Effect Transistors, *Advanced Functional Materials*, 2018, **28**, 1802895.

72 J. Zhu, Y. Xiao, J. Wang, K. Liu, H. Jiang, Y. Lin, X. Lu and X. Zhan, Alkoxy-Induced Near-Infrared Sensitive Electron Acceptor for High-Performance Organic Solar Cells, *Chemistry of Materials*, 2018, **30**, 4150–4156.

73 B. Dandrade, S. Datta, S. Forrest, P. Djurovich, E. Polikarpove and M. Thompson, Relationship Between the Ionization and Oxidation Potentials of Molecular Organic Semiconductors, *Organic Electronics*, 2005, **6**, 11–20.

74 G. Nagarjuna and D. Venkataraman, Strategies for Controlling the Active Layer Morphologies in OPVs, *Journal of Polymer Science Part B: Polymer Physics*, 2012, **50**, 1045–1056.

75 T. L. Benanti and D. Venkataraman, Organic Solar Cells: An Overview Focusing on Active Layer Morphology, *Photosynthesis Research*, 2006, **87**, 73–81.

76 S. S. van Bavel and J. Loos, in *Green Energy and Technology*, 2011, pp. 227–249.

77 X. Yang and J. Loos, Toward High-Performance Polymer Solar Cells: The Importance of Morphology Control, *Macromolecules*, 2007, **40**, 1353–1362.

78 B. C. Thompson and J. M. J. Fréchet, Polymer–Fullerene Composite Solar Cells, *Angewandte Chemie International Edition*, 2008, **47**, 58–77.

79 Z. G. Zhang and Y. Li, Side-chain Engineering of High-efficiency Conjugated Polymer Photovoltaic Materials, *Science China Chemistry*, 2015, **58**, 192–209.

80 S. J. Kang, S. Ahn, J. B. Kim, C. Schenck, A. M. Hiszpanski, S. Oh, T. Schiros, Y.-L. Loo and C. Nuckolls, Using Self-Organization To Control Morphology in Molecular Photovoltaics, *Journal of the American Chemical Society*, 2013, **135**, 2207–2212.

81 A. C. Mayer, M. F. Toney, S. R. Scully, J. Rivnay, C. J. Brabec, M. Scharber, M. Koppe, M. Heeney, I. McCulloch and M. D. McGehee, Bimolecular Crystals of Fullerenes in Conjugated Polymers and the Implications of Molecular Mixing for Solar Cells, *Advanced Functional Materials*, 2009, **19**, 1173–1179.

82 R. D. Kennedy, A. L. Ayzner, D. D. Wanger, C. T. Day, M. Halim, S. I. Khan, S. H. Tolbert, B. J. Schwartz and Y. Rubin, Self-Assembling Fullerenes for Improved Bulk-Heterojunction Photovoltaic Devices, *Journal of the American Chemical Society*, 2008, **130**, 17290–17292.

83 W. W. H. Wong, C. Q. Ma, W. Pisula, A. Mavrinskiy, X. Feng, H. Seyler, D. J. Jones, K. Müllen, P. Bäuerle and A. B. Holmes, Fluorenyl Hexa-peri-hexabenzocoronene-Dendritic Oligothiophene Hybrid Materials: Synthesis, Photophysical Properties, Self-Association Behaviour and Device Performance, *Chemistry - A European Journal*, 2011, **17**, 5549–5560.

84 W. W. H. Wong, C. Q. Ma, W. Pisula, C. Yan, X. Feng, D. J. Jones, K. Müllen, R. A. J. Janssen, P. Bäuerle and A. B. Holmes, Self-Assembling Thiophene Dendrimers with a Hexa-peri -hexabenzocoronene Core−Synthesis, Characterization and Performance in Bulk Heterojunction Solar Cells, *Chemistry of Materials*, 2010, **22**, 457–466.

85 R. J. Kumar, J. M. MacDonald, T. B. Singh, L. J. Waddington and A. B. Holmes, Hierarchical Self-Assembly of Semiconductor Functionalized Peptide α-Helices and Optoelectronic Properties, *Journal of the American Chemical Society*, 2011, **133**, 8564–8573.

86 J. Emsley, Very Strong Hydrogen Bonding, *Chemical Society Reviews*, 1980, **9**, 91.

87 L. J. Prins, D. N. Reinhoudt and P. Timmerman, Noncovalent Synthesis Using Hydrogen Bonding, *Angewandte Chemie - International Edition*, 2001, **40**, 2382–2426.

88 A. P. H. J. Schenning, J. V. Herrikhuyzen, P. Jonkheijm, Z. Chen, F. Würthner and E. W. Meijer, Photoinduced Electron Transfer in Hydrogen-bonded Oligo(p-phenylene vinylene)-Perylene Bisimide Chiral Assemblies, *Journal of the American Chemical Society*, 2002, **124**, 10252–10253.

89 E. D. Głowacki, M. Irimia-Vladu, S. Bauer and N. S. Sariciftci, Hydrogen-bonds in Molecular Solids-from Biological Systems to Organic Electronics, *Journal of Materials Chemistry B*, 2013, **1**, 3742–3753.

90 J. Dhar, D. P. Karothu and S. Patil, Herringbone to Cofacial Solid State Packing via H-bonding in Diketopyrrolopyrrole (DPP) Based Molecular Crystals: Influence on Charge Transport, *Chemical Communications*, 2015, **51**, 97–100.

91 H. Yanagisawa, J. Mizuguchi, S. Aramaki and Y. Sakai, Organic Field-Effect Transistor Devices Based on Latent Pigments of Unsubstituted Diketopyrrolopyrrole or Quinacridone, *Japanese Journal of Applied Physics*, 2008, **47**, 4728–4731.

92 E. D. Głowacki, H. Coskun, M. A. Blood-Forsythe, U. Monkowius, L. Leonat, M. Grzybowski, D. Gryko, M. S. White, A. Aspuru-Guzik and N. S. Sariciftci, Hydrogen-bonded

Diketopyrrolopyrrole (DPP) Pigments as Organic Semiconductors, *Organic Electronics*, 2014, **15**, 3521–3528.

93 S. L. Hsu, C. M. Chen, Y. H. Cheng and K. H. Wei, New Carbazole-based Conjugated Polymers Containing Pyridylvinyl Thiophene Units for Polymer Solar Cell Applications: Morphological Stabilization through Hydrogen Bonding, *Journal of Polymer Science Part A: Polymer Chemistry*, 2011, **49**, 603–611.

94 D. Sahu, H. Padhy, D. Patra, D. Kekuda, C. W. Chu, I. H. Chiang and H. C. Lin, Synthesis and Application of H-Bonded Cross-linking Polymers Containing a Conjugated Pyridyl H-Acceptor Side-chain Polymer and Various Carbazole-based H-Donor Dyes Bearing Symmetrical Cyanoacrylic Acids for Organic Solar Cells, *Polymer*, 2010, **51**, 6182–6192.

95 D. Patra, M. Ramesh, D. Sahu, H. Padhy, C. W. Chu, K.-H. Wei and H. C. Lin, Enhancement of Photovoltaic Properties in Supramolecular Polymer Networks Featuring a Solar Cell Main-chain Polymer H-bonded With Conjugated Cross-linkers, *Polymer*, 2012, **53**, 1219–1228.

96 C. Liu, Y. Li, C. Li, W. Li, C. Zhou, H. Liu, Z. Bo and Y. Li, New Methanofullerenes Containing Amide as Electron Acceptor for Construction Photovoltaic Devices, *The Journal of Physical Chemistry C*, 2009, **113**, 21970–21975.

97 Y. Lin, Q. Wei, G. Qian, L. Yao and J. J. Watkins, Morphology Control in TiO_2 Nanorod/Polythiophene Composites for Bulk Heterojunction Solar Cells Using Hydrogen Bonding, *Macromolecules*, 2012, **45**, 8665–8673.

98 M. Irimia-Vladu, E. D. Głowacki, G. Voss, S. Bauer and N. S. Sariciftci, Green and Biodegradable Electronics, *Materials Today*, 2012, **15**, 340–346.

99 G. R. Desiraju, Reflections on the Hydrogen Bond in Crystal Engineering, *Crystal Growth & Design*, 2011, **11**, 896–898.

100 C. B. Aakeröy and K. R. Seddon, The Hydrogen Bond and Crystal Engineering, *Chem. Soc. Rev.*, 1993, **22**, 397–407.

101 M. Mautner, The Ionic Hydrogen Bond, *Chemical Reviews*, 2005, **105**, 213–284.

102 G. R. Desiraju, C-H ··· O Hydrogen Bonding and the Deliberate Design of Organic Crystal Structures, *Molecular Crystals and Liquid Crystals Science and Technology. Section A. Molecular Crystals and Liquid Crystals*, 1992, **211**, 63–74.

103 Z. Xiao, K. Sun, J. Subbiah, S. Ji, D. J. Jones and W. W. H. Wong, Hydrogen Bonding in Bulk Heterojunction Solar Cells: A Case Study, *Scientific Reports*, 2015, **4**, 5701.

104 Y. J. Kim, W. Jang, S. Ahn, C. E. Park and D. H. Wang, Dramatically Enhanced Performances and Ideally Controlled Nano-morphology via Co-solvent Processing in Low Bandgap Polymer Solar Cells, *Organic Electronics*, 2016, **34**, 42–49.

105 T. H. Lee, S. Y. Park, B. Walker, S. J. Ko, J. Heo, H. Y. Woo, H. Choi and J. Y. Kim, A Universal Processing Additive for High-Performance Polymer Solar Cells, *RSC Advances*, 2017, **7**, 7476–7482.

106 H. Zhang, S. Li, B. Xu, H. Yao, B. Yang and J. Hou, Fullerene-free Polymer Solar Cell Based on a Polythiophene Derivative with an Unprecedented Energy Loss of Less Than 0.5 eV, *Journal of Materials Chemistry A*, 2016, **4**, 18043–18049.

107 T. Aytun, L. Barreda, A. Ruiz-Carretero, J. A. Lehrman and S. I. Stupp, Improving Solar Cell Efficiency Through Hydrogen Bonding: A Method for Tuning Active Layer Morphology, *Chemistry of Materials*, 2015, **27**, 1201–1209.

Appendix A

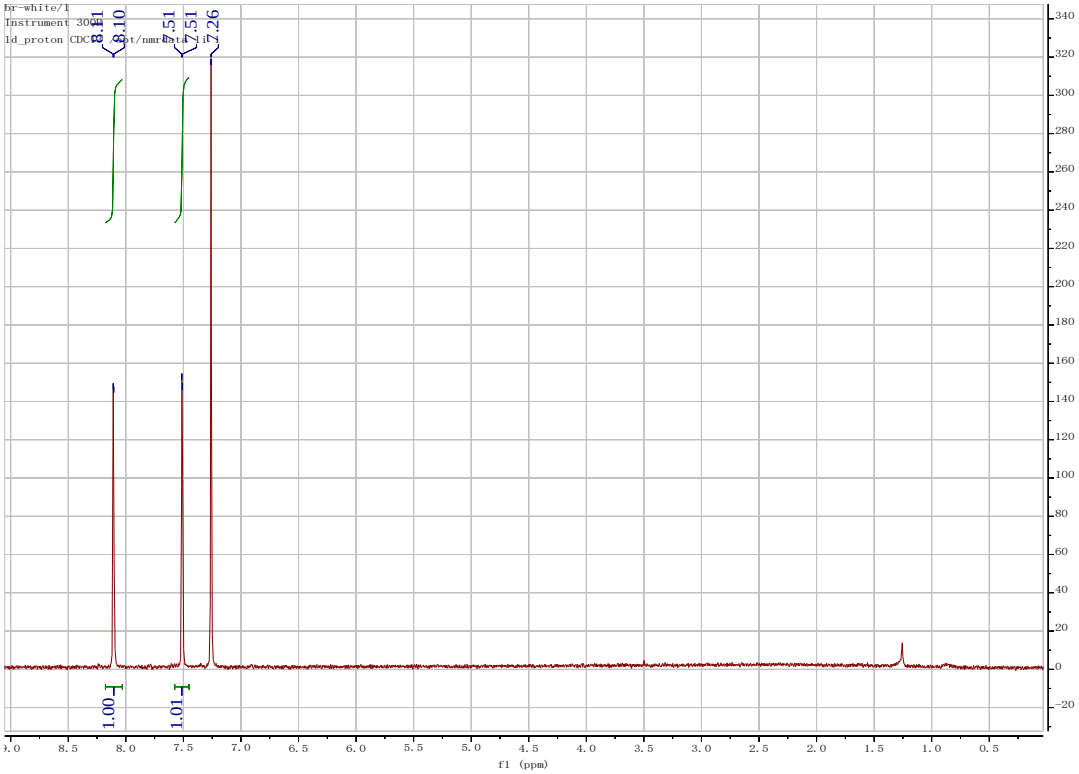

Appendix A- 1 300 MHz ^{1}H NMR spectrum for 5-bromothiophene-3-carboxylic acid in chloroform-*d.*

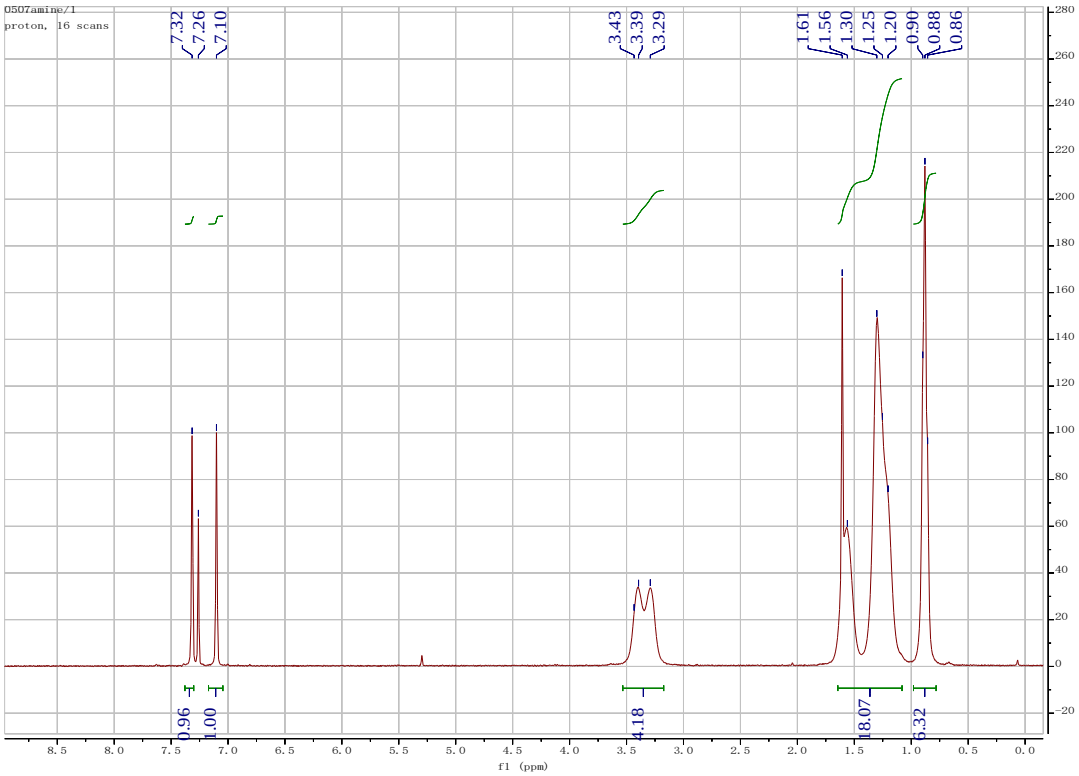

Appendix A- 2 300 MHz ^{1}H NMR spectrum for N, N-dihexyl-3-thiophenecarbamide in chloroform-*d*.

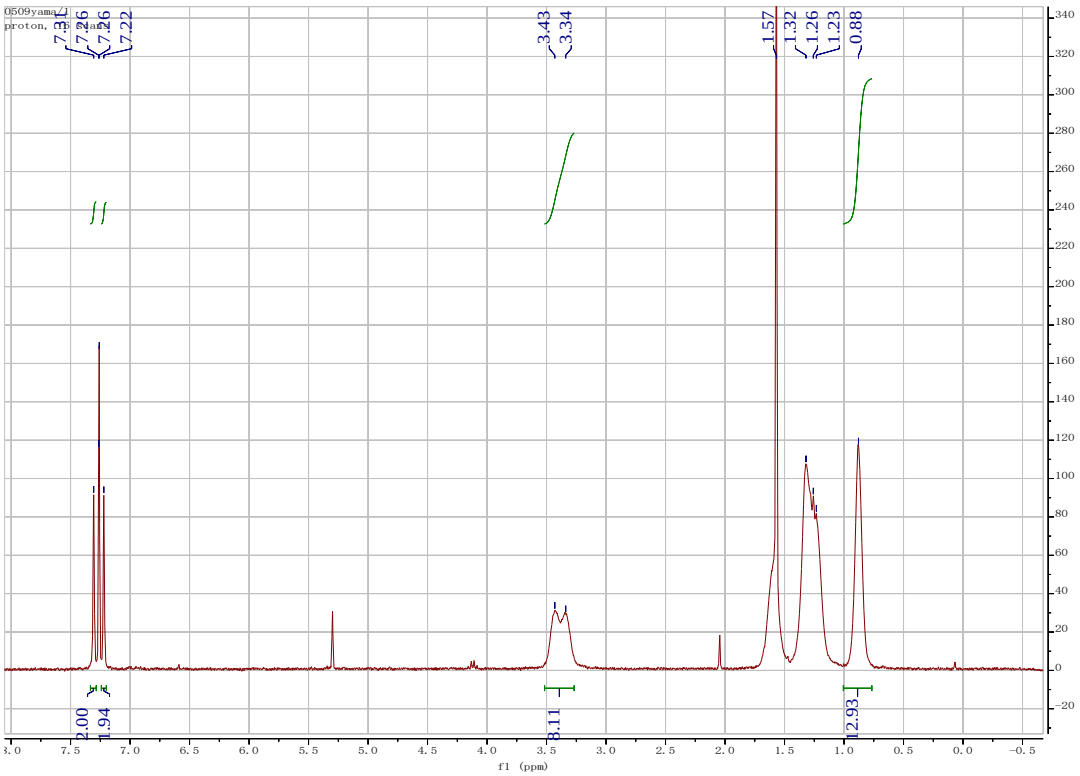

Appendix A- 3 300 MHz ^{1}H NMR spectrum for N^4, N^4, $N^{4'}$, $N^{4'}$-tetrahexyl-[2,2'-bithiophene]-4,4'-dicarboxamide in chloroform-*d*.

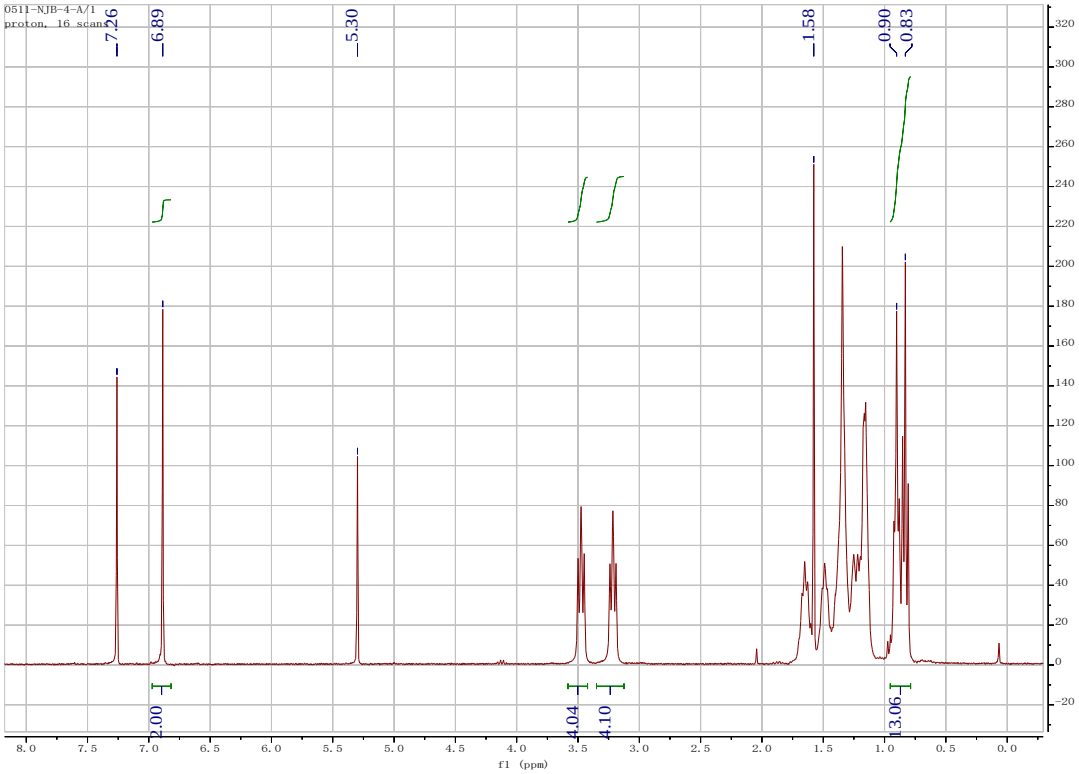

Appendix A- 4 300 MHz ^{1}H NMR spectrum for 5,5'-dibromo-N^{4}, N^{4}, $N^{4'}$, $N^{4'}$-tetrahexyl-[2,2'-bithiophene]-4,4'-dicarboxamide in chloroform-*d*.

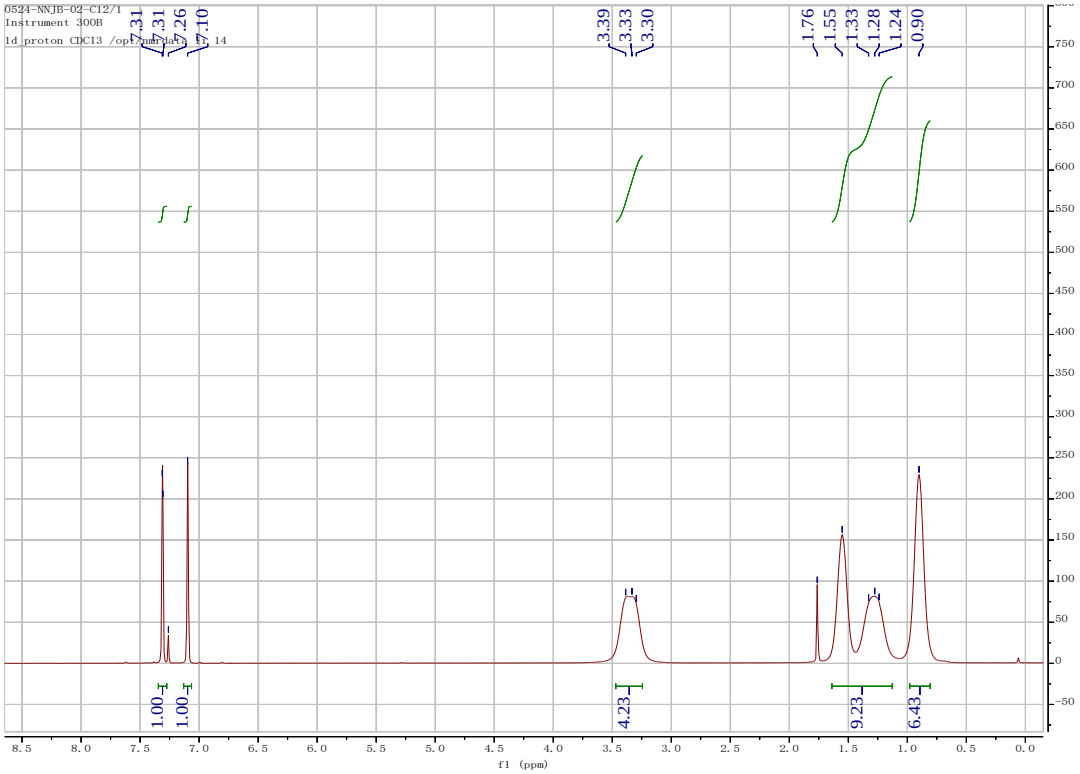

Appendix A- 5 300 MHz ^{1}H NMR spectrum for 5-bromo-N, N-dibutylthiophene-3-carboxamide in chloroform-*d*.

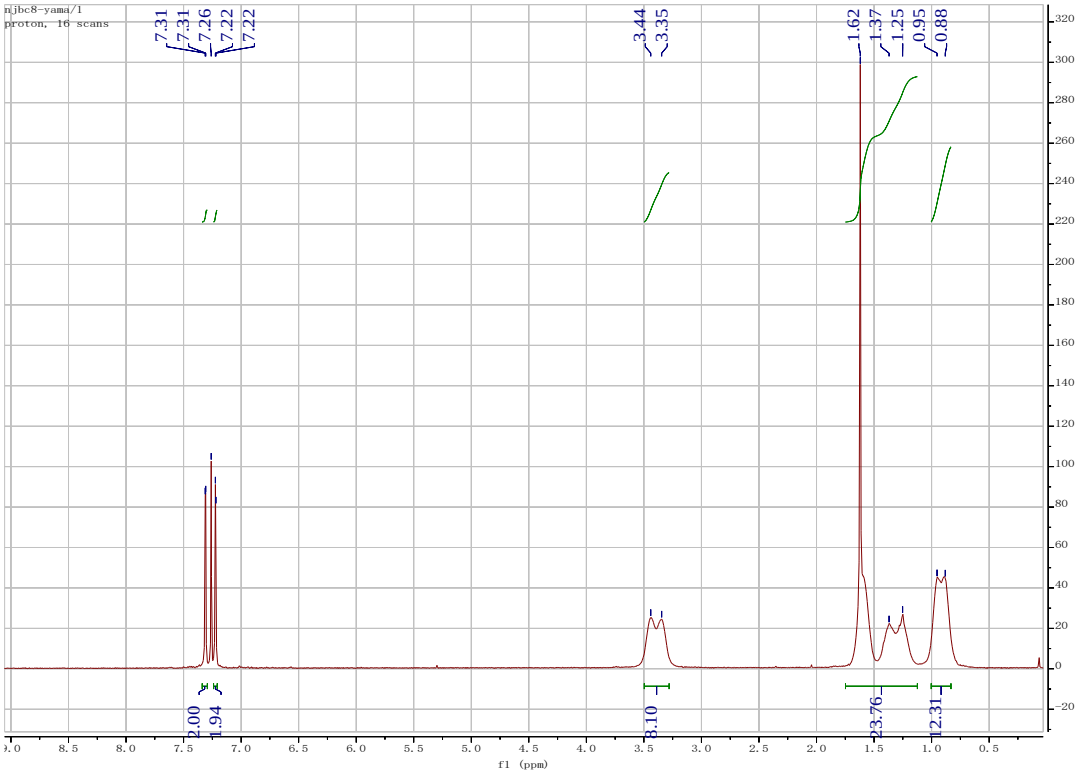

Appendix A- 6 300 MHz ^{1}H NMR spectrum for N^{4}, N^{4}, $N^{4'}$, $N^{4'}$-tetrabutyl-[2,2'-bithiophene]-4,4'-dicarboxamide in chloroform-*d*.

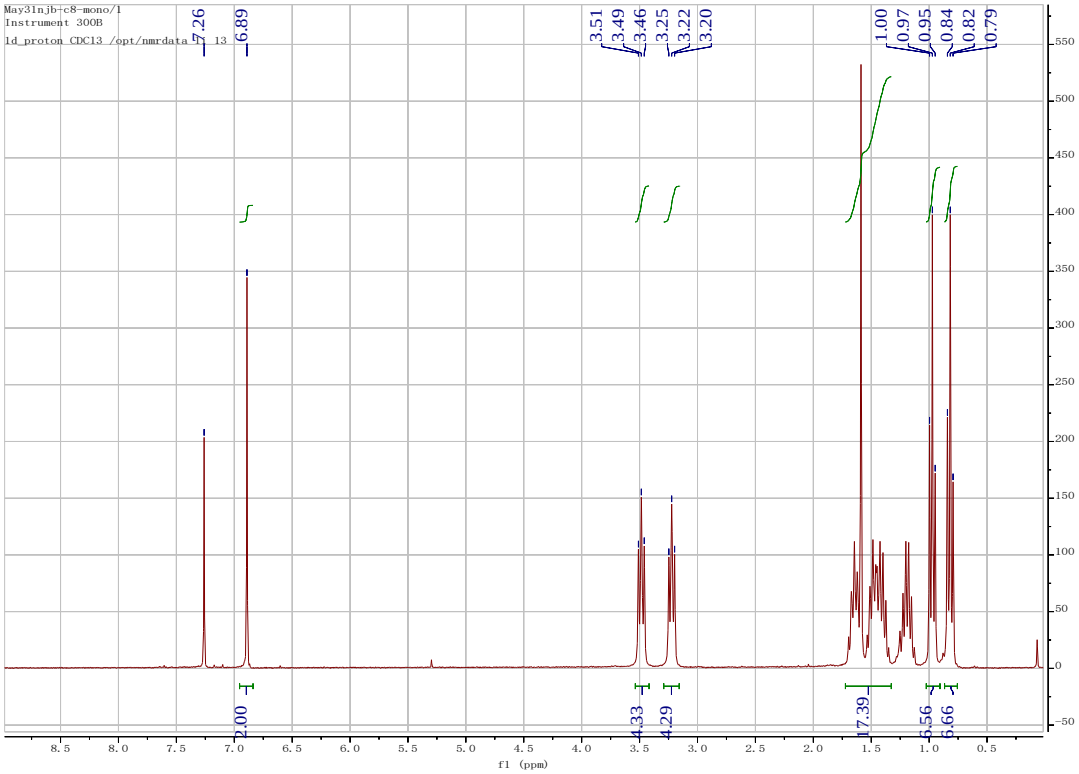

Appendix A- 7 300 MHz ^{1}H NMR spectrum for 5,5'-dibromo-N^4, N^4, $N^{4'}$, $N^{4'}$-tetrabutyl-[2,2'-bithiophene]-4,4'-dicarboxamide in chloroform-*d*.

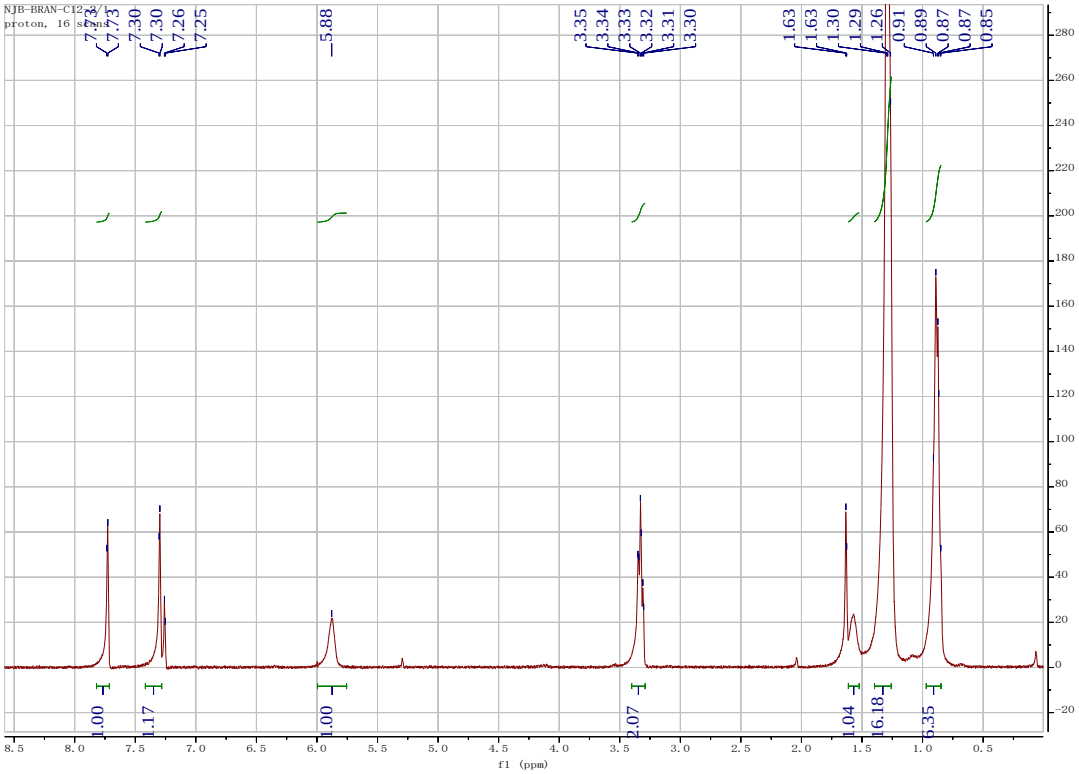

Appendix A- 8 300 MHz ^{1}H NMR spectrum for 5-bromo-N-(2-butyloctyl)-thiophene-3-carboxamide in chloroform-*d*.

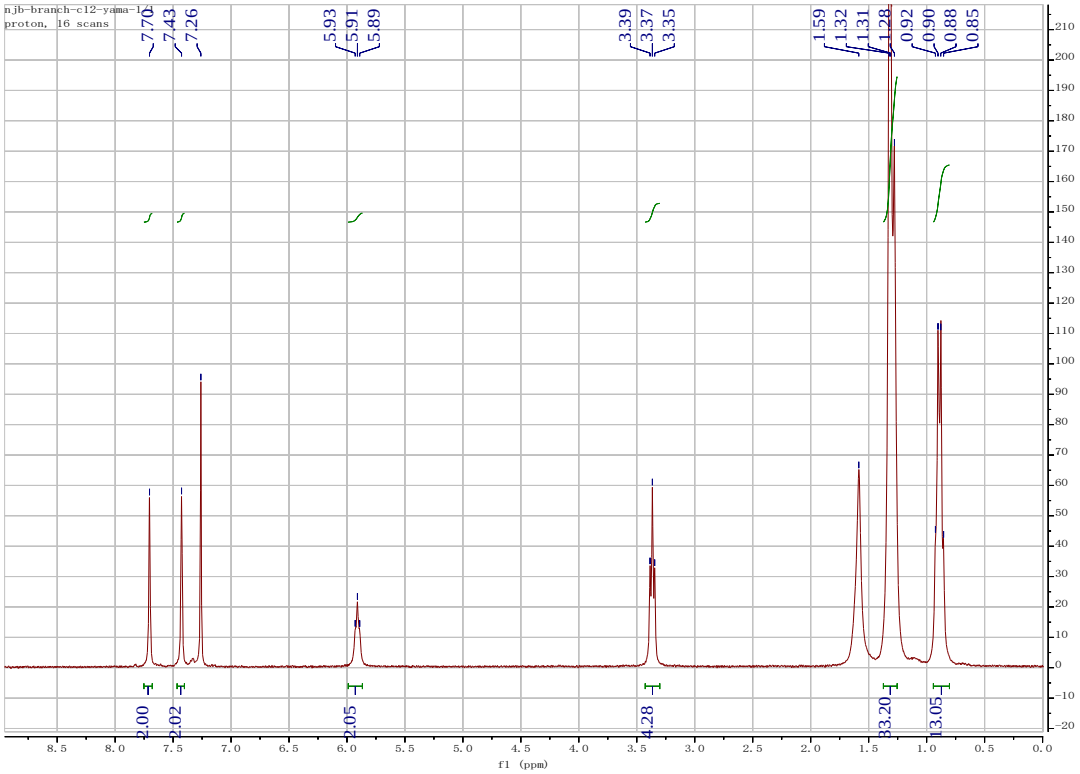

Appendix A- 9 300 MHz ^{1}H NMR spectrum for N^{4}, $N^{4'}$-bis(2-butyloctyl)-[2,2'-bithiophene]-4,4'-dicarboxamide in chloroform-*d*.

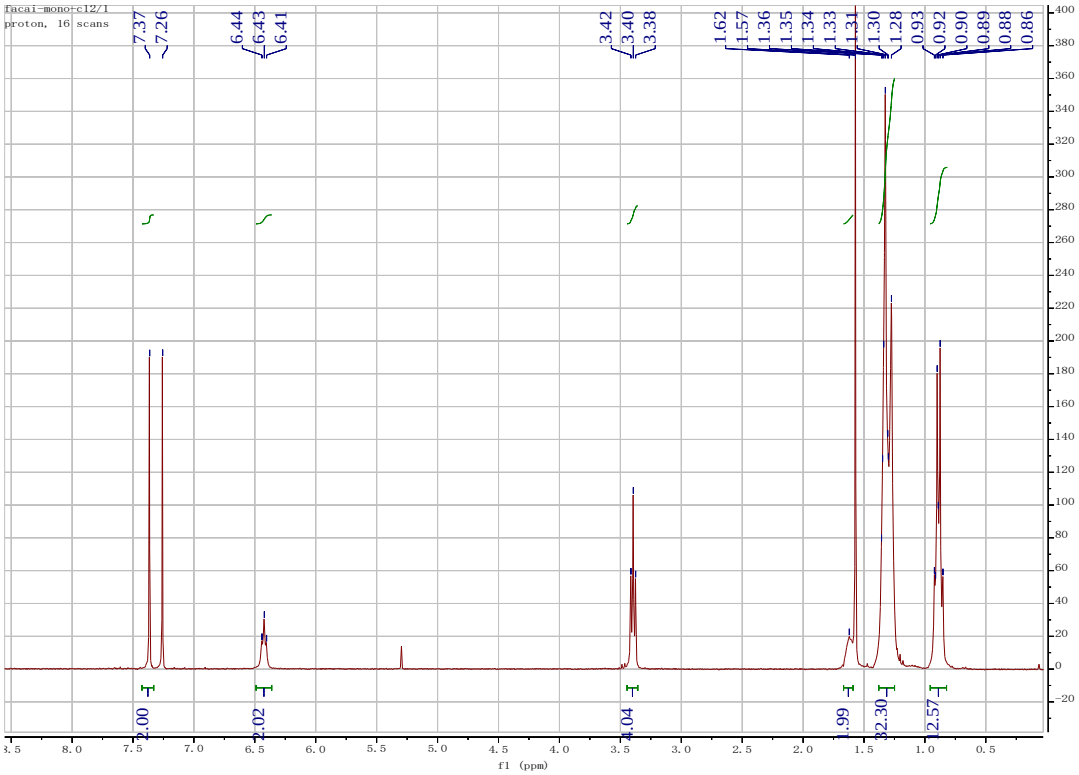

Appendix A- 10 300 MHz ^{1}H NMR spectrum for 5,5'-dibromo-N^{4}, N$^{4'}$-bis(2-butyloctyl)-[2,2'-bithiophene]-4,4'-dicarboxamide in chloroform-*d*.

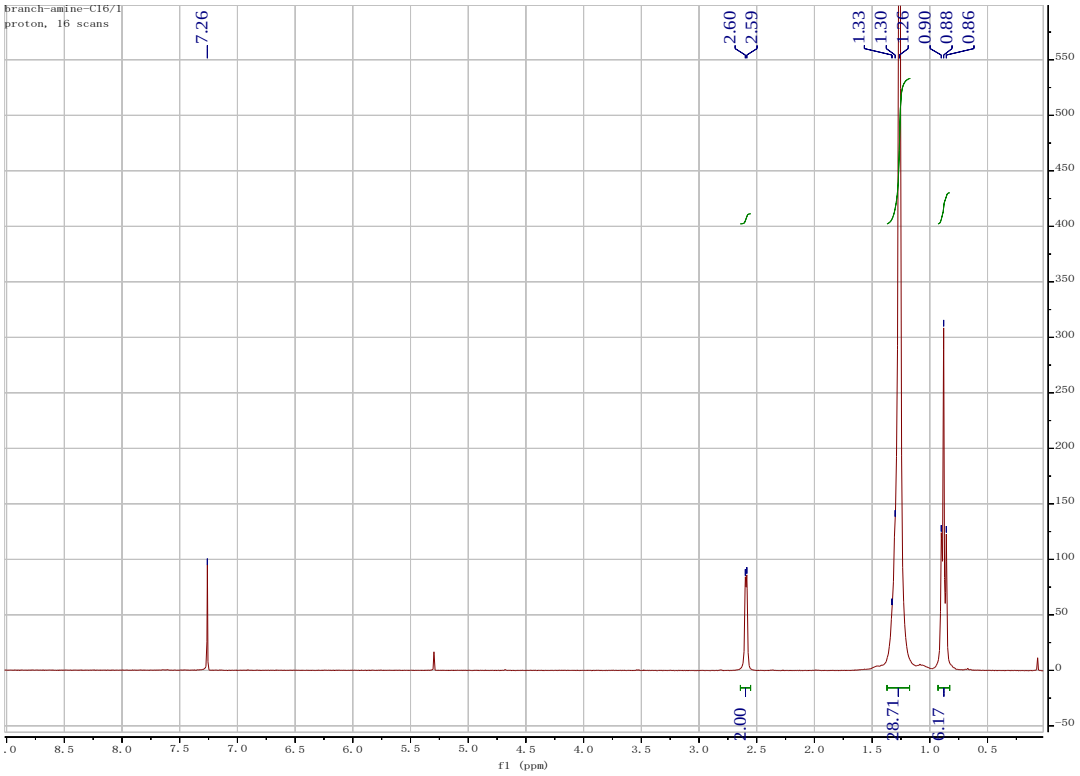

Appendix A- 11 300 MHz ^{1}H NMR spectrum for 2-hexyldecan-1-amine in chloroform-*d*.

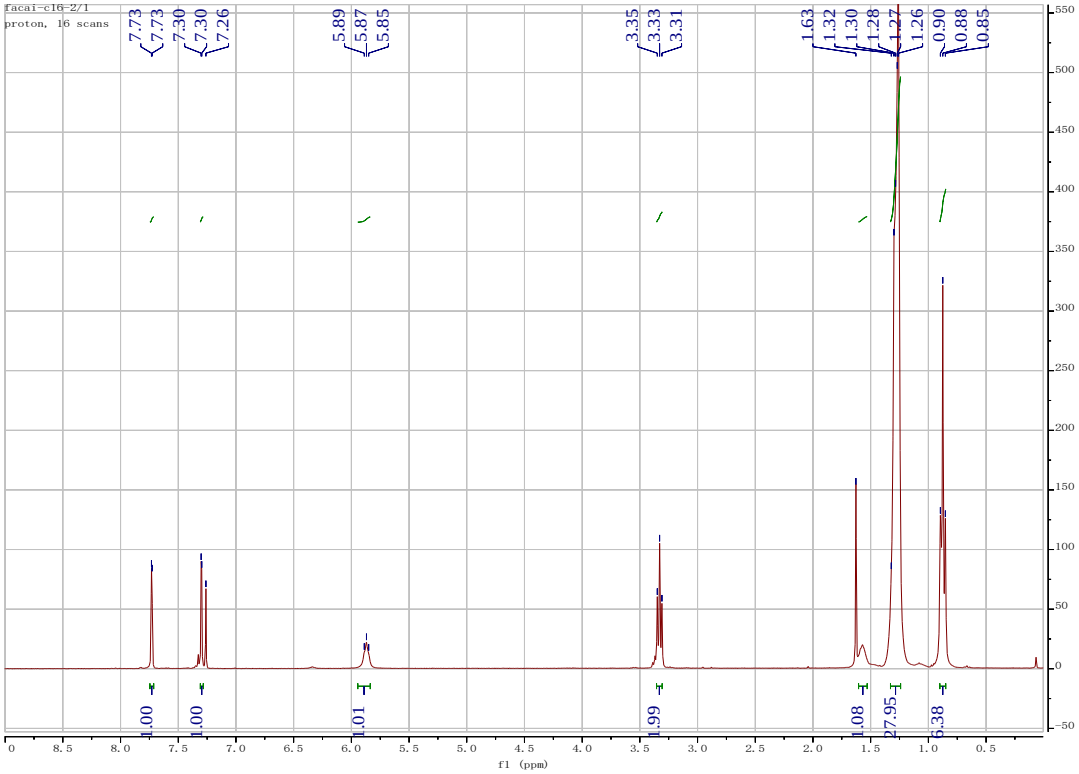

Appendix A- 12 300 MHz ^{1}H NMR spectrum for 5-bromo-N-(2-hexyldecyl)-thiophene-3-carboxamide in chloroform-*d*.

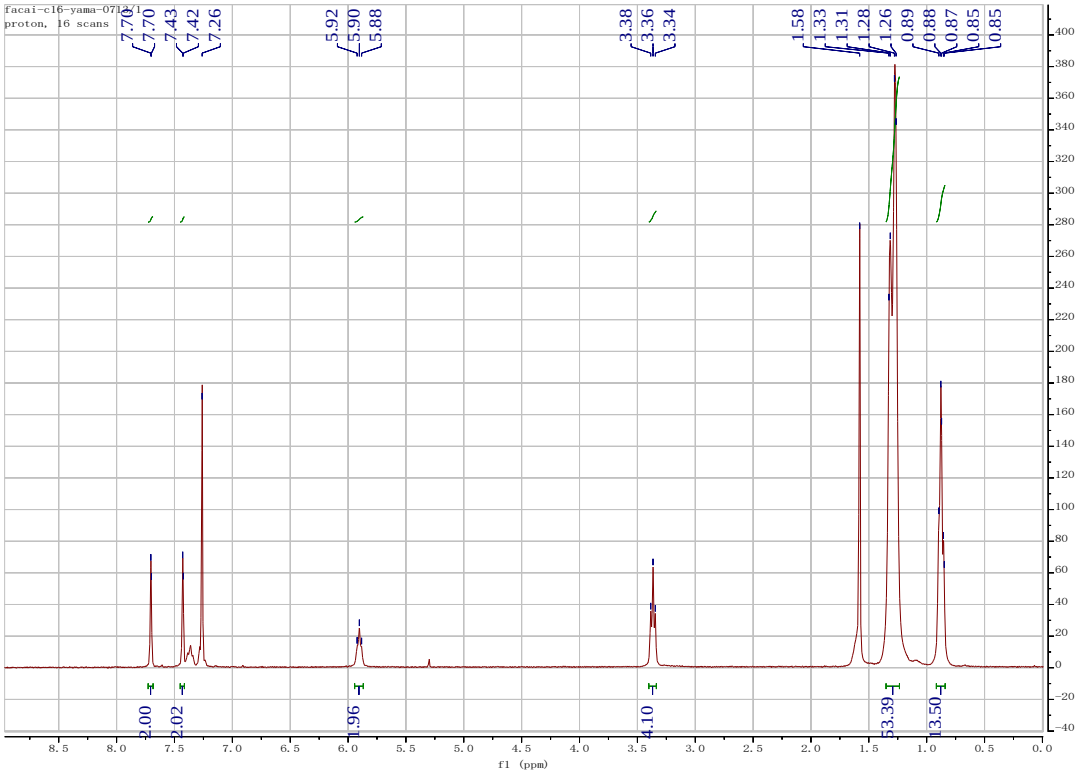

Appendix A- 13 300 MHz ^{1}H NMR spectrum for N^{4}, $N^{4'}$-bis(2-hexyldecyl)-[2,2'-bithiophene]-4,4'-dicarboxamide in chloroform-*d*.

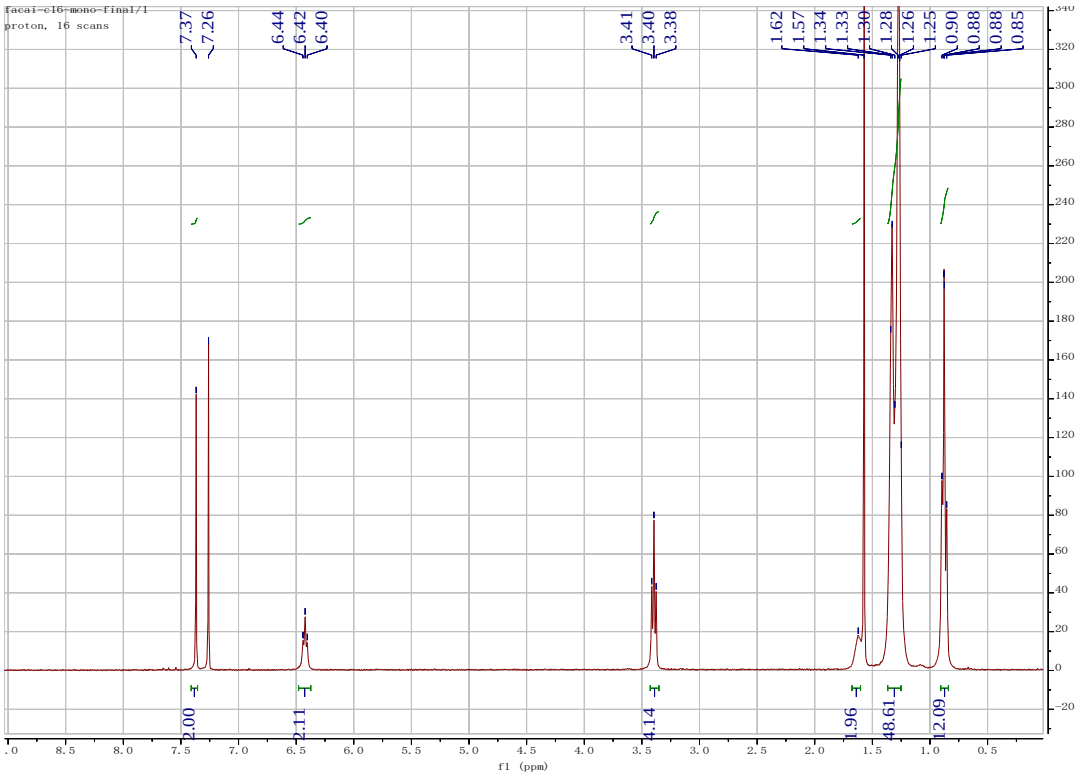

Appendix A- 14 300 MHz ^{1}H NMR spectrum for 5,5'-dibromo-N^{4}, N$^{4'}$-bis(2-hexyldecyl)-[2,2'-bithiophene]-4,4'-dicarboxamide in chloroform-*d*.

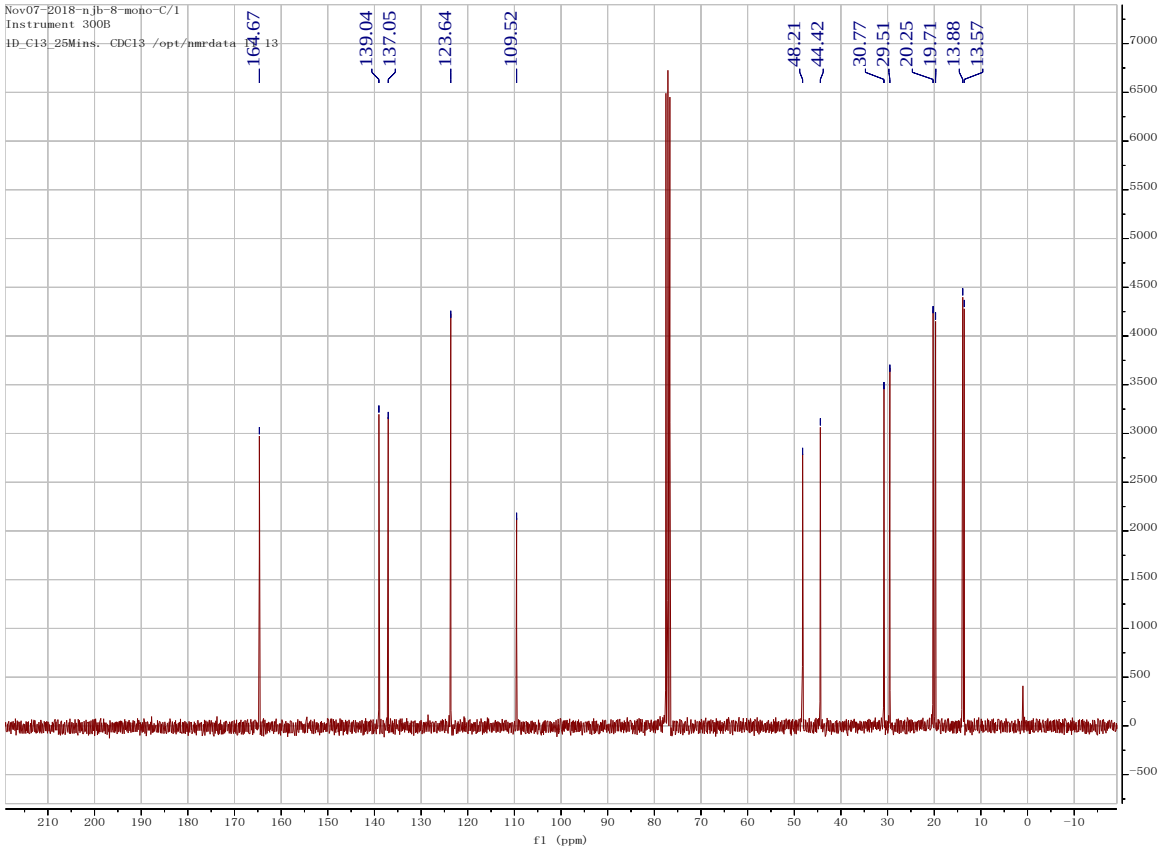

Appendix A- 15 75 MHz ^{13}C NMR spectrum for 5,5'-dibromo-N^4, N^4, N$^{4'}$, N$^{4'}$-tetrahexyl-[2,2'-bithiophene]-4,4'-dicarboxamide in chloroform-*d*.

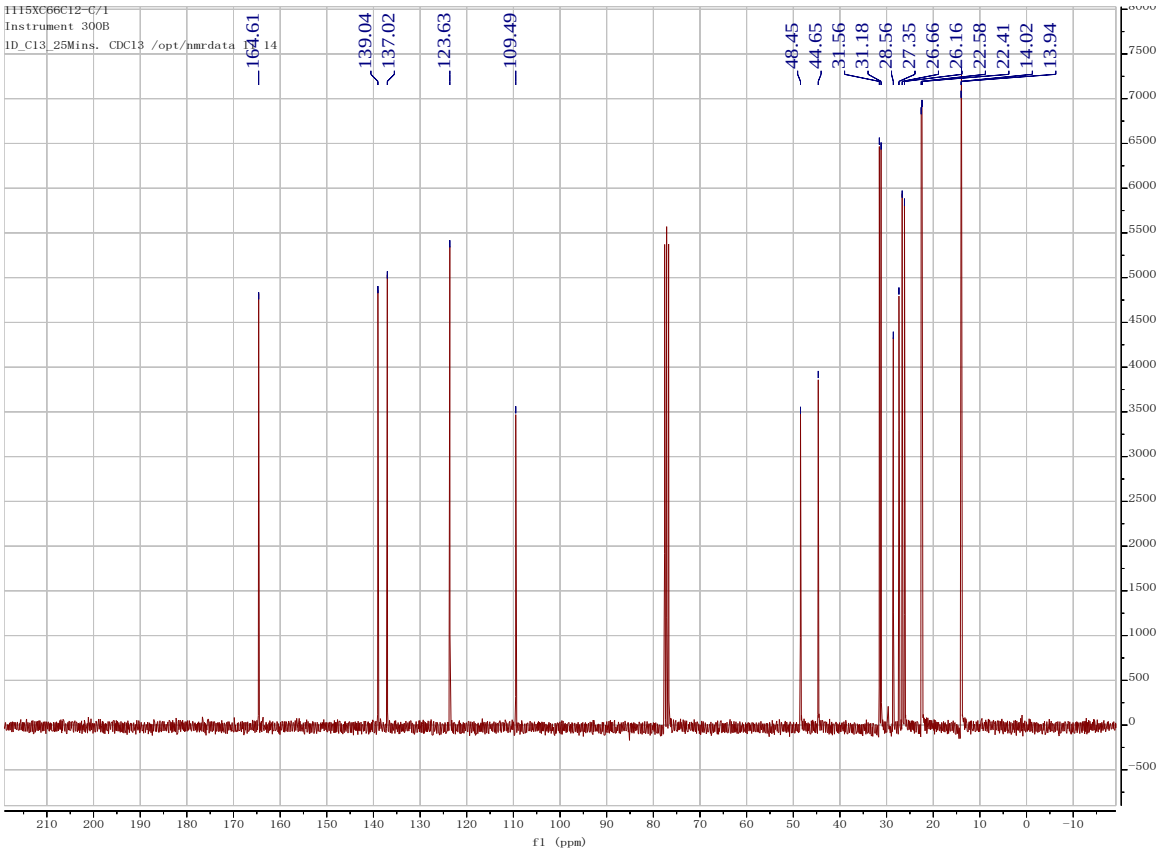

Appendix A- 16 75 MHz ^{13}C NMR spectrum for 5,5'-dibromo-N^4, N^4, N$^{4'}$, N$^{4'}$-tetrabutyl-[2,2'-bithiophene]-4,4'-dicarboxamide in chloroform-*d*.

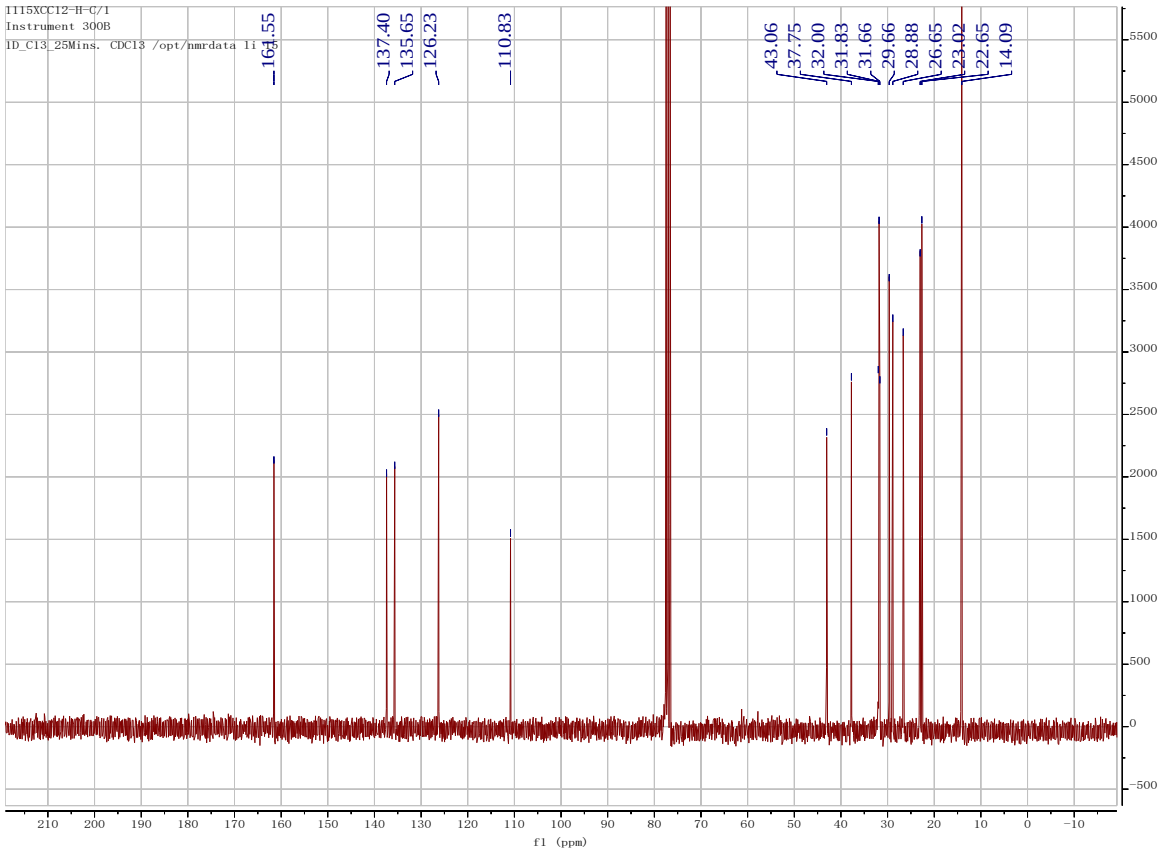

Appendix A- 17 75 MHz ^{13}C NMR spectrum for 5,5'-dibromo-N^4, N$^{4'}$-bis(2-butyloctyl)-[2,2'-bithiophene]-4,4'-dicarboxamide in chloroform-*d*.

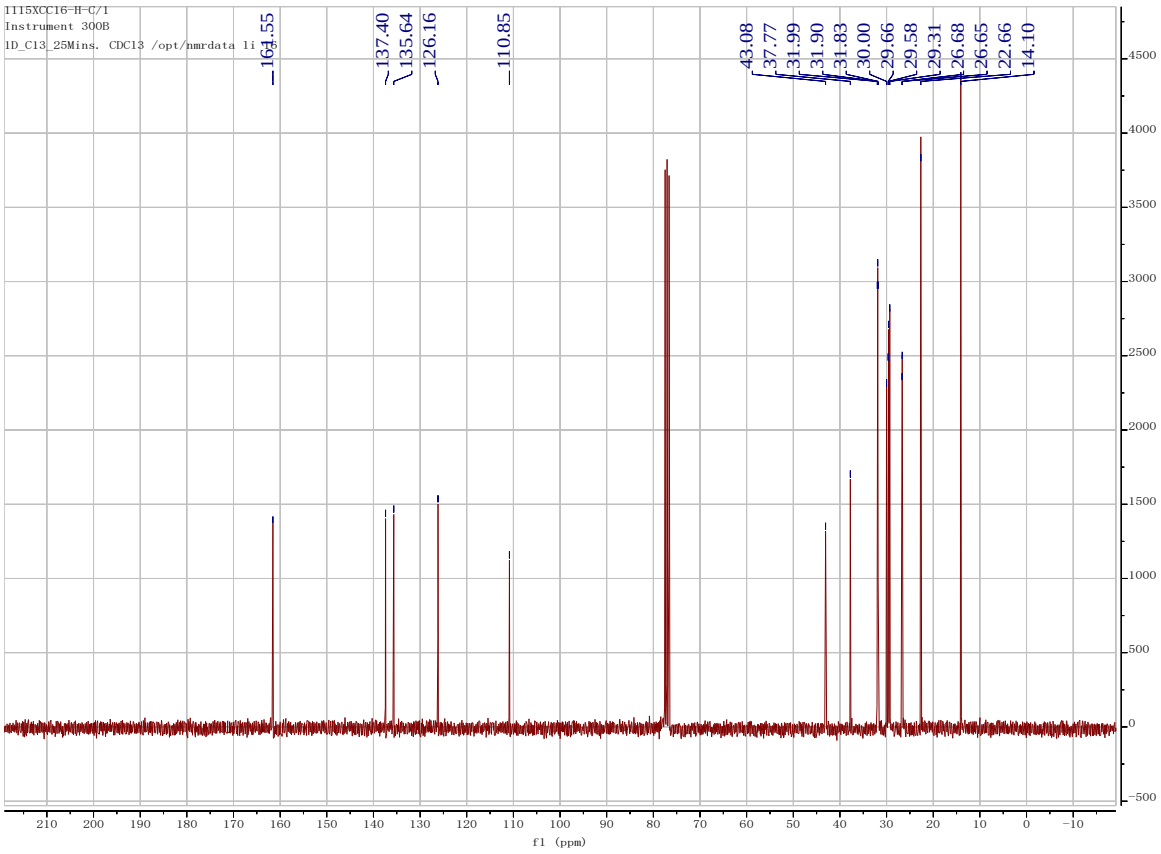

Appendix A- 18 75 MHz ^{13}C NMR spectrum for 5,5'-dibromo-N^{4}, N$^{4'}$-bis(2-hexyldecyl)-[2,2'-bithiophene]-4,4'-dicarboxamide in chloroform-*d*